Structural Characterization of Photovoltaic Nanocrystals, Single Crystals, and Thin Film Semiconductors.

Erin E Jedlicka

A dissertation submitted
in partial fulfillment of the
requirements for the degree of

Doctor of Philosophy

University of Washington

2021

Reading Committee:

David S. Ginger, Chair

Brandi M. Cossairt

Robert E. Synovec

Program Authorized to Offer Degree:

Chemistry

University of Washington

Abstract

Structural Characterization of Photovoltaic Nanocrystals, Single Crystals, and Thin Film Semiconductors.

Erin E Jedlicka

Chair of the Supervisory Committee:

Professor David S. Ginger

Department of Chemistry

According to the U.S. Energy Information Administration, solar and wind make up over two-thirds of the 39.7 giga-watts (GW) of new energy capacity added to the grid in 2021. In addition, wind turbine service technicians and solar panel installers are ranked number one and number three respectively on the U.S. Bureau of Labors "Fastest Growing Occupations for 2019-2029". However, currently solar panels require energy-consuming manufacturing processes, are limited to inflexible substrates, and only convert around 20-30% of light into electricity. Many new alternative materials for solar cells emerged with in the past few decades with low-cost solution processing, the ability to print onto flexible substrates, and the potential to convert higher percentages of light into electricity. However, most studies focus on the improvements in performance without studying the impact that changing processing conditions and adding dopants has on the vertical composition and crystalline structure of the material. Here, we study the structural characteristics of different photovoltaic materials to determine the impact of different processing methods and dopants.

First, we investigate the vertical composition in solution processed photovoltaic semiconductor materials. While solution-processed solar cells offer a low-cost and less energy consuming manufacturing method, the processing materials and method highly impact the performance of the solar cell. In Chapter 2, we investigate how changes in processing photovoltaic thin-films impacts the film morphology and vertical composition of the film. We use glow discharge optical emission spectroscopy (GDOES) coupled with scanning electron microscopy (SEM) to analyze changes in film morphology. We look at three types of semiconductor materials: polymer/quantum dot blends, kesterite, and chalcopyrite. In polymer/quantum dot blends use GDOES to confirm the depth composition from a three-dimensional reconstruction using discrete algebraic reconstruction technique (DART) from scanning electron microscopy images. We discover that a post-deposition ligand exchange directly from the native quantum dot ligands to shorter, electrically conducting ligands results in damage to film causing cracks and voids. However, using a solution-based exchange to an intermediary ligand before a post-deposition ligand prevents damage to the film and results in better device performance. Next, we use GDOES to show that Ag-doping in kesterite films results in a more homogenous composition throughout the film depth and reduces the voids in the film. Finally, we discover that the selenization copper-rich under higher pressure allows results in films with fewer voids and Na-passivated defects. Overall, we see that processing conditions impact the vertical composition and can change the performance of photovoltaic materials.

In addition to changes from processing conditions, changes in material properties can be induced by doping the material. In Chapter 3, we investigate how doping changes the structure of methylammonium lead tribromide ($MAPbBr_3$) single crystals. We observe a shift in the structural phase transition temperature as a result of bismuth incorporation into the crystal structure. Using

x-ray diffraction, we discover a contraction in the lattice constant with increase bismuth concentration. We compare the lattice contraction to the effects of applying external pressure to $MAPbBr_3$ and observe a similar shift to lower temperatures for the phase transition. We use density functional theory (DFT) simulations and determine the likely defect species to be Bi_{Pb}^{+}.

In our final chapter, we investigate the impacts of a remote outreach activity on student knowledge and attitudes towards science. We use pre/post-activity surveys to evaluate changes in student understanding of Next Generation Science Standards (NGSS) aligned content about the relationship between energy production and the environment. We also use 5-point Likert-scale surveys to measure student attitudes towards STEM/STEM careers. We use quantitative statistical analysis methods such as Welch's t-test, Mann-Whitney U test, and Wilcoxon Signed Ranked test to determine the significance of changes between pre/post-activity surveys. We find an increase in the probability of students identifying wind, hydropower, and nuclear energy as renewable resources on the post-survey. Similarly, for non-renewable resources we find an increase in the probability that students identify fossil fuels, gas, and nuclear on the post-activity survey. We observe no changes in student attitudes towards STEM/STEM careers between pre/post survey. However, we determine that teachers over-estimated the changes in student attitudes from the outreach activity. We also observe an interesting result in the post-activity surveys with a higher mean response for "I enjoyed this [outreach] activity" and compared to the mean response for "I enjoy science and engineering activities". This discrepancy in student attitudes should be further studied, however this provides insight in how we can improve student attitudes towards science and engineering activities.

Table of Contents

List of Figures:

Acknowledgement

In what feels like a different lifetime, I was forced to memorize the poem *Invictus* by William Ernest Henley with the hope that it would bring peace and courage in times when everything seemed overwhelming. What I thought would be an inconsequential assignment turned into a meditation and serves as continuous reminder that perseverance can be one of our greatest strengths.

I want to thank the people who have been on this voyage with me, especially those who noticed when the sky was red and understood the meaning. It was not always smooth sailing, but there was no better crew to help get me through the stormy seas. Who knows if my watch has ended or if it has just begun, either way I stand relieved.

I want to thank my advisor David Ginger and the members of my committee for their guidance and support over the past few years. I also want to thank the professors who helped foster the passion all those years ago back at the Naval Academy.

I want to thank my fellow Ginger Lab members for their helpful discussions regarding science, life, and determining what wavelength best describes a particular color. A special thanks to Adam Colbert, Phil Cox, Giles Eperon, Jian Wang, Raj Giridharagopal, Katie Guye, Sarthak Jariwala, Demi Liu for their mentorship, support, and guidance.

This work would not have been possible without the efforts of my research collaborators and I would like to thank Raymond Hickey, Jingjing Jiang, Yuancai Gong, Josh Mutch, Young-Kwang Jung, Prof. Adam Moulé, Prof. Hao Xin, Prof. Jiun-Haw Chu, and Prof. Aron Walsh for all their help.

A special thanks to the Clean Energy Institute, especially Kristine Parra and Danica Hendrickson.

Finally, I want to thank my family – Ben, Madison, and Haley for their love and support.

Chapter 1. Introduction

1.1 Importance of Vertical Composition and Structure in Photovoltaic Devices

Solar cells are vertical devices in which the middle layer, also called the active layer, contains a photovoltaic material that absorbs the energy from light converts it into electrons and holes.[1,2] The electrons and holes generated by the active layer are extracted at electrodes on the top and bottom of the device stack creating an electrical current. Additional layers between the active layer and the electrodes can be added selective conduct charges towards the electrodes adding in charge seperation.[1–3] **Figure 1.1** shows a generic device structure for a solar cell.

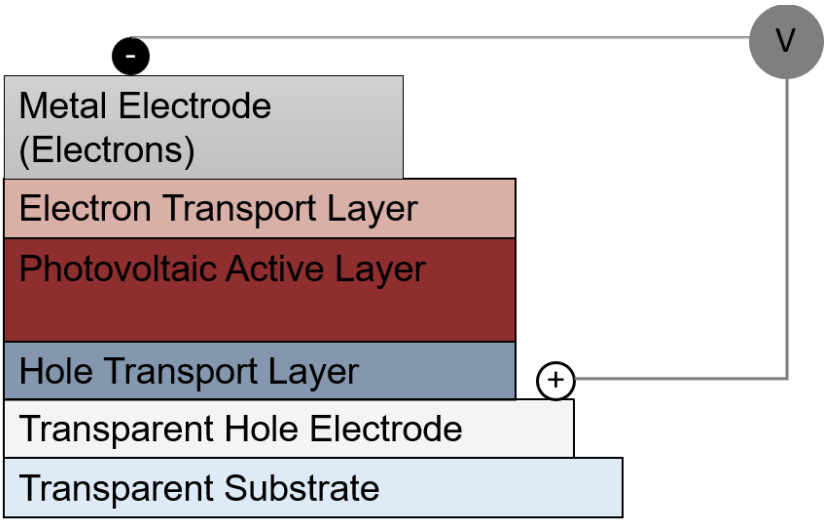

Figure 1.1: Generic solar cell device architecture showing electron and hole extraction electrodes.

However, the process of extracting charges from the solar cells is in competition with the attraction between the negatively charged electrons and the positively charged holes which have the potential to recombine before extraction from the solar cell. The competition between charge extraction and recombination means that the morphology and composition of the different layers of the device influence the overall power conversion efficiencies of the device.[1]

Understanding the structure and composition through the photovoltaic device is of particular importance for solution-processed semiconductor materials. Solution-processed solar cell materials include organic photovoltaics, mixed organic-inorganic polymer/quantum dot blends, perovskites, kesterite, and chalcopyrite. These third-generation solar cell materials are of interest due to the potential for higher power conversion efficiencies, tunable bandgap, potential for use in tandem solar cells, and ability to print onto flexible substrates.[2,4,5] For these emerging solar materials, control over the material structure is traded for lower cost, less energy consuming manufacturing processes.[5,6] Film morphology and composition in solution processed solar cells can be altered through precursor materials, solvents, additives, solvent temperature, deposition spped parameters, thermal annealing, and post-deposition treatments.[7–11] However, often research on these devices focuses on changes in device performance, electronic properties, or surface structure and composition.

This thesis explores the structural properties of different photovoltaic materials including nanocrystals, single crystals, and thin films. First, this thesis investigates three different types of photovoltaic materials using a technique called glow discharge optical emission spectroscopy (GDOES) to analyze the composition as a function of film depth. More details on this technique can be found later in this chapter. Second, this thesis explores how Bi-doping alters the structural phase transitions in methylammonium lead tribromide ($MAPbBr_3$) single crystals and uses the observed lattice contraction to help identify potential doping species. Finally, this thesis examines the impact of outreach activities on the knowledge of the relationship between energy and the environment and attitudes towards science for the next generation of scientists.

References:

(1) Nelson, J. The Physics of Solar Cells; Imperial College Press, London, 2003.

(2) Yan, J.; Saunders, B. R. Third-Generation Solar Cells: A Review and Comparison of Polymer:Fullerene, Hybrid Polymer and Perovskite Solar Cells. *Rsc Adv* **2014**, *4* (82), 43286–43314. https://doi.org/10.1039/c4ra07064j.

(3) Wurfel, U.; Cuevas, A.; Wurfel, P. Charge Carrier Separation in Solar Cells. *Ieee J Photovolt* **2014**, *5* (1), 461–469. https://doi.org/10.1109/jphotov.2014.2363550.

(4) Green, M. A. Third Generation Photovoltaics: Solar Cells for 2020 and Beyond. *Phys E Low-dimensional Syst Nanostructures* **2002**, *14* (1–2), 65–70. https://doi.org/10.1016/s1386-9477(02)00361-2.

(5) Meredith, P.; Armin, A. Scaling of next Generation Solution Processed Organic and Perovskite Solar Cells. *Nat Commun* **2018**, *9* (1), 5261. https://doi.org/10.1038/s41467-018-05514-9.

(6) Alapatt, G. F.; Singh, R.; Poole, K. F. Fundamental Issues in Manufacturing Photovoltaic Modules Beyond the Current Generation of Materials. *Adv Optoelectron* **2012**, *2012*, 1–10. https://doi.org/10.1155/2012/782150.

(7) Huang, Y.; Kramer, E. J.; Heeger, A. J.; Bazan, G. C. Bulk Heterojunction Solar Cells: Morphology and Performance Relationships. *Chem Rev* **2014**, *114* (14), 7006–7043. https://doi.org/10.1021/cr400353v.

(8) Li, Q.; Wang, L.-M.; Liu, S.; Guo, L.; Dong, S.; Ma, G.; Cao, Z.; Zhan, X.; Gu, X.; Zhu, T.; Cai, Y.-P.; Huang, F. Vertical Composition Distribution and Crystallinity Regulations Enable High-Performance Polymer Solar Cells with >17% Efficiency. *Acs Energy Lett* **2020**, *5* (11), 3637–3646. https://doi.org/10.1021/acsenergylett.0c01927.

(9) Li, Q.; Wang, L.-M.; Liu, S.; Zhan, X.; Zhu, T.; Cao, Z.; Lai, H.; Zhao, J.; Cai, Y.; Xie, W.; Huang, F. Impact of Donor–Acceptor Interaction and Solvent Additive on the Vertical

Chapter 2. Investigating Structural Characteristics of Various Solution Processed Semiconductors

2.1 Overview

Solution processed semiconductor materials require lower energy consumption for production than other materials such as silicon solar cells which require prolonged periods of heating to high temperatures.[1,2] However, the easier processing conditions are accompanied by a decrease in the control over composition.[3–7] Understanding the morphological consequences of processing conditions for semiconductor materials is critical for developing these materials for the next generation of solar cells. In this chapter we investigate how processing conditions affect the formation of three different semiconductor candidates for next generation solar materials: quantum-dot (QD)/polymer blends, kesterite films, and chalcopyrite films. For each of these materials, we use optical glow discharge emission spectroscopy (GDOES) to investigate the compositional depth profile of the films to understand how changing processing conditions and precursor materials affects the film quality and device performance.

2.2 Introduction to Glow Discharge Optical Emission Spectroscopy

Glow discharge optical emission spectroscopy (GDOES) provides depth profiles of solids and thin film materials by eroding the sample through ion sputtering and measuring the intensity of emission at different wavelengths.[8–11] Similar techniques include auger electron spectroscopy (AES), X-ray photoelectron spectroscopy (XPS), and secondary ion mass spectrometry (SIMS). Table 1 shows a comparison of these different methods.[8,11]

Table 1: Comparison of Depth Profiling Techniques

	Minimum Area	Maximum Depth	Detection Limit	Advantages	Disadvantages
AES	100 nm	1 µm	0.1 atomic %	Local depth profiling	No bulk insulators Preferential sputtering
GDOES	2 mm	100 µm	10 µg/g	Works with Insulators	Poor lateral resolution Preferential sputtering
SIMS	1 µm	1 µm	0.1 atomic %	Very fast Low Ion energy Works with Insulators	No lateral resolutions Impacted by crater profile
XPS	1 µm	1 µm	0.1 atomic %	Surface sensitive Lateral resolution	No bulk insulators Mass interference

Compared to other elemental analysis, GDOES allows for fast analysis of the sample over a large area and depth. The measurement time for GDOES stays on the order of minutes per sample making it a very fast method for analyzing vertical compositions.[8–11] Additionally, GDOES can be used to profile the composition of insulating materials which can not be resolved through AES or SIMS.[11] The large measurement area and ability to work well with both conductive and insulating materials makes GDOES a good measurement tool for analyzing thin-film semiconductor

materials. However, GDOES measurements are impacted by the uniformity of sputtering across the measurement area and are unable to provide lateral resolutions of elemental compositions.[8–11] In blended semiconductor materials, the sputtering rate can vary as a function of composition making quantitative analysis difficult as changes in composition can impact the sputtering rate through the sample.[8]

Here, we use GDOES to qualitative compare how the composition changes through the film thickness and at the film interfaces. We use the relative emission intensities to compare the elemental ratios as a function of depth for three different semiconductor materials. In our first study, we use the compositional depth profile to confirm the results of a three-dimensional reconstruction of the film from transmission electron microscopy (TEM) images. In the second study, we investigate how Ag-doping in kesterite films changes film morphology by reducing the formation of voids in the active layer and preventing blending of layers at the interfaces of the film. Finally, we show that higher selenization pressure in copper-rich chalcopyrite semiconductors reduces $Cu_{2-x}Se$ defect formation and allows for Na passivation of active layer defects such as grain boundaries, In_{Cu} interstitials, and Se vacancies.

2.3 Morphological Consequences of Ligand Exchange in Quantum Dot – Polymer Blend Solar Cells

The first system we examine combines conductive organic polymers with inorganic quantum dots (QDs). Fully organic solar cells created from of blends of donor and acceptor polymers lag in performance compared to silicon solar cells which allow for better charge transportation through the active layer due to the more conductive nature of the materials.[12–15] However, the ability to create solution processable solar cells remains attractive due the lower cost of fabrication, ability to process at lower temperature without high vacuum environments, and the potential to create flexible solar cell devices. Combining inorganic QDs with electrically conductive polymers theoretically would allow for solution processable solar cells with more tunable band gaps, increased thermal stability, and reduced carrier recombination.[16–20] However, in practice these hybrid organic/inorganic devices only achieved a maximum power conversion efficiency (PCE) of 5.5%,[21] performing worse than QD-only solar cells and organic photovoltaics with record PCEs of over 10%.[12–15,22]

The reduced power conversion efficiency is attributed in part to poor transfer of the electrons between the polymer and the quantum dots due to the long electrically inactive hydrocarbon chains on the native oleic acid (OA) ligands on the surface of the quantum dots.[23] Ligand exchange improves power conversion efficiency by replacing bulky organic OA ligands with shorter more electrically active ligands such as butylamine (BA), ethanedithiol (EDT), or mercaptopropionic acid (MPA).[23–26] While it is possible to exchange the ligands on the quantum dots directly before combining with the polymer, the BA, EDT, and MPA ligands are more polar than the OA which leads to poor miscibility with the non-polar polymer solution. Colbert and co-workers report a better device efficiency and high external quantum efficiencies (EQE) in QD/polymer devices following a two-step ligand exchange procedure. In the first ligand exchange, OA ligands on PbS QDs are exchanged in solution with BA ligands resulting in BA-capped PbS QDs. The BA-capped QDs are then mixed with a the polymer poly((4,8-bis(octyloxy)benzo(1,2-b:4,5-b')-dithiophene-2,6-diyl)(2- ((dodecyloxy)carbonyl)thieno (3,4-b)-thiophenediyl)) (PTB1) and the solution is then deposited onto a substrate to form a thin film. Following deposition, the

BA-ligand is replaced with MPA by exposing the film to a MPA solution and spincoating off excess solution.[27]

To better understand the improved device performance of two-step ligand exchange processes, we investigate the morphological consequences of different ligand exchange protocols specifically looking at the differences between a single step ligand exchange from OA-capped PbS QDs to MPA-capped PbS QDs versus a two-step ligand exchange using a BA-capped PbS QDs as an intermediary for film processing before exchanging the BA for MPA. Figure 2.1a shows a schematic of the two different ligand exchange processes we employed in this study. Experimental methods for quantum dot synthesis, QD/polymer film preparation and ligand exchange procedures are described in detail in Appendix A.

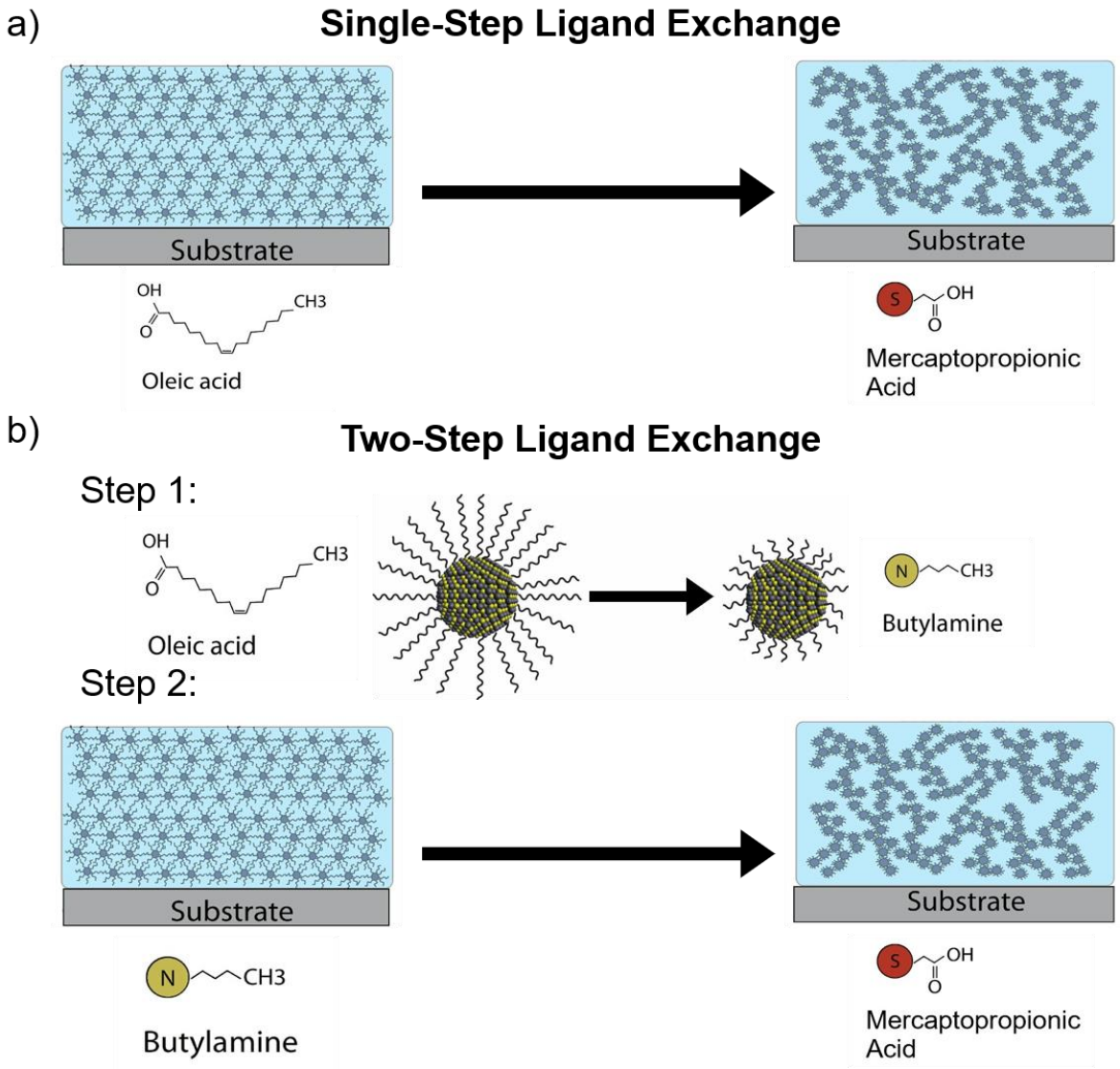

Figure 2.1: Schematics of different ligand exchange procedures: (a) One-step post-deposition ligand exchange from oleic acid to mercaptopropionic acid and (b) Two-step ligand exchange with step (1) a solution based ligand exchange on the QDs from oleic acid to butylamine and step (2) a post-deposition ligand exchange from butylamine to mercaptopropionic acid.

To better understand how the polymer and QD morphology changes throughout the bulk of the film as a function of ligand exchange, we employ high annual dark field electron tomography (HAADF-ET) and use discrete algebraic reconstruction technique (DART) to create a 3-dimensional reconstruction of the film. More details about the HAADF-ET and DART reconstruction methods can be found in the following publication by Hickey co-workers.[28] Here, we briefly summarize the finding of the 3D reconstruction of films as a result of the two ligand treatment schemes discussed in Figure 1. Figure 2.2 shows 20 x 20 x 20 nm volume DART reconstruction of the films with Figure 2.2A and 2.2B showing the film before and after the single step ligand exchange with MPA and Fig. 2.2C and 2.2D showing the films resulting from the two-step ligand exchange procedure.

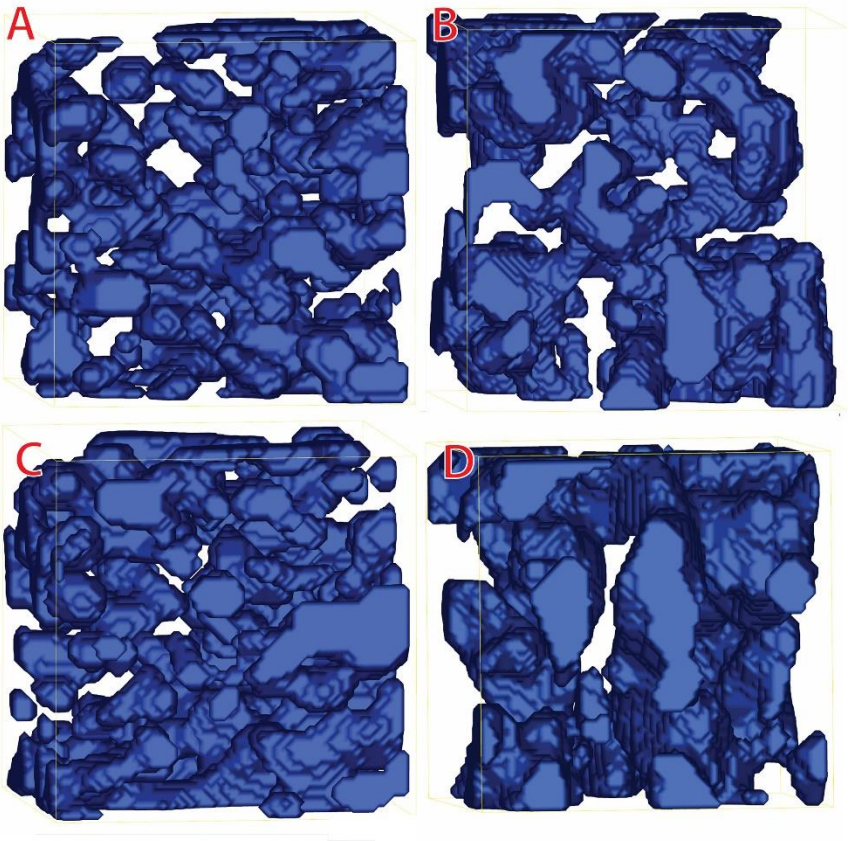

Figure 2.2 Three-dimensional DART reconstruction of the PbS phase in PbS/PTB1 blend films with different ligand treatments: (a) as-cast OA-capped PbS QDs (b) post-deposition MPA ligand exchange treatment of OA-capped PbS QDs, (c) as-cast BA-capped PbS QDs, (d) post-deposition MPA ligand exchange treatment of BA-capped PbS QDs. The negative space represents mixed PbS/PTB1 phase and voids in the film. Adapted with permissions from *Organic Electronics* **2018**, 54, 119-125, DOI: 10.1016.j.orgel.2017.12.018 Copyright © 2017 Elsevier B.V.

In **Figure 2.2** the blue regions represent the PbS QD only phase of the films with the negative spaces representing the mixed PTB1/PbS phase as well as any void present in the film. We see that after the MPA ligand exchange the PbS regions get larger when exchanging the OA ligand to MPA and remain approximately the same size when exchanging from BA to MPA. It is also important to note that when exchanging from OA to MPA, the film after ligand exchange

shows evidence of voids forming along the surface of the film as shown in both the AFM and SEM images of the film as seen in Supporting Information Fig S1 and Fig S2. Hickey and co-workers quantified by determining the volume fraction and surface area to volume ratio of PbS QD domains in the 3D reconstructions as summarized in Table 1.[28] These measurements confirm the observation that the PbS regions of the films become larger as a result of ligand exchange, but the ratio of PbS QDs on the surface of the film decreases during the ligand exchange process.

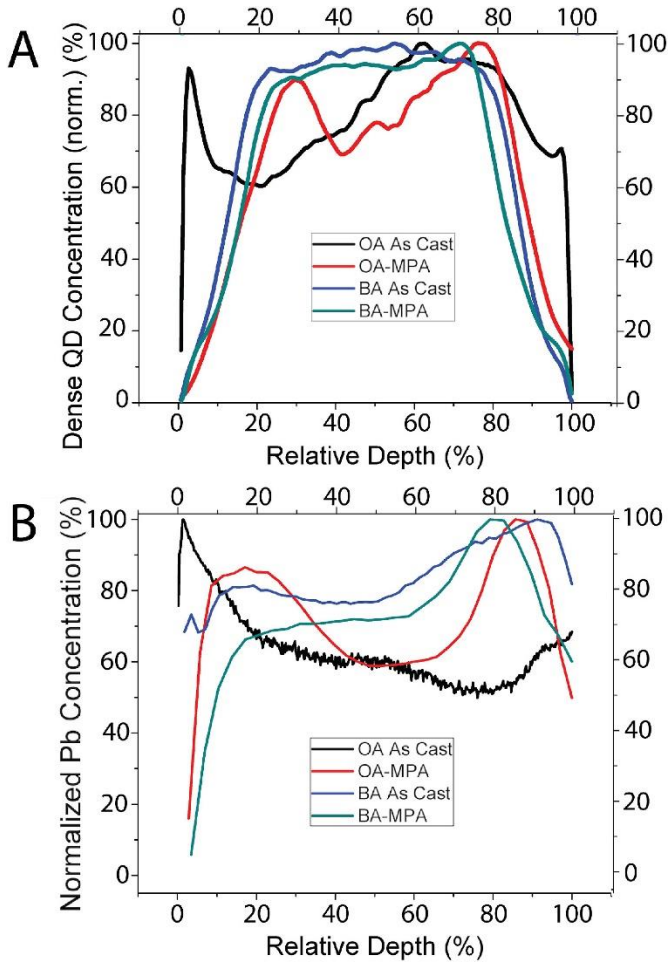

Figure 2.3: Depth profile of Pb concentration in film composition; the top of the film is 0 % and the bottom of the film is 100%. (a) Normalized Pb concentration as determined through DART reconstruction (b) Normalized Pb concentration as determined through GDOES. Adapted with permissions from *Organic Electronics* **2018**, 54, 119-125, DOI: 10.1016.j.orgel.2017.12.018 Copyright © 2017 Elsevier B.V.

We use (GDOES) as a physical measurement of the vertical composition of the QDs in the film to confirm the distribution of PbS determined from the DART reconstructions. **Figure 2.3** shows the normalized concentration of Pb through the depth of the film as determined by DART reconstruction (Fig. 2.3A) and GDOES (**Fig. 2.3B**). We use the Pb concentration as a proxy for PbS concentration because the both the PTB1 and the MPA contain sulfur atoms and would not be able to distinguish between the polymer, ligand, and quantum dots. Overall, there is good qualitative agreement between the DART and GDOES measurements. The OA PbS film without

MPA treatment shows a larger concentration of PbS on the surface of the film compared to the other films agreeing with the larger PbS volume to surface area ratio calculated from DART reconstructions. When the OA is exchanged for MPA, the amount of PbS at the surface decreases and the concentration of PbS throughout the film is inconsistent with higher concentrations towards the top and bottom of the film with lower concentrations in the center. We suspect that this is due to the ligand exchange which exposes the top of the film first, creating voids as the long OA chains are replaced with much shorted MPA ligands.

In the BA PbS films, we see that the QD phase in both the as-cast film and the MPA-exchanged film appears to be concentrated in the center of the film as shown in Fig. 2.3A. We suggest that this results from the difference in larger difference in polarities between the BA QDs and the PTB1 polymer preventing better mixing. We attribute the differences between the DART and GDOES concentrations towards the bottom of the film to the difference in sputtering rate between the polymer and the PbS which causes uneven etching of the film.

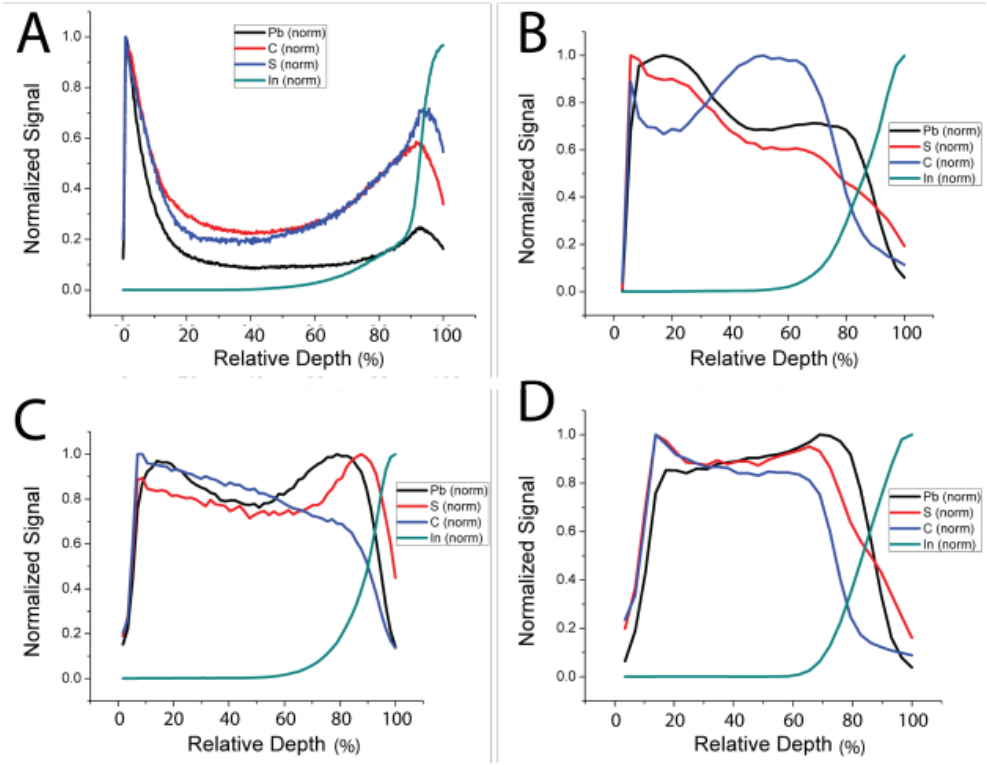

Figure 2.4: GDOES compositional profiles for Pb, S, C, and In for each sample. (A) OA as cast, (B) OA-MPA treated, (C) BA as cast, (D) BA-MPA treated.

This can be seen in **Figure 2.4** which shows the GDOES data of the films tracking Pb, S, C and In. The In signal is used to determine the interface with the indium tin oxide (ITO) on the substrate. In all four films, the normalized intensity for carbon, which would largely come from the polymer, decreases in intensity before the Pb and S indicating the polymer sputters at a faster rate than the PbS QDs. We suspect the uncertainty in the ratio of Pb in the film increases towards the bottom of the film as the PTB1 has been etched away and the remaining signal comes from the unetched quantum dots. Despite these physical limitations of the GDOES measurement, we find the results supports the qualitative data from the reconstructed volumes.

In summary, we used GDOES to verify the tomographic reconstruction of blended PbS/PTB1 films with different ligand exchange methods. In the single step ligand exchange, the film showed defect formation and voids form as a result of replacing the long hydrocarbon chains from the OA ligands with the shorter chains from MPA. Films made from a two-step ligand exchange procedure, where OA was replaced with BA before making films, there was no formation of voids or defects in the film upon MPA ligand exchange. In addition, films using the two-step ligand exchange method showed a more uniform distribution of PbS QDs throughout the film which may explain in part the better performance of devices made using this protocol. Understanding the morphological consequences of solution processing provides critical information for device performance.

2.4 Kesterite Solar Cell Morphology and Performance Improved Via Ag Doping

The second semiconductor material group we study are kesterite semiconductors including Cs_2ZnSnS_4 (CZTS), $Cu_2ZnSnSe_4$ (CZTSe), and the sulfur/selenium alloy $Cu_2ZnSn(S,Se)_4$ (CZTSSe). These materials offer a less toxic alternative to copper indium gallium selenide (CIGS) semiconductor solar cells made with earth-abundant elements.[29–33] However, the power conversion efficiency (PCE) of kesterite solar cells currently remains at 12.6%[34,35] which lag behind the performance of CIGS solar cells at 23.35% PCE. One potential cause of the poor device performance for kesterite solar cells is the large open-circuit voltage deficit ($V_{oc,def}$) which is attributed to many factors including deep intra-band defect levels, recombination of charges at the interface, alternative crystalline phase formation, and band tailing.[36–41] In this section we investigate the morphological consequences of incorporating Ag into CZTSSe in order to decrease the $V_{oc,def}$.

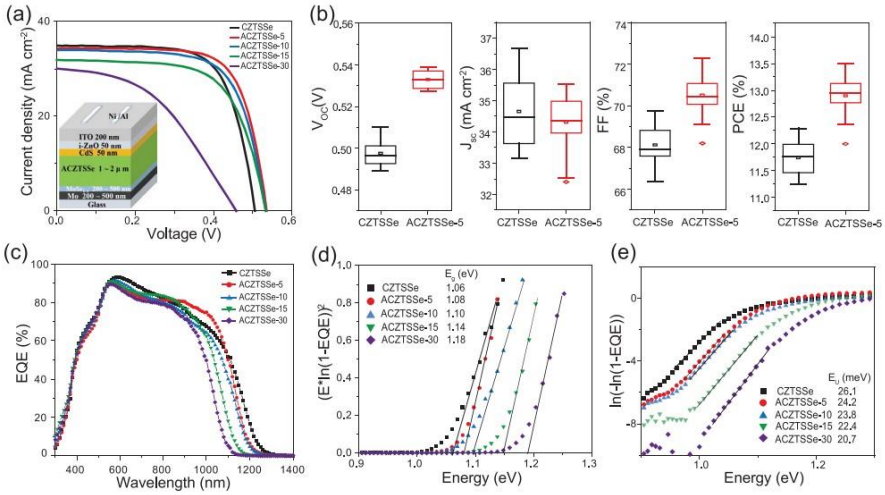

Figure 2.5: a) Current density-voltage (J-V) curves for CZTSSe and ACZTSSe-n (n= 5, 10, 15, 30) solar cells. b) Box plots of device parameters for CZTSSe and ACZTSSe-5 based on 20 devices. c) External quantum efficiency (EQE) curves of CZTSSe and A-CZTSSe-n devices. d) Bandgap and e) Urbach energy determined from EQE measurements. Adapted with permissions from *Adv. Funct. Mater.* **2021**, 2101927, DOI: 10.1002/adfm.202101927 Copyright © 2021 Wiley-VCH GmbH

In order to investigate the impacts of Ag incorporation into CZTSSe on the $V_{oc,def}$, our co-workers made CZTSSe devices with varying concentrations of Ag^{+} in the precursor solution. **Figure 2.5** shows the device structure, current-voltage curves, and EQE for the various compositions created.[42] From the device measurements, we see that devices with 5% Ag (ACZTSSe-5) in the precursor solution show the best improvement in device performance compared to the undoped CZTSSe devices. **Figure 2.5D** shows the comparison between V_{OC}, short-circuit current density (J_{sc}), fill factor (FF), and power-conversion efficiency (PCE) for the CZTSSe and ACZTSSe-5 samples. As shown in **Fig 2.5D**, the sample with Ag doping shows improvements in the V_{oc}, FF, and PCE with comparable J_{sc} performance.

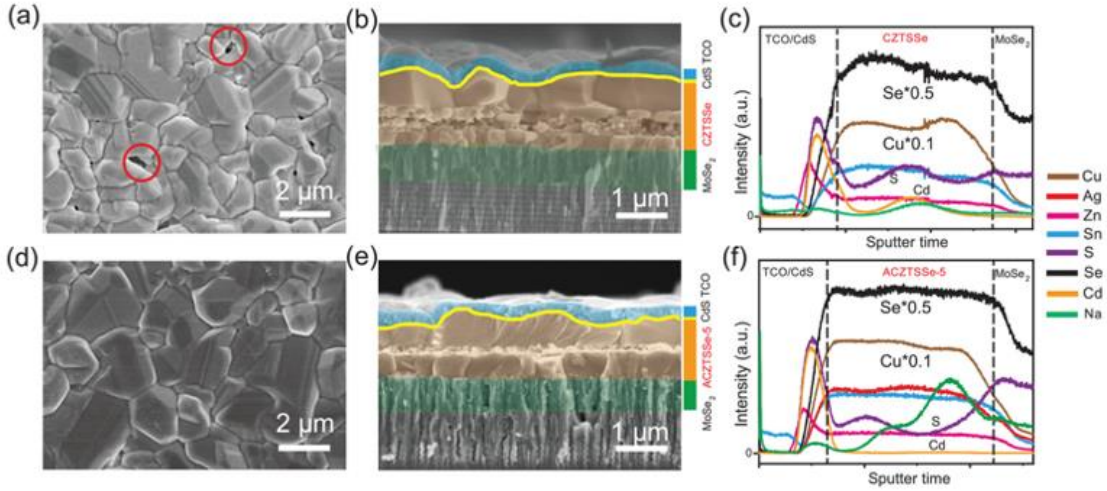

Figure 2.6: Morphology characterization of CZTSSe and ACZTSSe-5 films. CZTSSe film: a) SEM, b) cross-sectional SEM, c) compositional depth profile. ACZTSSe-5 film d) SEM, e) cross-sectional SEM, f) compositional depth profile. Adapted with permission from *Adv. Funct. Mater.*, **2021**, 2101927, DOI: 101002/adfm.202101927 © 2021 Wiley-VCH GmbH

To understand why Ag incorporation improves device performance, we use GDOES to investigate the changes in vertical composition as Ag incorporates into the film. **Figure 2.6A** and **Fig. 2.6D** shows the SEM of the CZTSSe and ACZTSSe-5 films respectively. Both films have large grains on the scale of a few micrometers, but the film without Ag-doping shows evidence of voids (circles in red) while the ACZTSSe film show a more uniform film without voids on the surface of the film. The cross-sectional SEM profile of the films, **Fig. 2.6B** (CZTSSe) and **Fig. 2.6E** (ACZTSSe), show a tri-layer structure common in CZTSSe films that we attribute to a bidirectional grain growth resulting from using a Sn^{4+}-based DMSO precursor solution.[43] The thinner middle layer of the ACZTSSe-5 film compared to the larger middle layer of the CZTSSe film results from faster grain growth that we attribute to the Ag incorporation. Comparing the grain size and middle layer in higher Ag concentration films, shown in Supporting Information **Figure S3**, we observe an increase in grain size and a decrease in the thickness of the middle layers with higher Ag doping in the films.

We use glow discharge optical emission discharge spectroscopy (GDOES) to compare the vertical composition of the CZTSSe (**Fig. 2.6C**) and ACZTSSe-5 (**Fig. 2.6F**). **Figure 2.6C** and **Fig. 2.6F** shows the vertical depth profile of Cu (brown), Zn (pink), Sn (blue), S (purple), Se (black), Ag (red), Cd (yellow), and Na (green). At the top interface of the film, we observe Cd infiltrating into the active layer of CZTSSe film instead of remaining on top of the active layer as seen in the ACZTSSe-5 film. The Cd comes from a post-treatment of the films with a chemical bath deposition of CdS. The absence of Cd in the ACZTSSe-5 film supports the observation that Ag prevents the formation of voids in the film through which CdS can penetrate the CZTSSe layer. Comparing the active layer of the films, we see the ACZTSSe-5 film has a more even distribution of Cu, Sn, and Se throughout the active layer suggesting that Ag incorporation aids in grain growth allowing for more uniform vertical composition. The bottom interface of the films shows a higher concentration of sulfur in the ACZTSSe-5 film compared to the CZTSSe film which we attribute to faster grain growth resulting from the Ag incorporation. The formation of the ACZTSSe/CZTSSe absorber materials proceeds via a two-step process as shown in Eq. 1 and Eq. 2 below:[42]

$$2x\mathrm{Ag(Tu)_3NO_3} + 2(1-x)\mathrm{Cu(Tu)_3Cl} + \mathrm{Zn(Tu)_2(OAc)_2} + \mathrm{Sn(DMSO)_2Cl_4} \rightarrow \mathrm{(Ag,Cu)_2ZnSnS_4} \quad (1)$$

$$\mathrm{(Ag,Cu)_2ZnSnS_4} + 4\ \mathrm{Se} \rightarrow \mathrm{(Ag,Cu)_2ZnSn(S,Se)_4} \quad (2)$$

With the introduction of Se in the second step, the absence of Se at the bottom interface for the ACZTSSe-5 film suggests that the grains have already begun forming before the precursor film is exposed to selenium. This supports the hypothesis that Ag incorporation promotes crystal growth in the film, improving film quality and allowing for better charge transport through the film.

Overall, we observe that doping CZTSSe films with Ag improves device performance compared to undoped films prepared using the same synthetic method. The ACZTSSe films show a smaller $V_{oc,def}$ with higher PCE, FF, V_{oc} and comparable J_{sc} to the CZTSSe films. We attribute the improved device performance to better film morphology due to the lack of void formation and more uniform vertical composition observed in the ACZTSSe-5 films.

2.5 High Selenization Pressure Improves Film Homogeneity and Morphology.

The final semiconductor material we investigate is the chalcopyrite absorber copper indium sulfoselenide CuInSSe (CISSe). The formation of CISSe films requires selenization which exposes the precursor film to elemental Se or H_2Se and results in the formation of several liquid byproducts such as $Cu_{2-x}Se$, In_4Se_3, or InSe.[44,45] Excessive $Cu_{2-x}Se$ byproducts in the film can result in the formation of recombination centers and shunt paths in the absorber. To prevent these defects, CISSe films have been fabricated under copper-poor conditions to reduce the amount of $Cu_{2-x}Se$ formed.[46–48] However, both experimental and theoretical calculations indicate that copper-rich films have the potential to achieve higher efficiencies due to higher carrier concentrations and the potential for lower defect concentrations. Jiang and co-workers previously reported the suppression of $Cu_{2-x}Se$ defects in Cu-poor films processed using a dimethylformamide (DMF) molecular solution under pressures above 1 atm.[49–53] In this work, we investigate the impact of

various copper concentrations at pressures above 1 atm and below 1 atm on device performance and film morphology.

To investigate the morphological consequences of copper concentration under pressures above 1 atm, CISSe precursor films were synthesized using the following [Cu]/[In] ratios in a DMF solution: 0.85, 0.95, 1.05, and 1.20. These films were subsequently selenized under two different pressures with films selenized under a lower pressure of 0.10 MPa (condition A) and a higher pressure of 0.16 MPa (condition B). **Figure 2.7** shows the performance of solar cell devices made from the resulting films.[54] The current density-voltage (JV) curves shown in **Figure 2.7A** show that increasing [Cu]/[In] ratio from 0.85 to 1.05 improves the device performance for both selenization conditions. However, for [Cu]/[In] ratio of 1.20 both selenization conditions show a significant deterioration in device performance. Additionally, we observe that for all [Cu]/[In] ratios the higher pressure selenization devices perform better than the lower pressure selenization devices. Additional device characterization parameters such as PCE, J_{sc}, V_{oc}, FF, are detailed in Table 1 of the supporting information.

Figure 2.7B shows similar external quantum efficiencies through the visible and near-infrared region for all devices except for devices with a [Cu]/[In] ratio of 1.20. **Figure 2.7C, D** extrapolate the bandgap from the EQE for the low pressure and high pressure selenization respectively. We see an increase in bandgap for the copper-rich devices synthesized under higher selenization pressures, with the except of [Cu]/[In] ratio of 1.20 which have lower bandgaps.

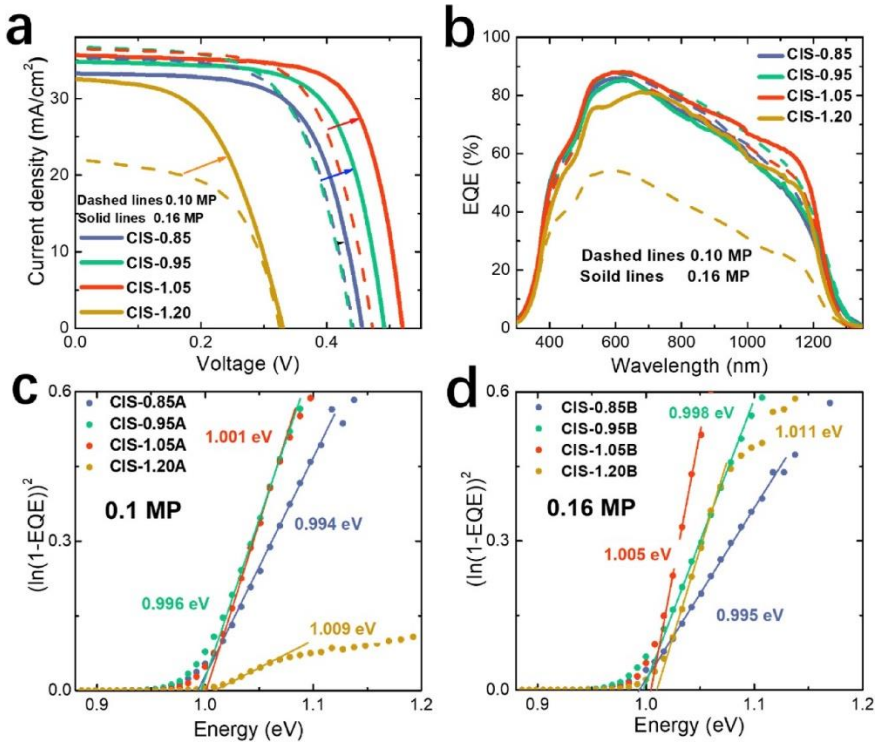

Figure 2.7: Device characterization of CISSe films under different Cu/In ratios and different processing pressures. (a) JV curves, (b) EQE, (c,d) band gap estimation of top performing CIS solar cells under each processing condition. Adapted with permission from *Nano Energy*, **2020**, 69, 104438, DOI: 10.1016/j.nanoener.2019.104438 © 2019 Elsevier Ltd.

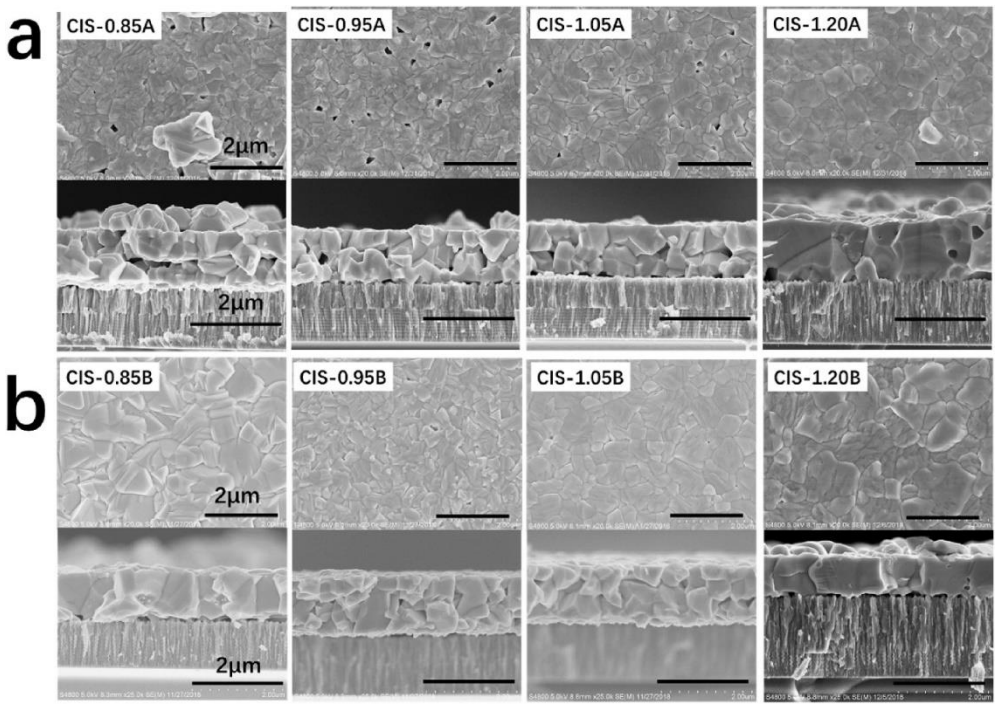

Figure 2.8: (top) SEM and (bottom) cross-sectional SEM images of CISSe films with various Cu/In ratios under lower pressure, 0.10 MPa (condition A), and higher pressure, 0.16 MPa (condition B). Adapted with permission from *Nano Energy*, **2020**, 69, 104438, DOI: 10.1016/j.nanoener.2019.104438 © 2019 Elsevier Ltd.

To understand the improvement in device performance, we look at the film morphology and composition for the different processing conditions. **Figure 2.8** shows the film and cross-sectional SEM images of all films. For the films processed under low pressure, we find that increasing the copper concentration results in denser films with less voids. However, we see that the corresponding compositions under high selenization pressure have no voids and are more densely packed. Additionally, the cross-sectional images show that the high pressure selenization films have smoother surfaces than the low selenization pressure films which show several grains growing above the surface.

While the SEM indicates that the high pressure helps form denser films with fewer voids, we use GDOES to investigate the differences in copper-poor versus copper-rich devices selenized under high pressure. **Figure 2.9** shows the depth composition profiles for the CIS-0.85 (**Fig 2.9A**) and CIS-1.05 (**Fig. 2.9D**) [Cu]/[In] films. We compare the Cu/In and (Cu+In)/(S+Se) ratios for the two films in **Fig. 2.9B** and **Fig. 2.9E** respectively. As expected, we find higher ratios for the CIS-1.05 [Cu]/[In] film due to the higher amount of copper in the precursor solution. Both films show uniform distribution throughout the depth of the films. However, we observe that the amount of copper on the surface of the CIS-0.85 film is approximately half the amount of copper in the bulk of the film. We observe the opposite trend with the Na in **Fig. 2.**9C, where Na concentration is higher at the surface for the CIS-0.85 film. In the CIS-1.05, we observe lower amount of Na present at the film surface and higher amounts in the middle of the active layer.

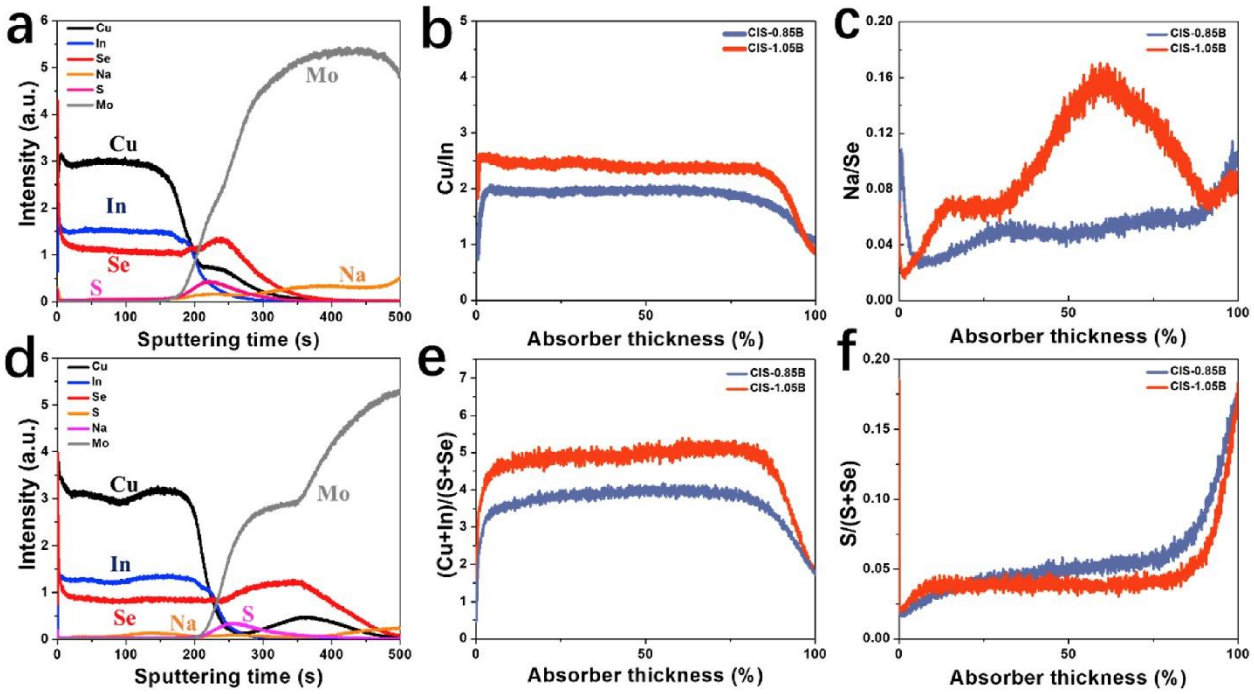

Figure 2.9: Compositional depth profiles measured through glow discharge optical emission spectroscopy CISSe films. (a, d) show depth profiles of selected elements for CIS-0.85B (a) and CIS-1.05B (d) and (b, c, e, and f) show the selected ratios of ions in CIS-0.85B (blue) and CIS-1.05B (red): (b) Cu/In, (c) Na/Se, (d) (Cu+In)/(S+Se) and (e) S/(S+Se). Adapted with permission from *Nano Energy*, **2020**, 69, 104438, DOI: 10.1016/j.nanoener.2019.104438 © 2019 Elsevier Ltd.

We propose that the Na is located at different defect sites in the two films. In the CIS-0.85 copper-poor film, we believe the Na occupies copper vacancies towards the surface of the film. However, in the CIS-1.05 film, we propose that the Na primarily passivates defects within the film such as grain boundaries, In_{Cu} interstitials, or Se vacancies leading to an increase in the hole concentration and improvement in the power conversion efficiency.[55–58] Overall, we determine that a higher selenization pressure and a [Cu]/[In] ratio of 1.05 yields the best devices due to optimized morphology with reduced $Cu_{2-x}Se$ defect formation and passivated active layer defects.

2.6 Conclusion:

We used GDOES to characterize the vertical composition for three different semiconductor materials and found improvements in film morphology lead to improvements in device performance for all three systems studied. In polymer/quantum dot blend films, a single-step ligand exchange from native oleic acid ligands to MPA results in the formation of cracks and voids through the film surface. However, using a 2-step ligand exchange procedure with a solution-based exchange to butylamine before deposition prevents damage to the film during the second ligand exchange procedure and yields better device performance. In CZTSSe, we found that Ag-doping lead to faster grain growth and prevented void formation. In CISSe, we find that using a higher selenization pressure prevented void and $Cu_{2-x}Se$ defect formation. The resulting films showed denser active layers with fewer voids and Na-passivated grain boundaries.

2.7 Acknowledgements

We thank our collaborators in the Moulé Group at U.C. Davis and the Xin Group at Nanjing University of Post and Telecommunication. The study on the morphology of polymers/quantum dots blends was primarily funded by the U.S. National Science Foundation under award No. 1436273. The study on Ag doping was funded supported by the National Key Research and Development Program of China (2019YFE0118100) and the National Natural Science Foundation of China (22075150, 62074052, U1902218). The work on copper-rich CISSe at different selenization pressures was primarily funded by the National Natural Science Foundation China (NSFC, Grant No. 21571106). We acknowledge support of facilities in the Molecular Analysis Facility, a National Nanotechnology Coordinated Infrastructure site at the University of Washington which was supported in part by the National Science Foundation (Grant NNCI-1542101), the University of Washington, the Molecular Engineering and Sciences Institute, the Clean Energy Institute, and the National Institutes of Health.

References:

(1) Gong, J.; Darling, S. B.; You, F. Perovskite Photovoltaics: Life-Cycle Assessment of Energy and Environmental Impacts. *Energ Environ Sci* **2015**, *8* (7), 1953–1968. https://doi.org/10.1039/c5ee00615e.

(2) Woodhouse, M.; Smith, B.; Ramdas, A.; Margolis, R. Crystalline Silicon Photovoltaic Module Manufacturing Costs and Sustainable Pricing: 1H 2018 Benchmark and Cost Reduction Roadmap. *National Renewable Energy Laboratory.* **n.d.**

(3) Yan, J.; Saunders, B. R. Third-Generation Solar Cells: A Review and Comparison of Polymer:Fullerene, Hybrid Polymer and Perovskite Solar Cells. *Rsc Adv* **2014**, *4* (82), 43286–43314. https://doi.org/10.1039/c4ra07064j.

(4) Green, M. A. Third Generation Photovoltaics: Solar Cells for 2020 and Beyond. *Phys E Low-dimensional Syst Nanostructures* **2002**, *14* (1–2), 65–70. https://doi.org/10.1016/s1386-9477(02)00361-2.

(5) Alapatt, G. F.; Singh, R.; Poole, K. F. Fundamental Issues in Manufacturing Photovoltaic Modules Beyond the Current Generation of Materials. *Adv Optoelectron* **2012**, *2012*, 1–10. https://doi.org/10.1155/2012/782150.

(6) Wang, Q.; Xie, Y.; Soltani-Kordshuli, F.; Eslamian, M. Progress in Emerging Solution-Processed Thin Film Solar Cells – Part I: Polymer Solar Cells. *Renew Sustain Energy Rev* **2016**, *56*, 347–361. https://doi.org/10.1016/j.rser.2015.11.063.

(7) Meredith, P.; Armin, A. Scaling of next Generation Solution Processed Organic and Perovskite Solar Cells. *Nat Commun* **2018**, *9* (1), 5261. https://doi.org/10.1038/s41467-018-05514-9.

(8) Angeli, J.; Bengtson, A.; Bogaerts, A.; Hoffmann, V.; Hodoroaba, V.-D.; Steers, E. Glow Discharge Optical Emission Spectrometry : Moving towards Reliable Thin Film Analysis–a Short Review. *J Anal Atom Spectrom* **2003**, *18* (6), 670–679. https://doi.org/10.1039/b301293j.

(9) Shimizu, K.; Habazaki, H.; Skeldon, P.; Thompson, G. E. Radiofrequency GDOES: A Powerful Technique for Depth Profiling Analysis of Thin Films. *Surf Interface Anal* **2003**, *35* (7), 564–574. https://doi.org/10.1002/sia.1572.

(10) Gamez, G.; Voronov, M.; Ray, S. J.; Hoffman, V.; Hieftje, G. M.; Michler, J. Surface Elemental Mapping via Glow Discharge Optical Emission Spectroscopy. *Spectrochimica Acta Part B* **2012**, No. 70, 1–9.

(11) Oswald, S.; Baunack, S. Comparison of Depth Profiling Techniques Using Ion Sputtering from the Practical Point of View. *Thin Solid Films* **2003**, *425* (1–2), 9–19. https://doi.org/10.1016/s0040-6090(02)01097-0.

(12) You, J.; Dou, L.; Yoshimura, K.; Kato, T.; Ohya, K.; Moriarty, T.; Emery, K.; Chen, C.-C.; Gao, J.; Li, G.; Yang, Y. A Polymer Tandem Solar Cell with 10.6% Power Conversion Efficiency. *Nat Commun* **2013**, *4* (1), 1446. https://doi.org/10.1038/ncomms2411.

(13) Liu, Y.; Zhao, J.; Li, Z.; Mu, C.; Ma, W.; Hu, H.; Jiang, K.; Lin, H.; Ade, H.; Yan, H. Aggregation and Morphology Control Enables Multiple Cases of High-Efficiency Polymer Solar Cells. *Nat Commun* **2014**, *5* (1), 5293. https://doi.org/10.1038/ncomms6293.

(14) Nam, S.; Seo, J.; Woo, S.; Kim, W. H.; Kim, H.; Bradley, D. D. C.; Kim, Y. Inverted Polymer Fullerene Solar Cells Exceeding 10% Efficiency with Poly(2-Ethyl-2-Oxazoline) Nanodots on Electron-Collecting Buffer Layers. *Nat Commun* **2015**, *6* (1), 8929. https://doi.org/10.1038/ncomms9929.

(15) Chen, J.; Cui, C.; Li, Y.; Zhou, L.; Ou, Q.; Li, C.; Li, Y.; Tang, J. Single-Junction Polymer Solar Cells Exceeding 10% Power Conversion Efficiency. *Adv Mater* **2015**, *27* (6), 1035–1041. https://doi.org/10.1002/adma.201404535.

(16) Hines, M. A.; Scholes, G. D. Colloidal PbS Nanocrystals with Size-Tunable Near-Infrared Emission: Observation of Post-Synthesis Self-Narrowing of the Particle Size Distribution. *Adv Mater* **2003**, *15* (21), 1844–1849. https://doi.org/10.1002/adma.200305395.

(17) Chang, L.; Lademann, H. W. A.; Bonekamp, J.; Meerholz, K.; Moulé, A. J. Effect of Trace Solvent on the Morphology of P3HT:PCBM Bulk Heterojunction Solar Cells. *Adv Funct Mater* **2011**, *21* (10), 1779–1787. https://doi.org/10.1002/adfm.201002372.

(18) Ning, Z.; Zhitomirsky, D.; Adinolfi, V.; Sutherland, B.; Xu, J.; Voznyy, O.; Maraghechi, P.; Lan, X.; Hoogland, S.; Ren, Y.; Sargent, E. H. Graded Doping for Enhanced Colloidal Quantum Dot Photovoltaics. *Adv Mater* **2013**, *25* (12), 1719–1723. https://doi.org/10.1002/adma.201204502.

(19) Noone, K. M.; Subramaniyan, S.; Zhang, Q.; Cao, G.; Jenekhe, S. A.; Ginger, D. S. Photoinduced Charge Transfer and Polaron Dynamics in Polymer and Hybrid Photovoltaic Thin Films: Organic vs Inorganic Acceptors. *J Phys Chem C* **2011**, *115* (49), 24403–24410. https://doi.org/10.1021/jp207514v.

(20) Chang, L.; Jacobs, I. E.; Augustine, M. P.; Moulé, A. J. Correlating Dilute Solvent Interactions to Morphology and OPV Device Performance. *Org Electron* **2013**, *14* (10), 2431–2443. https://doi.org/10.1016/j.orgel.2013.06.016.

(21) Liu, Z.; Sun, Y.; Yuan, J.; Wei, H.; Huang, X.; Han, L.; Wang, W.; Wang, H.; Ma, W. High-Efficiency Hybrid Solar Cells Based on Polymer/PbSxSe1-x Nanocrystals Benefiting from Vertical Phase Segregation. *Adv Mater* **2013**, *25* (40), 5772–5778. https://doi.org/10.1002/adma.201302340.

(22) Lan, X.; Voznyy, O.; Arquer, F. P. G. de; Liu, M.; Xu, J.; Proppe, A. H.; Walters, G.; Fan, F.; Tan, H.; Liu, M.; Yang, Z.; Hoogland, S.; Sargent, E. H. 10.6% Certified Colloidal Quantum

Dot Solar Cells via Solvent-Polarity-Engineered Halide Passivation. *Nano Lett* **2016**, *16* (7), 4630–4634. https://doi.org/10.1021/acs.nanolett.6b01957.

(23) Moulé, A. J.; Chang, L.; Thambidurai, C.; Vidu, R.; Stroeve, P. Hybrid Solar Cells: Basic Principles and the Role of Ligands. *J Mater Chem* **2011**, *22* (6), 2351–2368. https://doi.org/10.1039/c1jm14829j.

(24) Chen, Y.; Munechika, K.; Plante, I. J.-L.; Munro, A. M.; Skrabalak, S. E.; Xia, Y.; Ginger, D. S. Excitation Enhancement of CdSe Quantum Dots by Single Metal Nanoparticles. *Appl Phys Lett* **2008**, *93* (5), 053106. https://doi.org/10.1063/1.2956391.

(25) Munro, A. M.; Ginger, D. S. Photoluminescence Quenching of Single CdSe Nanocrystals by Ligand Adsorption. *Nano Lett* **2008**, *8* (8), 2585–2590. https://doi.org/10.1021/nl801132t.

(26) Munro, A. M.; Plante, I. J.-L.; Ng, M. S.; Ginger, D. S. Quantitative Study of the Effects of Surface Ligand Concentration on CdSe Nanocrystal Photoluminescence. *J Phys Chem C* **2007**, *111* (17), 6220–6227. https://doi.org/10.1021/jp068733e.

(27) Colbert, A. E.; Wu, W.; Janke, E. M.; Ma, F.; Ginger, D. S. Effects of Ligands on Charge Generation and Recombination in Hybrid Polymer/Quantum Dot Solar Cells. *J Phys Chem C* **2015**, *119* (44), 24733–24739. https://doi.org/10.1021/acs.jpcc.5b07828.

(28) Hickey, R. T.; Jedlicka, E.; Pokuri, B. S. S.; Colbert, A. E.; Bedolla-Valdez, Z. I.; Ganapathysubramanian, B.; Ginger, D. S.; Moulé, A. J. Morphological Consequences of Ligand Exchange in Quantum Dot - Polymer Solar Cells. *Org Electron* **2018**, *54*, 119–125. https://doi.org/10.1016/j.orgel.2017.12.018.

(29) Todorov, T. K.; Tang, J.; Bag, S.; Gunawan, O.; Gokmen, T.; Zhu, Y.; Mitzi, D. B. Beyond 11% Efficiency: Characteristics of State-of-the-Art Cu2ZnSn(S,Se)4 Solar Cells. *Adv Energy Mater* **2013**, *3* (1), 34–38. https://doi.org/10.1002/aenm.201200348.

(30) Yan, C.; Huang, J.; Sun, K.; Johnston, S.; Zhang, Y.; Sun, H.; Pu, A.; He, M.; Liu, F.; Eder, K.; Yang, L.; Cairney, J. M.; Ekins-Daukes, N. J.; Hameiri, Z.; Stride, J. A.; Chen, S.; Green, M. A.; Hao, X. Cu2ZnSnS4 Solar Cells with over 10% Power Conversion Efficiency Enabled by Heterojunction Heat Treatment. *Nat Energy* **2018**, *3* (9), 764–772. https://doi.org/10.1038/s41560-018-0206-0.

(31) Su, Z.; Liang, G.; Fan, P.; Luo, J.; Zheng, Z.; Xie, Z.; Wang, W.; Chen, S.; Hu, J.; Wei, Y.; Yan, C.; Huang, J.; Hao, X.; Liu, F. Device Postannealing Enabling over 12% Efficient Solution-Processed Cu2ZnSnS4 Solar Cells with Cd2+ Substitution. *Adv Mater* **2020**, *32* (32), 2000121. https://doi.org/10.1002/adma.202000121.

(32) Liu, F.; Wu, S.; Zhang, Y.; Hao, X.; Ding, L. Advances in Kesterite Cu2ZnSn(S, Se)4 Solar Cells. *Sci Bull* **2020**, *65* (9), 698–701. https://doi.org/10.1016/j.scib.2020.02.014.

(33) Li, J.; Huang, Y.; Huang, J.; Liang, G.; Zhang, Y.; Rey, G.; Guo, F.; Su, Z.; Zhu, H.; Cai, L.; Sun, K.; Sun, Y.; Liu, F.; Chen, S.; Hao, X.; Mai, Y.; Green, M. A. Defect Control for 12.5% Efficiency Cu2ZnSnSe4 Kesterite Thin-Film Solar Cells by Engineering of Local Chemical Environment. *Adv Mater* **2020**, *32* (52), 2005268. https://doi.org/10.1002/adma.202005268.

(34) Son, D.-H.; Kim, S.-H.; Kim, S.-Y.; Kim, Y.-I.; Sim, J.-H.; Park, S.-N.; Jeon, D.-H.; Hwang, D.-K.; Sung, S.-J.; Kang, J.-K.; Yang, K.-J.; Kim, D.-H. Effect of Solid-H 2 S Gas Reactions on CZTSSe Thin Film Growth and Photovoltaic Properties of a 12.62% Efficiency Device. *J Mater Chem A* **2019**, *7* (44), 25279–25289. https://doi.org/10.1039/c9ta08310c.

(35) Wang, W.; Winkler, M. T.; Gunawan, O.; Gokmen, T.; Todorov, T. K.; Zhu, Y.; Mitzi, D. B. Device Characteristics of CZTSSe Thin-Film Solar Cells with 12.6% Efficiency. *Adv Energy Mater* **2014**, *4* (7), 1301465. https://doi.org/10.1002/aenm.201301465.

(36) Bourdais, S.; Choné, C.; Delatouche, B.; Jacob, A.; Larramona, G.; Moisan, C.; Lafond, A.; Donatini, F.; Rey, G.; Siebentritt, S.; Walsh, A.; Dennler, G. Is the Cu/Zn Disorder the Main Culprit for the Voltage Deficit in Kesterite Solar Cells? *Adv Energy Mater* **2016**, *6* (12), 1502276. https://doi.org/10.1002/aenm.201502276.

(37) Kim, S.; Park, J.-S.; Walsh, A. Identification of Killer Defects in Kesterite Thin-Film Solar Cells. *Acs Energy Lett* **2018**, *3* (2), 496–500. https://doi.org/10.1021/acsenergylett.7b01313.

(38) Ma, S.; Li, H.; Hong, J.; Wang, H.; Lu, X.; Chen, Y.; Sun, L.; Yue, F.; Tomm, J. W.; Chu, J.; Chen, S. Origin of Band-Tail and Deep-Donor States in Cu 2 ZnSnS 4 Solar Cells and Their Suppression through Sn-Poor Composition. *J Phys Chem Lett* **2019**, *10* (24), 7929–7936. https://doi.org/10.1021/acs.jpclett.9b03227.

(39) Li, J.; Yuan, Z.-K.; Chen, S.; Gong, X.-G.; Wei, S.-H. Effective and Noneffective Recombination Center Defects in Cu 2 ZnSnS 4 : Significant Difference in Carrier Capture Cross Sections. *Chem Mater* **2019**, *31* (3), 826–833. https://doi.org/10.1021/acs.chemmater.8b03933.

(40) Nisika; Kaur, K.; Kumar, M. Progress and Prospects of CZTSSe/CdS Interface Engineering to Combat High Open-Circuit Voltage Deficit of Kesterite Photovoltaics: A Critical Review. *J Mater Chem A* **2020**, *8* (41), 21547–21584. https://doi.org/10.1039/d0ta06450e.

(41) Kumar, M.; Dubey, A.; Adhikari, N.; Venkatesan, S.; Qiao, Q. Strategic Review of Secondary Phases, Defects and Defect-Complexes in Kesterite CZTS–Se Solar Cells. *Energ Environ Sci* **2015**, *8* (11), 3134–3159. https://doi.org/10.1039/c5ee02153g.

(42) Gong, Y.; Qiu, R.; Niu, C.; Fu, J.; Jedlicka, E.; Giridharagopal, R.; Zhu, Q.; Zhou, Y.; Yan, W.; Yu, S.; Jiang, J.; Wu, S.; Ginger, D. S.; Huang, W.; Xin, H. Ag Incorporation with Controlled Grain Growth Enables 12.5% Efficient Kesterite Solar Cell with Open Circuit Voltage Reached 64.2% Shockley–Queisser Limit. *Adv Funct Mater* **2021**, 2101927. https://doi.org/10.1002/adfm.202101927.

(43) Gong, Y.; Zhang, Y.; Jedlicka, E.; Giridharagopal, R.; Clark, J. A.; Yan, W.; Niu, C.; Qiu, R.; Jiang, J.; Yu, S.; Wu, S.; Hillhouse, H. W.; Ginger, D. S.; Huang, W.; Xin, H. Sn4+ Precursor Enables 12.4% Efficient Kesterite Solar Cell from DMSO Solution with Open Circuit Voltage Deficit below 0.30 V. *Sci China Mater* **2021**, *64* (1), 52–60. https://doi.org/10.1007/s40843-020-1408-x.

(44) Kamada, R.; Yagioka, T.; Adachi, S.; Handa, A.; Tai, K. F.; Kato, T.; Sugimoto, H. New World Record Cu(In,Ga)(Se,S)2 Thin Film Solar Cell Efficiency Beyond 22%. *IEEE 43rd Photovoltaic Specialists Conference (PVSC)* **2016**, 1287–1291.

(45) Nakamura, M.; Yoneyama, N.; Horiguchi, K.; Iwata, Y.; Yamaguchi, K.; Sugimoto, H.; Kato, T. Recent R&D Progress in Solar Frontier's Small-Sized Cu(InGa)(SeS)2 Solar Cells. *IEEE 40th Photovoltaic Specialist Conference (PVSC)* **2014**, 0107–0110.

(46) Hages, C. J.; Koeper, M. J.; Miskin, C. K.; Brew, K. W.; Agrawal, R. Controlled Grain Growth for High Performance Nanoparticle-Based Kesterite Solar Cells. *Chem Mater* **2016**, *28* (21), 7703–7714. https://doi.org/10.1021/acs.chemmater.6b02733.

(47) Adurodija, F. O.; Song, J.; Kim, S. D.; Kwon, S. H.; Kim, S. K.; Yoon, K. H.; Ahn, B. T. Growth of CuInSe2 Thin Films by High Vapour Se Treatment of Co-Sputtered Cu-In Alloy in a Graphite Container. *Thin Solid Films* **1999**, *338* (1–2), 13–19. https://doi.org/10.1016/s0040-6090(98)00358-7.

(48) Chernomordik, B. D.; Ketkar, P. M.; Hunter, A. K.; Béland, A. E.; Deng, D. D.; Aydil, E. S. Microstructure Evolution During Selenization of Cu2ZnSnS4 Colloidal Nanocrystal Coatings. *Chem Mater* **2016**, *28* (5), 1266–1276. https://doi.org/10.1021/acs.chemmater.5b02462.

(49) Bertram, T.; Depredurand, V.; Siebentritt, S. Electrical Characterization of Defects in Cu-Rich Grown CuInSe2 Solar Cells. *EEE Journal of Photovoltaics* **2016**, *6* (2), 546–551. https://doi.org/0.1109/JPHOTOV.2015.2508239.

(50) Aida, Y.; Depredurand, V.; Larsen, J. K.; Arai, H.; Tanaka, D.; Kurihara, M.; Siebentritt, S. Cu-rich CuInSe2 Solar Cells with a Cu-poor Surface. *Prog Photovoltaics Res Appl* **2015**, *23* (6), 754–764. https://doi.org/10.1002/pip.2493.

(51) Buffière, M.; Mel, A. E.; Lenaers, N.; Brammertz, G.; Zaghi, A. E.; Meuris, M.; Poortmans, J. Surface Cleaning and Passivation Using (NH4)2S Treatment for Cu(In,Ga)Se2 Solar Cells: A Safe Alternative to KCN. *Adv Energy Mater* **2015**, *5* (6), 1401689. https://doi.org/10.1002/aenm.201401689.

(52) Jiang, J.; Yu, S.; Gong, Y.; Xin, H. 10.3% Efficient CuIn(S,Se)2 Solar Cells from DMF Molecular Solution with the Absorber Selenized under High Argon Pressure. *2018 IEEE 7th World Conference on Photovoltaic Energy Conversion (WCPEC) (A Joint Conference of 45th IEEE PVSC, 28th PVSEC & 34th EU PVSEC)* **2018**, 0831–0834. https://doi.org/10.1109/pvsc.2018.8548027.

(53) Jiang, J.; Yu, S.; Gong, Y.; Yan, W.; Zhang, R.; Liu, S.; Huang, W.; Xin, H. 10.3% Efficient CuIn(S,Se)2 Solar Cells from DMF Molecular Solution with the Absorber Selenized under High Argon Pressure. *Sol Rrl* **2018**, *2* (6), 1800044. https://doi.org/10.1002/solr.201800044.

(54) Jiang, J.; Giridharagopal, R.; Jedlicka, E.; Sun, K.; Yu, S.; Wu, S.; Gong, Y.; Yan, W.; Ginger, D. S.; Green, M. A.; Hao, X.; Huang, W.; Xin, H. Highly Efficient Copper-Rich Chalcopyrite Solar Cells from DMF Molecular Solution. *Nano Energy* **2020**, *69* (69), 104438. https://doi.org/10.1016/j.nanoen.2019.104438.

(55) Choi, P.-P.; Cojocaru-Mirédin, O.; Wuerz, R.; Raabe, D. Comparative Atom Probe Study of Cu(In,Ga)Se2 Thin-Film Solar Cells Deposited on Soda-Lime Glass and Mild Steel Substrates. *J Appl Phys* **2011**, *110* (12), 124513. https://doi.org/10.1063/1.3665723.

(56) Rudmann, D.; Cunha, A. F. da; Kaelin, M.; Kurdesau, F.; Zogg, H.; Tiwari, A. N.; Bilger, G. Efficiency Enhancement of Cu(In,Ga)Se2 Solar Cells Due to Post-Deposition Na Incorporation. *Appl Phys Lett* **2004**, *84* (7), 1129–1131. https://doi.org/10.1063/1.1646758.

(57) Yuan, Z.; Chen, S.; Xie, Y.; Park, J.; Xiang, H.; Gong, X.; Wei, S. Na-Diffusion Enhanced P-type Conductivity in Cu(In,Ga)Se2: A New Mechanism for Efficient Doping in Semiconductors. *Adv Energy Mater* **2016**, *6* (24), 1601191. https://doi.org/10.1002/aenm.201601191.

(58) Forest, R. V.; Eser, E.; McCandless, B. E.; Chen, J. G.; Birkmire, R. W. Reversibility of (Ag,Cu)(In,Ga)Se2 Electrical Properties with the Addition and Removal of Na: Role of Grain Boundaries. *J Appl Phys* **2015**, *117* (11), 115102. https://doi.org/10.1063/1.4915334.

Chapter 3. Bismuth Doping Alters Structural Phase Transitions in Methylammonium Lead Tribromide Single Crystals

Adapted with permissions from Jedlicka, E.; Wang, J.; Mutch, J.; Jung, Y.-K.; Went, P.; Mohammed, J.; Ziffer, M. Z.; Giridharagopal, R.; Walsh, A.; Chu, J,-H.; Ginger, D. S. Bismuth Doping Alters Structural Phase Transitions in Methylammonium Lead Tribromide Single Crystals. *J. Phys. Chem. Lett.* **2021**, 12, 2749-2755, DOI: 10.1021.acs.jpclett.1c00334

3.1 Overview

We study the effects of bismuth doping on the crystal structure and phase transitions in single crystals of the perovskite semiconductor methylammonium lead tribromide, $MAPbBr_3$. By measuring temperature-dependent specific heat capacity (C_p) we find that, as Bi doping increases, the phase transition assigned to the cubic to tetragonal phase boundary decreases in temperature. Furthermore, after doping we observe one phase transition between 135 and 155 K, in contrast to two transitions observed in the undoped single crystal. These results appear strikingly similar to previously reported effects of mechanical pressure on perovskite crystal structure. Using X-ray diffraction, we show that the lattice constant decreases as Bi is incorporated into the crystal, as predicted by density functional theory (DFT). We propose that bismuth substitutional doping on the lead site is dominant, resulting in Bi_{Pb}^{+} centers which induce compressive chemical strain that alters the crystalline phase transitions.

3.2 Introduction

Halide perovskites have emerged as promising semiconductor materials for applications including solar cells, light-emitting diodes, photodetectors, and lasers.[1-4] They exhibit unique and tunable optoelectronic properties via facile tailoring of the chemical composition of the structure. In the archetypal perovskite ABX_3 crystal structure, A represents a monovalent cation species ($A = Cs^{+}$, $CH_3NH_3^{+}$ (MA^{+}), or $(NH_2)_2CH3^{+}$ (FA^{+})), B represents a divalent cation ($B = Pb^{+2}$, Sn^{+2}), and X represents a halide ($X = Cl^{-}$, Br^{-}, I^{-}). Diverse electronic and structural motifs are thereby accessible by modification of the chemical composition and the dimensionality of the material.[5] Doping provides an additional lever for changing the properties of lead halide perovskites by substituting a selected impurity into the crystal at low concentrations. Several dopant species, including Bi^{3+}, Cd^{2+}, K^{+}, Mn^{2+}, Ce^{3+}, Yb^{3+}, and Eu^{3+},[5-13] have been studied regarding their effects on the optoelectronic properties of the lead halide perovskites. However, there have been relatively fewer studies of how doping, defects, and impurities affect the structural properties of halide perovskites crystals and nanocrystals. Doping and defects can affect temperature-dependent phase transition behavior and can alter of the lattice constant and strain.[13-15] Understanding these phenomena is important for tailoring materials properties, and for engineering materials with improved stability in varying operational conditions.

In this work, we study the effects of dopant inclusion on the crystal structure in a series of single crystals of the hybrid organic-inorganic lead halide perovskite, methylammonium lead tribromide

($MAPbBr_3$) with various amounts of bismuth doping. We chose this system for several reasons. First, the optoelectronic properties of bismuth-doped perovskites have been well characterized, among many other dopants, e.g. quenching of visible photoluminescence with corresponding near-infrared (NIR) emission, increasing conductivity, increased free carrier concentrations, and increased carrier lifetimes.[6-10,13,16] Secondly, recently developed crystallization methods for $MAPbBr_3$ report rapid growth of high purity macroscopic mm-sized single crystals with bismuth doping[6-10,17,18] which offer an ideal platform to study the intrinsic dopant effects on the crystal structure without the complication of extrinsic influences such as surfaces or grain boundaries.[19] Finally, a number of studies on the crystal structure and phase transitions of undoped $MAPbBr_3$ are available, under both atmospheric conditions and under external pressure, providing a firm literature basis for further analysis.[20-26]

Here, we investigate the effects of Bi doping on the phase transition behavior of $MAPbBr_3$ single crystals using specific heat capacity measurements (C_p). We show that as the Bi-doping level increases the temperature decreases for the phase-transition assigned to the cubic to tetragonal phase of $MAPbBr_3$. Additionally, upon incorporation of bismuth into the $MAPbBr_3$ crystal lattice we observe a single phase transition between 135 K and 155 K instead of the two phase transitions in that temperature range observed in the undoped $MAPbBr_3$ crystal. These changes in phase-transition behavior occur alongside a lattice contraction induced by the Bi substitutional doping at the Pb site. We compare the lattice contraction observed in X-ray diffraction (XRD) to first-principles predictions at the various doping levels for both Bi_{Pb}^{0} and Bi_{Pb}^{+} defect sites. We propose the incorporation of Bi occurs through a Bi_{Pb}^{+} defect site, which induces compressive chemical strain, resulting in a lattice contraction and the changes in the phase transition behavior.

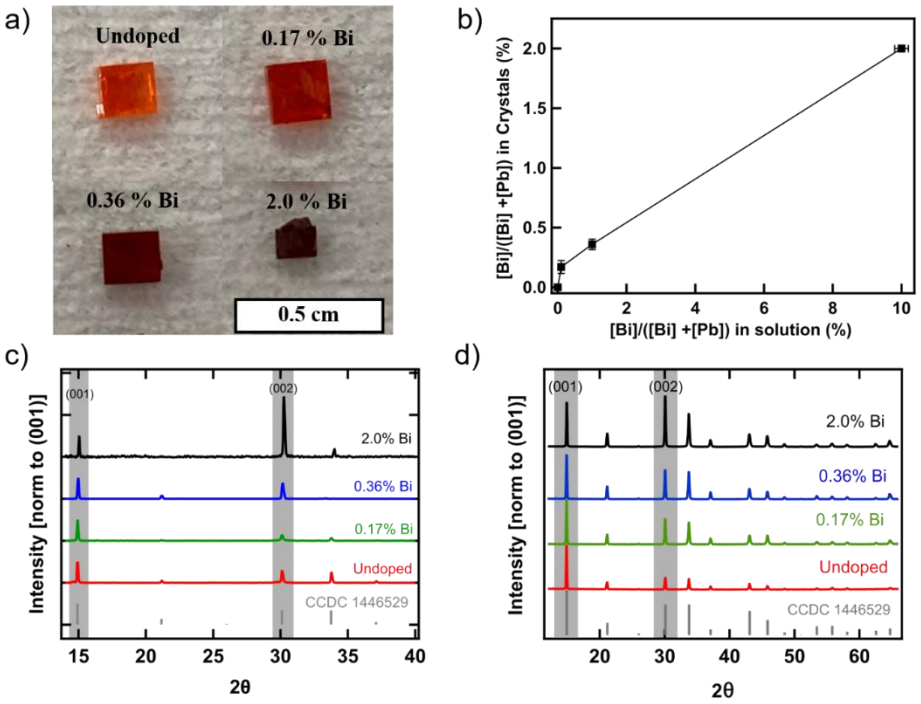

Figure 3.1: Characterization of $MAPbBr_3$ single crystals with various levels of bismuth doping. (a) $MAPbBr_3$ single crystals, (b) ratio of Bi to total amount of Pb and Bi in single crystals verses the growth solution, (c) single crystal X-ray diffraction patterns, (d) powder X-ray diffraction patterns.

3.3 Bismuth doping in $MAPbBr_3$ single crystals

We grow single-crystal $MAPbBr_3$ that incorporate various concentrations of bismuth following the inverse temperature crystallization method reported by Nayak and coworkers.[6] Detailed growth methods are provided in Supporting Information. **Figure 3.1a** shows as-prepared $MAPbBr_3$ single crystals with increasing bismuth concentration. As previously reported, we observe that bismuth doping induces strong changes in color for $MAPbBr_3$ single crystals, from translucent orange (undoped) to an increasingly darker red color (from 0.1% to 1%), then to opaque black at the highest Bi-doping (10%) levels.[6-8] This color change has been attributed to an increasing number of sub-band-gap states with increasing Bi-doping level.[6]

To quantify the bismuth-doping level in our single crystals, which can differ from the amount of Bi added to the growth solution,[6,7] we use inductively-coupled-plasma optical emission spectrometry (ICP-OES) to determine the ratio of bismuth to lead in our single crystals. **Figure 3.1b** shows a plot of the ICP-OES measured Bi concentration in the final crystal, as a function of the Bi concentration in the growth solution. As shown in **Fig. 3.1b**, we observe increasing bismuth concentration for crystals grown with higher bismuth concentrations in solution and confirm no detectable bismuth concentration in our undoped samples. We report final bismuth concentrations of 0.17%, 0.36%, and 2.0% for the 0.1%, 1%, and 10% bismuth solutions, respectively. In agreement with previous reports, we find that, at high concentrations of bismuth in the growth solution, the concentration of bismuth incorporated into the crystal is lower than the concentration of bismuth in the growth solution.[6,7]

Figures 3.1c and **3.1d** show the XRD patterns, intensity normalized to the (001) plane, on both $MAPbBr_3$ single crystal and crushed powders, respectively. Both XRD show that the diffraction patterns after Bi-doping agrees with the undoped $MAPbBr_3$ reference pattern reported by Jaffe and co-workers[27] and consistent with previous reports.[6-8] We note that the (002) plane diffraction intensity increases, with respect to (001), as the bismuth level in the crystal increases. Such an increasing trend in (002) to (001) intensity in bismuth-doping level can be found in the XRD patterns in other literature reports,[6-8] though the effect was not discussed or explained. We propose that the observed increasing (002)/(001) ratio upon Bi-doping indicates increasing lattice disorder in the Bi-doped single crystals. Previous studies on undoped crystals have similarly correlated increases in the (002)/(001) intensity ratio with increasing long-range disorder as verified by far-infrared reflection (FIR) spectroscopy.[28] More ordered $MAPbBr_3$ crystals, those with less stacking faults or dislocations as quantified by a higher far-infrared reflectance intensity, also exhibit higher (001) diffraction peak intensities with respect to their (002) planes. This result is also consistent with the optical microscopy images (Fig. S1), where we clearly resolve hillock-like crystalline growing fronts in the undoped crystal. We observe fewer such growth fronts on the 0.17% Bi-doped crystal, and no such front on the 0.36% and 2.0% Bi-doped crystals suggesting less long-range order.

3.4 Altered structural phase transition behavior in bismuth doped $MAPbBr_3$

Next, to understand the potential impact of the Bi-doping on the phase transition behaviors, we perform temperature-dependent specific heat capacity measurements as a function of bismuth-doping concentration. Specific heat capacity measurements have been applied to study the

temperature-dependent phase transition behaviors of lead halide perovskites, which have been demonstrated to depend both on the A-site alloying (FA, Cs) and X-site halide selection,[20,29] however the effects of B-site doping and substitution are less explored. Recently, Ma and co-workers showed that replacing Pb^{2+} with Ni^{2+} on the B-site in $CsPbCl_3$ nanocrystals altered the local structure of the doped regions and inhibited the cubic to orthorhombic phase transition.[15] Here we expect that heterovalent B-site doping, such as Bi^{3+} on Pb^{2+}, might also alter the phase transition behavior.

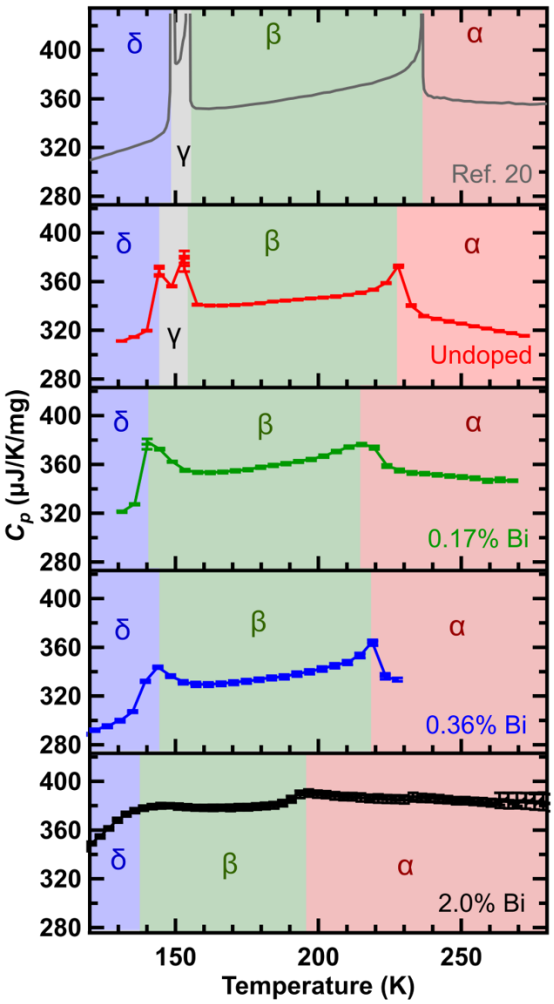

Figure 3.2: Temperature-dependent specific heat capacity (C_p) for various levels of bismuth doping. Phase transitions are color coded as: Red: cubic phase (α); Green: tetragonal phase I (β); Gray: tetragonal phase II (γ); Blue: orthorhombic (δ).

Figure 3.2 shows the heat capacity as measured using a Physical Properties Measurement System (PPMS) Dynacool™ (Quantum Design) for four $MAPbBr_3$ samples with different Bi-doping levels. Additionally, we show a reference C_p vs. T plot with phase assignments as reported by Onoda-Yamamuro and co-workers.[20] In **Fig. 3.2**, the baseline represents the normal part heat capacity as a result of different vibrational modes, whereas the transitional peaks correspond to the $MAPbBr_3$ phase transition temperatures.[20] We observe three phase transitions in our undoped $MAPbBr_3$ crystals, which we determine from where the first derivative of the specific heat capacity

equals zero. The peaks we measure for the undoped sample agree well with those measured by Onoda-Yamamuro et. al.

Following the previous phase transition assignments,[30,31] we identify them as: (1) the transition between α-$MAPbBr_3$, cubic (Pm3m), and β-$MAPbBr_3$, tetragonal (I4/mcm), at 228 K; (2) the transition between β-$MAPbBr_3$, tetragonal (I4/mcm), and γ-$MAPbBr_3$, tetragonal (P4/mmm), at 153 K; and (3) the transition between γ-$MAPbBr_3$, tetragonal (P4/mmm), and δ-$MAPbBr_3$, orthorhombic (Pnma), at 144 K. We assign space groups for the cubic and tetragonal phases according to studies by Poglitsch and Weber.[30] For the low temperature orthorhombic phase, we follow the assignment from Swainson and co-workers,[31] in which they suggest that Pnma space group yields more satisfactory refinement without missing symmetry, compared to previously reported $Pna2_1$ assignment. For the convenience of the reader, we have included the detailed crystal structure information for the different phases of $MAPbBr_3$ in SI Table 1. After Bi doping, we observe a few additional features: (1) the temperature of the phase transition between the cubic phase (α) to the tetragonal phase (β) shifts to lower temperatures, as seen by the expansion of the cubic phase in Figure 2, represented by the red-shaded region of the plot for the bismuth-doped samples; (2) only one low-temperature phase transition between tetragonal and orthorhombic, as seen by the disappearance of the doublet peaks near 150K likely indicating the loss of the lower temperature tetragonal phase (γ);[26] (3) at the doping level increases, phase transition peaks become less definitive but turn to gradual bumpy transition features. We note that the highest doping level (2%) crystals show greater sample-to-sample variations, as seen in Figure S2, which yet all follow the above trends qualitatively. We attribute these variations to the wider range of crystallization temperatures we observed for the 2% Bi doped single crystals. We speculate that the 2.0% Bi single crystals thus have more variation in local crystallinity which could alter the C_p behavior between samples with the same nominal concentration of bismuth.

3.5 Bismuth doping induces lattice compression.

To understand the origin and implication of these observations, we compare them with similar behaviors found on the undoped $MAPbBr_3$ single crystal phase transition under external pressure. Onoda-Yamamuro et. al. have shown that (**Fig. 3.3a**, dashed lines w.r.t. top axis), for undoped $MAPbBr_3$ single crystals, as the external mechanical pressure increases, (1) the transition between the cubic phase and the tetragonal phase shifts to lower temperatures, and (2) the doublet peaks corresponding to the two tetragonal phases near 150K disappear.[21] The cause of the pressure-induced behavior is understood to be due to the unit cell volume reduction through tilting and shrinking of the $PbBr_6$ octahedra.[32] The presence of two tetragonal phases, I4/mcm (β) at higher temperature and P4/mmm (γ) at lower temperature, is unique to $MAPbBr_3$, contrasting with $MAPbCl_3$ and $MAPbI_3$ which each have only one tetragonal phase. Onoda-Yamamuro and co-workers mention that the lower temperature tetragonal (γ) phase for $MAPbBr_3$ corresponds to the P4/mmm tetragonal phase of $MAPbCl_3$ and the higher temperature tetragonal (β) phase corresponds to the I4/mcm tetragonal phase of $MAPbI_3$.[20] Khanal and co-workers attributed the formation of either P4/mmm or I4/mcm tetragonal phase to the B-X bond. In P4/mmm, the smaller octahedral volume prevents the free rotation of the MA^+ ions that can occur with larger octahedra in the I4/mcm space group, thus $MAPbI_3$ with a larger Pb-I bond length forms I4/mcm tetragonal phase while $MAPbCl_3$ with a shorter distance for the Pb-Cl bond length forms the P4/mmm tetragonal phase.[33] When $MAPbBr_3$ crystals are subjected to pressure, the volume of the unit cell and the Pb-Br bond length decreases.[34] This results in the disappearance of the P4/mmm (γ) phase

in pressures above 43.2 MPa.[21] Chemical doping with Bi causes similar strain as the effective ionic radius of Bi^{3+} (1.03Å) is smaller than Pb^{2+} (1.19Å),[34] and should lead to a reduction of the lattice constant/volume, mimicking the effect of external strain, hence also inducing the disappearance of the P4/mmm (γ) phase. By closely examining the single crystal XRD data (**Fig. 3.3b & 3.3c**, zoom-in of **Fig. 3.1c**), we observe that the diffraction plane positions shift to a higher angle, indicating a contraction of the crystal with increasing doping concentration. Notably, we only observe such a shift to higher diffraction angles on doping when performing XRD on single crystals. For the Bi-doped crystals, after crushing them into powders and performing XRD again, we observe that the diffraction planes return to the same position as the undoped crystals (**Fig. S3**), implying that strain builds up in the Bi-doped single crystal, and relaxes (possibly to the surface) after grinding. Previous studies also report that strain exists in Bi-doped $MAPbBr_3$ single crystals, where a broadening of the diffraction peak is observed instead of the shifting to a higher angle.[6] This result implies that a homogeneous strain exists in their system rather than the dominant compressive strain in our sample series, which might be due to subtle growth differences in the single crystals.

Fig. 3.3a plots the sample phase transition temperatures as a function of the lattice constants extracted from XRD. Here the top and bottom axis are registered following a previous study on undoped $MAPbBr_3$ lattice constants under external pressure.[34] The shift to a lower temperature of the cubic to tetragonal phase transition, as well as the disappearance of two tetragonal phases upon Bi doping, closely resembles the structural effects induced by an external pressure. The tetragonal to orthorhombic phase transition temperature, however, stays relatively unchanged.

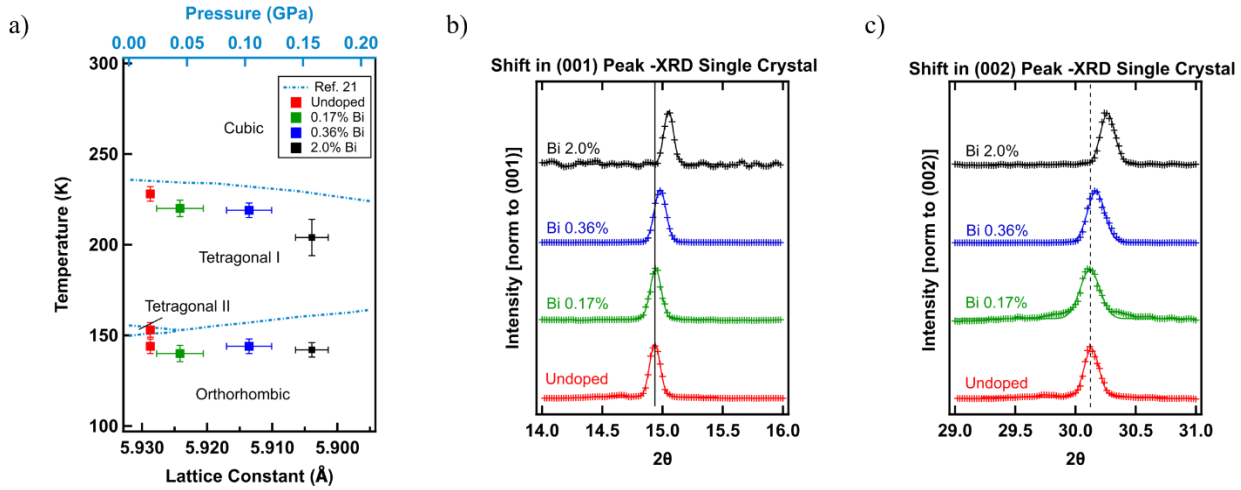

Figure 3.3: (a) Phase transition temperatures for pure $MAPbBr_3$ as a function of increasing pressure (blue lines, Ref. 21) and for increasing levels of Bi doping as a function of the lattice spacing. The lattice constant (bottom axis) and pressure (top axis) are registered according to a pressure-dependent $MAPbBr_3$ lattice constant study, Ref. 34 (b, c) Single crystal X-ray diffraction (XRD) showing shifts in (001) and (002) peaks to higher diffraction angles.

3.6 Density-functional-theory calculations of defect induced lattice compression

Finally, we perform density-functional-theory (DFT) calculations to examine the effects of the Bi dopant type on the lattice. Bi can be incorporated through a substitution on the Pb site by

either Bi^{3+} (Bi_{Pb}^{+}), which donates an electron into the lattice, or an effective Bi^{2+} species that would result with a neutral defect species (Bi_{Pb}^{0}). Hence, we decided to consider two different charge state of Bi on Pb site. Fig. 4a shows the optimized supercell and octahedral structures. The calculated volume of the $[BiBr_6]^{3-}$ (Bi_{Pb}^{+}) octahedron is 10% smaller than the $[PbBr_6]^{4-}$ octahedron in the $MAPbBr_3$ lattice, while the $[BiBr6]^{4-}$ (Bi_{Pb}^{0}) octahedron has similar volume to the $[PbBr_6]^{4-}$. This indicates that shorter length of Bi-Br bonding compared to Pb-Br bonding can induce the lattice shrinkage. Since it is computationally demanding to model dilute defect concentration within DFT framework, we employed $2 \times 2 \times 2$ supercell of cubic $MAPbBr_3$ that contains 96 atoms and adopted the thermodynamic model of defect pressure.[36] Based on the model, we calculated the change of the lattice spacing (a_d) as functions of Bi_{Pb}^{+} and Bi_{Pb}^{0} concentration following

$$a_d = a_0(1 + nv_d)^{\frac{1}{3}} \quad (1)$$

where a_0 is the lattice constant of the pristine cell, n is the defect concentration (defect/cm^{-3}), and v_d is the volume of the defect (Å^3/defect).[36] The defect volume v_d is derived according to

$$v_d = \frac{p_d * V_0}{B_0} \quad (2)$$

and

$$p_d = -\left(\frac{\Delta(E^{defect}(V) - E^{host}(V))}{\Delta V}\right) \quad (3)$$

where V_0 is the volume of the pristine cell (Å^3/atom), B_0 is the bulk modulus (18.18 GPa), and p_d is the defect pressure (GPa) calculated from eq 3 using E^{defect} and E^{host} , which are the DFT total energy of the defective and pristine cell (in eV), respectively

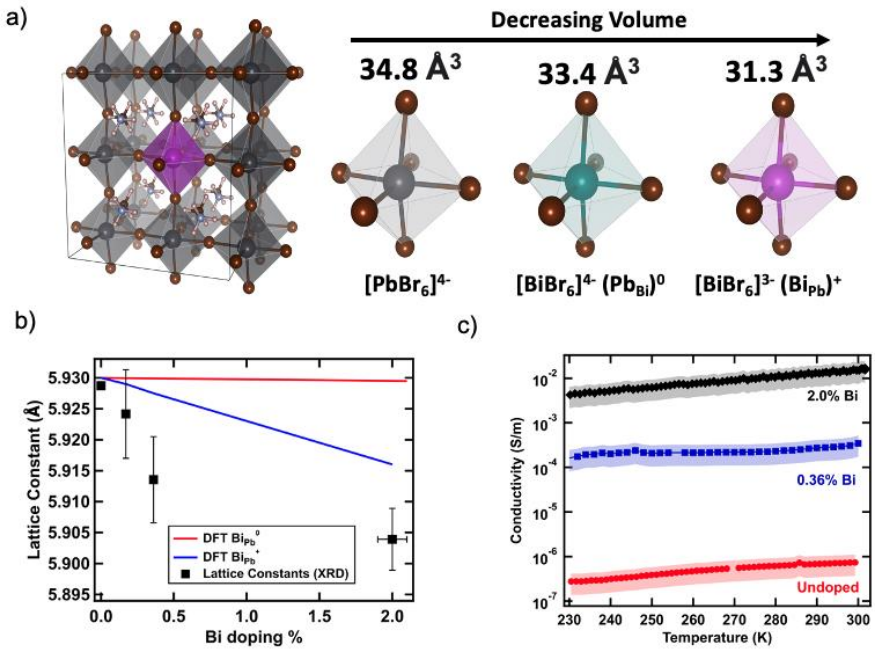

Figure 3.4: (a) Optimized structure of $MAPbBr_3$ 2 x 2 x 2 super cell geometry of octahedra in $MAPbBr_3$ lattice depending on center ions; (b) Lattice constants determined through DFT calculation (red and blue lines) and XRD (black markers); (c) Temperature-dependent conductivity measurements for single crystals.

Figure 3.4b shows the predicted lattice constant as a function of doping concentration. We find that the Bi_{Pb}^{+} dopant type exhibits a negative slope, similar to our experimental results, while the Bi_{Pb}^{0} dopant type suggests an almost invariant (slightly negative) lattice constant. Here, we note that the use of relatively small supercell with uniform Bi_{Pb} distribution does not take into account gradual strain change near defect sites, which could account for some of the quantitative discrepancy with actual experiment. However, the qualitative trend of lattice compression predicted for increasing Bi_{Pb}^{+} concentration is indeed consistent with the results from experiment. In addition, we note that Bi_{Pb}^{+} could interact with the native negatively charged defects, of which the most probable site are MA vacancies (V_{MA}^{-}) and bromine interstitials (Br_i^{-}), forming overall neutral-charged defect pairs, i.e. Bi_{Pb}-V_{MA} and Bi_{Pb}-Br_i.[5,9] We find that both V_{MA}^{-} and Br_i^{-} exhibit an increasing formation energy under pressure (Fig. S4), which implies that they have positive defect pressure that expands the lattice, i.e. they will mitigate the lattice contraction should there exist any bound pairs of Bi_{Pb}-V_{MA} or Bi_{Pb}-Br_i.

The conductivity measurements (**Fig. 3.4c**) show that the electrical conductivity increases orders of magnitude upon Bi doping, consistent with literature reports.[8,9] This provides circumstantial evidence that Bi_{Pb}^{+} does indeed form as a donor. From the conductivity measurements, and previous reports on carrier mobility as a function of Bi doping,[37] we estimate the electron carrier concentration to be ~$1x10^{13}$ cm^{-3}, $2x10^{16}$ cm^{-3}, and $1x10^{18}$ cm^{-3} for the undoped, 0.36% bismuth-doped, and 2.0% bismuth-doped samples, respectively. The doping efficiency, as defined by the ratio between carrier density and Bi dopant number, is therefore low (0.1~1%), which is a common feature of halide perovskites owing to efficient charge compensation mechanisms. When a charged donor is added, the system can respond by either increasing the electron carrier concentration or by forming compensating acceptor defects, for example, through methylammonium loss (V_{MA}), lead loss (V_{Pb}) or iodine gain (I_i). These compensating species could be distributed in the crystal or form bound complexes with Bi. The lack of quantitative agreement between the measurements and predictions for the lattice constants changes with Bi_{Pb}^{+} in Fig 4b is likely due to the nature of these compensating species, which are unresolved at present and will be the subject of further investigation.

3.7 Conclusion

In summary, we have demonstrated how doping can influence the structure and phase transitions of halide perovskites. We use specific heat capacity measurements to determine the transition temperatures for various levels of Bi-doped $MAPbBr_3$ single crystals. Bi-doping alters the phase transition behavior in $MAPbBr_3$ single crystals. Comparing with the effects of external pressure on the phase transition behaviors, we note that the resemble the effects of external pressure. This observation is consistent with the experimentally observed lattice contraction upon bismuth doping. We further compare DFT calculations with experimental data and suggest a charged bismuth species replacing Pb by forming Bi_{Pb}^{+} defects. These results provide new insight into how doping affects both the lattice structure and order in halide perovskites.

Appendix B

Supporting information for Chapter 3 including detailed single crystal growth, characterizations (XRD, ICP-OES, Microcalorimetry, conductivity), and DFT calculations.

Acknowledgement

This research was supported primarily by the National Science Foundation (NSF) through the UW Molecular Engineering Materials Center, a Materials Research Science and Engineering Center (DMR-1719797). Part of this work was conducted at the Molecular Analysis Facility, a National Nanotechnology Coordinated Infrastructure site at the University of Washington which is supported in part by the National Science Foundation (grant NNCI-1542101), the University of Washington, the Molecular Engineering & Science Institute, and the Clean Energy Institute. J.W. acknowledges the funding support from the Washington Research Foundation and Mistletoe Foundation postdoc fellowships. This work was also supported by a National Research Foundation of Korea (NRF) grant funded by the Korean government (MSIT) (No. 2018R1C1B6008728). Via our membership of the UK's HEC Materials Chemistry Consortium, which is funded by EPSRC (EP/L000202), this work used the ARCHER UK National Supercomputing Service (http://www.archer.ac.uk).

References

(1) Kim, J. Y.; Lee, J.; Jung, H. S.; Shin, H,; Park, N. High-Efficiency Perovskite Solar Cells. *Chem. Rev.* **2020**, 120, 7867-7918.

(2) Quan, L. N.; Rand, B. P.; Friend, R. H.; Mhaisalkar, S. G.; Lee, T.; Sargent, E. H. Perovskites for Next-Generation Optical Sources. *Chem. Rev.* **2019**, 119, 7444-7477.

(3) Chen, J.; Wang, J.; Xu, X.; Li, J.; Song, J.; Lan, S.; Liu, S.; Cai, B.; Han, B.; Precht, J.; Ginger, D. S.; Zeng, H. Efficient and Bright White Light-Emitting Diodes Based on Single-Layer Heterophase Halide Perovskites. *Nature Photonics* **2021,** 15, 238-244.

(4) DeQuilettes, D. W.; Frohna, K,; Emin, D.; Kirchartz, T.; Bulovic, V.; Ginger, D. S.; Stranks, S. D. Charge-Carrier Recombination in Halide Perovskites. *Chem. Rev.* **2019**, 119, 11007-11019.

(5) Manser, J. S.; Christians, J. A.; Kamat, P. V. Intriguing Optoelectronic Properties of Metal Halide Perovskites. *Chem. Rev.* **2016**, 116, 12956-13008.

(6) Nayak, P. K.; Sendner, M.; Wenger, B.; Wang, Z.; Sharma, K.; Ramadan, A. J.; Lovrinčić, R.; Pucci, A.; Madhu, P. K.; Snaith, H. J. Impact of Bi^{3+} Heterovalent Doping in the Organic-Inorganic Metal Halide Perovskites. *J. Am. Chem. Soc.***2018**, 140, 574-577.

(7) Abdelhady, A. L.; Saidaminov, M. I.; Murali, B.; Adinolfi, V.; Voznyy, O.; Katiev, K.; Alarousu, E.; Comin, R.; DUrsun, I.; Sinatra, L.; Sargent, E. H.; Mohammed, O. F.; Bakr, O. M. Heterovalent Dopant Incorporation for Bandgap and Type Engineering of Perovskite Crystals. *J. Phys. Chem. Lett.* **2016**, 7 , 295-301.

(8) Meng, R.; Guangbao, W.; Zhou, J.; Zhou, H.; Fang, H.; Loi, M. A.; Zhang, Y. Understanding the Impact of Bismuth Heterovalent Doping on the Structural and Photophysical Properties of $CH_3NH_3PbBr_3$ Halide Perovskite Crystals with Near-IR Photoluminescence. *Chem. Eur. J.* **2019**, 25, 5480-5488.

(9) Sun, P..; Kripalani, D. R.; Bai, L.; Zhou, K. Prediction of the Role of Bismuth Dopants in Organic–Inorganic Lead Halide Perovskites on Photoelectric Properties and Photovoltaic Performance. *J. Phys. Chem. C* **2019**, 123, 12684-12693.

(10) Hu, Y.; Bai, F.; Liu, X.; Ji, Q.; Miao, X.; Qiu, T.; Zhang, S. Bismuth Incorporation Stabilized α-$CsPbI_3$ for Fully Inorganic Perovskite Solar Cells. *ACS Energy Lett.* **2017**, *2* , 2219–2227.

(11) Zhou, Y.; Chen, J.; Bakr, O. M.; Sun, H. Metal-Doped Lead Halide Perovskites: Synthesis, Properties, and Optoelectronic Applications. *Chem. Mater.* **2018**, *30* , 6589-6613.

(12) Bala, A.; Kumar, V. A Study of Eu Doping in Nanolayers of $CsPbBr_3$ Using Ab Initio Calculations to Understand *f–f* Transitions in Eu^{3+}-Doped Nanocrystals for Light-Emitting Diodes. *ACS Appl. Nano Mater.* **2020**, 3, 4437-4444.

(13) Zhou, Y.; Yong, Z.; Zhang, K.; Liu, B.; Wang, Z.; Hou, J.; Fang, Y.; Zhou, Y.; Sun, H.; Song. B. Ultrabroad Photoluminescence and Electroluminescence at New Wavelengths from Doped Organometal Halide Perovskites. *J. Phys. Chem. Lett.* **2016**, 7, 2735-2741.

(14) Ma, J.; Yin, J.; Chen, Y.; Zhao, Q.; Zhou, Y.; Li, H.; Kuroiwa, Y.; Moriyoshi, C.; Li, Z.; Bakr, O. M.; Mohammed, O. F.; Sun, H. Defect-Triggered Phase Transition in Cesium Lead Halide Perovskite Nanocystals. *ACS Materials Lett.* **2019**, 1, 185-191.

(15) Ma, J.; Chen, J.; Yin, J.; Zhang, B.; Zhao, Q.; Kuroiwa, Y.; Moriyoshi, C.; Hu, L.; Bakr, O., M.; Mohammed, O., F.; Sun, H. Doping Induces Structural Phase Transitions in All-Inorganic Lead Halide Perovskite Nanocrystals. *ACS Materials Lett.* **2020**, 2, 367-375.

(16) Xie, A; Nguyen, T. H.; Hettiarachchi, C.; Witkowski, M. E.; Drozdowski, W.; Birowosuto, M. D.; Wang, H.; Dang, C. X-ray Luminescence in Undoped and Bismuth Doped Single Crystal Hybrid Lead Halide Perovskites. *Proc.* SPIE 10912, Physics and Simulation of Optoelectronic Devices XXVII, 109121G (26 February 2019); doi:10.1117/12.2509345.

(17) Saidaminov, M. I.; Abdelhady, A. L.; Murali, B.; Alarousu, E.; Burlakov, V. M.; Peng, W.; Dursun, I.; Wang, L.; He, Y.; Maculan, G.; Goriely, A.; Wu, T.; Mohammed, O. F.; Bakr, O. M. High-Quality Bulk Hybrid Perovskite Single Crystals within Minutes by Inverse Temperature Crystallization. *Nat. Commun.* **2015**, *6* (1), 7586.

(18) Nayak, P. K.; Moore, D. T.; Wenger, B.; Nayak, S.; Haghighirad, A. A.; Fineberg, A.; Noel, N. K.; Reid, O. G.; Rumbles, G.; Kukura, P.; Vincent, K. A.; Snaith, H. J. Mechanism for Rapid Growth of Organic-Inorganic Halide Perovskite Crystals. *Nat. Commun.* **2016**, 7, 13303.

(19) Shi, D.; Adinolfi, V.; Comin, R.; Yuan, M.; Alarousu, E.; Buin, A.; Chen, Y.; Hoogland, S.; Rothenberger, A.; Katsiev, K.; Losovyi, Y.; Zhang, X.; Dowben, P. A.; Mohammed, O. F.; Sargent, E. H.; Bakr, O. M. Low Trap-State Density and Long Carrier Diffusion in Organolead Trihalide Perovskite Single Crystals. *Science* **2015**, 347 (6221), 519-522.

(20) Onoda-Yamauro, N.; Matsuo, T.; Suga, H. Calormetric and IR Spectroscopic Studies of Phase Transitions in Methylammonium Trihalogenoplumbates (II). *J. Phys. Chem. Solids***1990**, 51 (12), 1383-1395.

(21) Onoda-Yamauro, N.; Yamamuro, O.; Matsuo, T.; Suga, H. *p-T* Relations of $CH_3NH_3PbX_3$ (X=Cl, Br, I) Crystals. *J. Phys. Chem. Solids* **1992**, 53 (2), 277-281.

(22) Wang, L.; Wang, K.; Zou, B. Pressure-Induced Structural and Optical Properties of Organometal Halide Perovskite-Based Formamidinium Lead Bromide. *J. Phys. Chem. Lett.* **2016**, 7, 2556-2562.

(23) Hirostu, S.; Harada, J.; Iizumi, M.; Gesi, K. Structural Phase Transitions in $CsPbBr_3$. *J. Phys. Soc. Jpn.* **1974**, 37 (5), 1393-1398.

(24) Lee, Y.; Mitzi, D. B.; Barnes, P. W.; Vogt, T. Pressure-Induced Phase Transitions and Templating Effect in Three-Dimensional Organic-Inorganic Hybrid Perovskites. *Phys. Rev. B* **2003,** 68, 020103(R).

(25) Jaffe, A.; Yu, L.; Karunadasa, H. I. Halide Perovskite Under Pressure: Accessing New Properties Through Lattice Compression. *ACS Energy Lett.* **2017**, 2, 1549-1555.

(26) Szafrański, M.; Katrusiak, A. Photovoltaic Hybrid Perovskites under Pressure. *J. Phys. Chem. Lett.* **2017**, 8, 2496-2506.

(27) Jaffe, A.; Yu, L.; Beavers, C. M.; Voss, J.; Mao, W. L.; Karunadasa, H. L.; CCDC 1446529: Experimental Crystal Structure Determination **2016**, DOI: 10.5512/ccdc/csd/cclkk711.

(28) Wang, J.; Motaharifar, E.; Murthy, L. N. S.; Higgins, M.; Barrera, D.; Daunis, T. B.; Zheng, Y.; Malko, A. V.; Ely, F.; Quevedo-Lopez, M.; Lee, M.; Hsu, J. W. P. Revealing Lattice and Photocarrier Dynamics of High-Quality $MAPbBr_3$ Single Crystals by Far Infrared Reflection and Surface Photovoltage Spectroscopy. *J. Appl. Phys.* **2019**, 125, 025706.

(29) Kawachi, S.; Atsumi, M.; Saito, N.; Ohashi, N.; Murakami, Y.; Yamaura, J. Structural and Thermal Properties in Formamidinium and Cs-Mixed Lead Halides. *J. Phys. Chem. Lett.* **2019**, 10, 6967-6972.

(30) Poglitsch, A.; Weber, D. Dynamic Disorder in Methylammoniumtrihalogenoplumbates (II) Observed by Millimeter-Wave Spectroscopy. *J. Chem. Phys.* **1987**, 87, 6373-6378.

(31) Swainson, I. P.; Hammond, R. P.; Soulliére, C.; Knop, O.; Massa, W. Phase Transitions in the Perovskite Methylammonium Lead Bromide, $CH_3ND_3PbBr_3$. *J. Solid State Chem.* **2003**, 176, 97-104.

(32) Swainson, I. P.; Tucker, M. G.; Wilson, D. J.; Winkler, B.; Milman, V. Pressure Response of an Organic-Inorganic perovskite: Methylammonium Lead Bromide. *Chem. Mater.* **2007**, 19, 2401- 2405.

(33) Khanal, R.; Ayers, N.; Banerjee, S.; Choudhury, S. Atomic Structure and Electronic Properties of Lead and Tin Based Hybrid Halide Perovskite Surface for Photovoltaic Applications. *AIP Advances* **2019**, 9, 085123.

(34) Zhang, R.; Cai, W.; Bi, T; Niloofar, Z.; Terpstra, T.; Zhang, C.; Verdeny, Z. V.; Zurek, E.; Deemyad, S. Effects of Nonhydrostatic Stress on Structural and Optoelectronic Properties of Methylammonium Lead Bromide Perovskite. *J. Phys. Chem. Lett.* **2017**, 8, 3457-3465.

(35) Shannon, R. D. Revised Effective Ionic Radii and Systematic Studies of Interatomic Distances in Halides and Chalcogenides. *Acta. Crys.* **1976**, A32, 751-767.

(36) Walsh, A.; Sokol, A. A.; Catlow, C. R. A. Free Energy of Defect Formation: Thermodynamics of Anion Frenkel Pairs in Indium Oxide. *Phys. Rev. B* **2011**, 83, 224105.

(37) Ulatowski, A. M.; Wright, A. D.; Wenger, B.; Buizza, L. R. V.; Motti, S. G.; Eggimann, H. J.; Savill, K. J.; Borchet, J.; Snaith, H., J.; Johnston, M. B.; Herz, L. M. Charge-Carrier Trapping Dynamics in Bismuth-Doped Thin Films of $MAPbBr_3$ Perovskite. *J. Phys. Chem. Lett.* **2020**, 11, 3681-3688.

Chapter 4 Evaluating the Effectiveness of Virtual STEM Outreach in Improving Student Attitudes Towards Science and Understanding of the Relationship Between Energy and the Environment

4.1. Overview

We study the impact of a virtual outreach activity on fifth-grade students' attitudes towards science and understanding of solar energy using pre/post-activity surveys. We compare the changes in student attitudes towards science to post-activity teacher surveys to determine the accuracy of teacher assessments. We find no change in student attitudes between surveys, however students report more positive attitudes towards the outreach activity then for science and engineering activities. Student knowledge of the relationship between the environment and energy improves after participating in the outreach activity with quantifiable differences in student understanding of renewable and non-renewable energy. We find that teacher surveys overestimated the changes in students' attitudes towards science. Overall, we determine that virtual outreach can be effective at helping students learn about the relationship between energy and the environment and has the potential to improve student views on science and engineering activities.

4.2 Introduction

Rapid advances in science and inclusion of technology into society has resulted in the increased desirability of science, technology, engineering, and math (STEM) backgrounds for the incoming workforce. According to the National Science Foundation, science and engineering jobs now make up 5% of all jobs in the United States (The State of U.S. Science and Engineering 2020) and the U.S. Bureau of Labor Statistics report 16 of the 20 fastest growing occupations fall into STEM related fields (U.S. Bureau of Labor Statistics, Occupational Outlook Handbook, Fastest Growing Occupations, 2019-2029).[1,2] However, according to a 2014 National Center for Education Statistics (NCES) report, only 28% of bachelor degree and 20% of associate degree students chose to pursue a STEM degree. In addition, STEM degrees have high attrition rates with the same study reporting a 48% and 69% attrition rate for bachelor degree and associate degree students, respectively.[3] The low percentage of students pursuing STEM degrees coupled with high attrition rates has sparked concerns of an upcoming "STEM crisis" resulting in increased demand for interventions to encourage students to pursue STEM degrees and careers.[4,5]

A recent study attributed the intent to major in STEM to three factors – (1) 12th grade math achievement, (2) exposure to math and science in high school courses, and (3) math self-efficacy beliefs.[6] Exposure to math and science courses in high school can be attributed to previously developed attitudes towards science and self-efficacy beliefs.[7] In a study looking at the motivations for taking elective science courses in secondary school, Cleaves found that lack of confidence in students' ability to do well in science could be a power factor in their choosing not to take additional science classes.[8] This observation is supported by many additional studies which establish that positive attitudes towards a science leads to increased engagement and desire to pursue science based classes and careers.[6,8–24]

However, studies by Yager and Yager found that attitudes towards science decline as students' progress through primary and secondary education. By comparing responses from third, seventh, and eleventh grade students, they found that student attitudes towards science decreased over time with 60% of third grade students, 40% of students in seventh grade, and 25% of students in eleventh grade describing science class as "fun". A similar trend was seen when asking students about self-efficacy beliefs with 56% of third grade students, 38% of seventh graders, and only 28% of eleventh graders reporting positive self-efficacy views towards science.[25] More recent studies support these observations showing decreases in positive attitudes towards science during secondary education.[8,26–29] The decline in positive attitudes and self-efficacy beliefs has been attributed to many factors including the increasing complexity of subject material and shift in teaching methods from activity-based learning towards a traditional lecture-based class.[25–28]

STEM outreach activities serve as one method to address declining attitudes towards science by providing students with an opportunity to engage with science and scientists.[15] Types of STEM outreach activities vary widely in duration, design, teaching style, and objectives. Some popular methods of STEM outreach include workshops, summer camps, classroom visits, and mentorship programs.[9,19] Several studies show that these STEM outreach activities improve student attitudes and motivation towards STEM.[15,17–20,22,23,30] However, as Vennix and co-workers show, the impact of these activities on attitude and motivation depends on the characteristics of the activity.[19] For example, activities that showed a personal connection between students and the science topic being explored resulted in increased autonomous motivation among students.[19] While many studies have investigated the benefits from STEM programs, these studies show the results of in-person interactions and the impact of virtual based STEM activities remains unknown.

The shift to remote learning during the COVID-19 pandemic created a demand for virtual outreach activities and for a better understanding of virtual learning environments. School shut-downs resulted in K-12 instructors struggling to rapidly adapt their curriculum to remote learning environments, often resulting in a reduction in the amount of curriculum taught and the number of student assessments.[31–33] While the full impact of COVID-19 shutdowns on student learning can not be determined yet, Middleton predicts that inequities such as the opportunity gap will likely increase as a result of the loss in student instructional time.[33] The school closures and limited capacity operations that have persisted through academic year 2020-2021 resulted in a loss of opportunities for in-person STEM outreach activities. Designing a virtual outreach activity provides and opportunity to continue to engage with K-12 students and promote interest and positive attitudes towards STEM.

In this study we investigate the impact of a virtual science activity to determine the extent of the impact this has on student knowledge of content and attitudes towards science. Specifically, we investigate two research questions:

> *Research Question 1 (RQ1): To what extent does a virtual outreach event impact student understanding that energy and fuels are derived from natural resources and their use impacts the environment?*
>
> *Research Question 2 (RQ2): To what extent do teacher evaluations accurately reflect the impact of an outreach activity on student's attitudes towards STEM and STEM careers?*

We use pre/post-activity surveys to measure the impact of the virtual activity and quantitative analysis methods to determine the extent of change in knowledge and attitudes. We also use post-

activity surveys with teachers to determine if teachers accurately predict the impact of the activity on student attitudes towards STEM/STEM careers.

4.3 Methods

We conducted a 45-minute virtual outreach activity simultaneously for three fifth grade classes, totaling 75 students. The virtual outreach activity included a 15-minute presentation on energy production and the relationship to the environment followed by 20-minute guided solar car design and race experiment. Finally, the last 10 minutes were left for a recap of the lessons from the experiment with an opportunity for students to ask questions. To evaluate the effectiveness of our outreach activity we conducted voluntary student surveys before and after the outreach activity. Students were able to participate in the outreach activity regardless of whether they completed the survey. Additionally, we asked the three classroom teachers to complete a post-activity survey to evaluate the outreach activity in terms of impact on student attitudes towards STEM/STEM Careers.

4.3.1 Student Surveys

We used the same questions on the pre/post-surveys activity to make a direct comparison between student knowledge and attitudes towards STEM/STEM careers before and after the outreach activity. Surveys included knowledge-based questions and Likert-scale questions to determine student attitudes towards STEM/STEM careers. Knowledge based questions were developed to align with Next Generation Science Standards (NGSS) 4-ESS-1. To understand attitudes towards science, we created questions using the "My Attitudes Towards Science (MATS)" survey as a guide.[34] The survey questions used are provided in the Supporting Information Survey Instruments.

Prior to starting the outreach activity, we explained the purpose of our surveys and provided a link to a google survey for the pre-activity assessment. A total of 39 students completed the pre-activity survey. Following the outreach activity, we reminded students who participated in the first survey to fill out the post-activity survey and provided a new google survey link for those students. In total, 27 students completed the post activity survey.

4.3.2 Teacher Surveys

We use previously developed teacher surveys, detailed in Supporting Information Survey Instruments, that have been used for the last 3 years and were developed for feedback on the outreach activities. We match four questions between the student surveys and the teacher surveys to compare how accurately teachers predict the impact on student interest in science and engineering, (2) knowledge of jobs, (3) confidence, and (4) student enjoyment of the outreach activity. All three teachers responded to the survey, however, there is a response missing on two of the questions regarding student attitudes.

4.4 Results and Discussion

4.4.1 Impact on Student Knowledge

We determine the impacts of the outreach activity on student knowledge about the relationship between energy and the environmental using three open response questions, summarized in **Table 1.**

Table 1: Open Response Questions to Evaluate Student Knowledge of Relationship Between Energy and the Environment	
Topic	Question
Environmental Impacts	What are some of the environment impacts of energy production?
Renewable Energy Sources	List methods of energy production that use renewable resources.
Non-Renewable Energy Sources	List methods of energy production that use non- renewable resources.

We use deductive thematic analysis to evaluate the student responses for each open response question as described in Supporting Information. We tabulate the number of responses in each coding category and calculate two separate comparative metrics: percentage of coded response and probability of coded response. We define percentage and probability in Eq 1 and Eq 2 respectively.

$$Percentage\ of\ Responses = \frac{\#\ of\ responses}{total\ \#\ of\ surveys}\ x\ 100 \quad (1)$$

$$Probability\ of\ Responses\ = \frac{\#\ of\ surveys\ with\ response}{total\ \#\ of\ surveys} \quad (2)$$

While percentage of coded response and probability of coded response(x100) are often equivalent, we note that particularly for the environmental impacts question we see more than one response per main coded categories resulting in discrepancies between the metrics. We consider the probability of a coded response appearing on a survey to be a more accurate reflection of change in knowledge compared to the percentage of responses. Therefore, when running statistical analysis we compare the probability of coded responses between pre/post-activity surveys to determine the impacts of participation in the outreach activity on student knowledge of the relationship between energy and the environment. While the preferred methods of statistical analysis of pre/post-surveys uses the paired T-test or Wilcoxon test to determine the change for each study member between surveys, one limitation of this study is the inability to identify which matching pre/post-activity surveys responses due to the anonymous nature of our online survey. Instead, we use the Welch's T-test with a 95% confidence interval to determine if we observe a measurable change in the mean probability for coded responses between the pre/post-activity surveys. This limits our ability to compare the impact of our intervention within individual respondents but allows us to determine if there is an overall effect between the groups.

For environmental impacts of energy production, we code the student responses into four main categories: (1) general responses, (2) specific responses, (3) uncertain responses, and (4) miscellaneous responses. **Figure 4.1** shows the percentage of responses for the four main categories on both surveys.

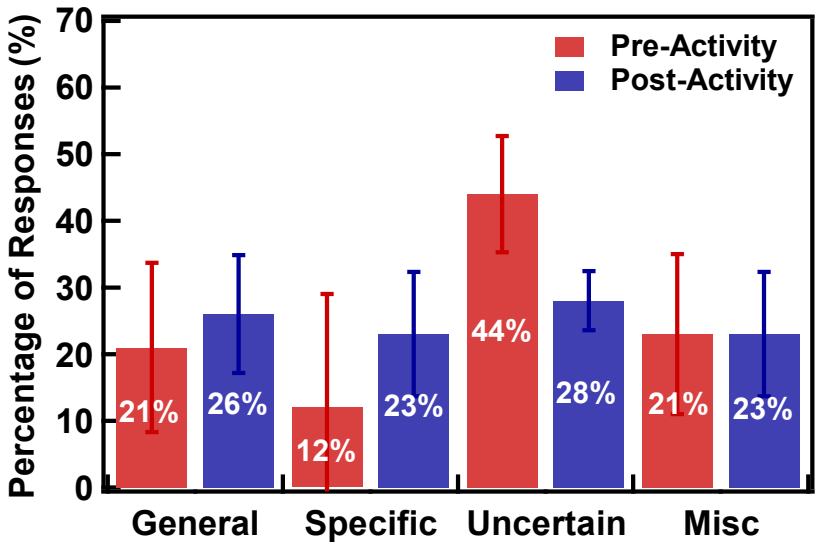

Figure 4.1: Percentage of student responses for environment impacts of energy production classified by general, specific, uncertain, and miscellaneous responses. Results for pre-activity survey (red, n=38) and post-activity survey (blue, n=27).

We observe the following qualitative trends between the pre/post-activity surveys: (1) an increase in the percentage of both general and specific responses (2) a decrease in the percentage of uncertain responses. Table 2 shows a summary of student responses for the environmental impacts of energy production coded into four main categories and the responses within each category. As shown in Table 2, we see the largest increase in the number of specific responses with an additional 5 students identifying "pollution" as an environmental impact of energy production on the post-survey. Conversely, we show that the number of "I don't know" responses decrease from 18 on the pre-activity survey to 9 on the post-activity survey. Due to the fewer number of responses on the post-activity survey, we use the change in probabilities to determine if we see a change in the mean probability between responses in the pre/post-activity surveys.

Table 2: Summary of Coded Responses for "What are some of the environmental impacts of energy production?"

Level 1 Coding	Level 2 Coding	Pre-Activity Survey # of Responses	Post-Activity Survey # of Responses
General Responses	Global Warming	3	9
	Climate Change	3	1
	Harmful to the Environment	3	0
	Total General Responses	**9**	**10**
Specific Responses	Pollution	1	6
	CO_2 Emission	2	1
	Affects Animals	1	1
	Water Pollution	1	1
	Total Specific Responses	**5**	**9**
Uncertain Responses	I don't know	18	9
	No Response	1	3
	Total Uncertain Responses	**19**	**11**
Miscellaneous Response	**Miscellaneous Response**	**10**	**9**

Table 3 shows a summary of the probability for coded responses on both surveys along with a p-value for each category as determined using the Welch T-Test. We observe an increase in the probability of general responses and specific responds along with a decrease in uncertain responses for the post-activity surveys. We use a p-value < .05 as a threshold for rejecting the null hypothesis of equivalent ranked means between the pre/post-activity surveys. We report p-values higher

Table 3: Probability of Coded Response In Pre/Post-Activity Surveys and P-value as determined using Welch T-Test

	Probability		P-value
	Pre-Activity Survey	Post-Activity Survey	
General Responses	0.24	0.33	.307
Specific Responses	0.13	0.22	.164
Uncertain Responses	0.50	0.41	.468
Miscellaneous Responses	0.21	0.22	.710

than .05 for all categories indicating that while we observe qualitative changes in the probability, the ranked means are equivalent over the 95% confidence interval.

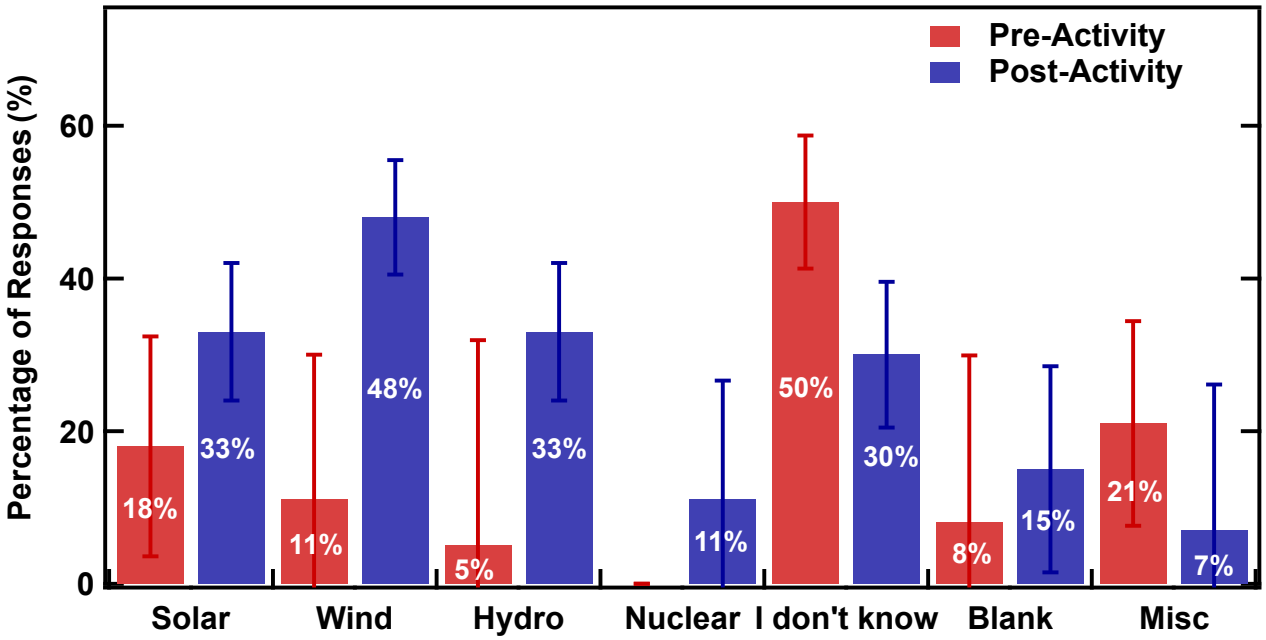

Figure 4.2: Percentage of student responses for renewable energy sources from pre-activity survey (red, n=38) and post-activity survey (blue, n=27).

Next, we compare the change in student responses for renewable energy sources between pre/post-activity surveys. **Figure 4.2** shows the percentage of pre/post-activity surveys corresponding to each category of responses. We observe an increase in the percentage of responses including solar, wind, hydropower, and nuclear power in the post-activity survey. Additionally, the percentage of "I don't know" and miscellaneous responses decreases in the post-activity survey. Table 4 shows the probability of each response for renewable energy sources on both surveys and the corresponding p-value. We report p-values below .05 for wind power, hydropower, and nuclear power indicating a higher ranked mean probability for these three responses based on a 95% confidence interval. We interpret this as an improvement in student knowledge of renewable resources.

Table 4: Probability of Renewable Energy Sources Coded Response In Pre/Post-Activity Surveys and P-value as determined using Welch T-Test

	Probability		P-value
	Pre-Activity Survey	Post-Activity Survey	
Solar Power	0.18	0.33	.190
Wind Power	0.11	0.48	.001
Hydropower	0.05	0.33	.008
Nuclear Power	0.00	0.11	.036
I don't know	0.50	0.30	.104
Blank	0.08	0.15	.383
Miscellaneous	0.21	0.07	.137

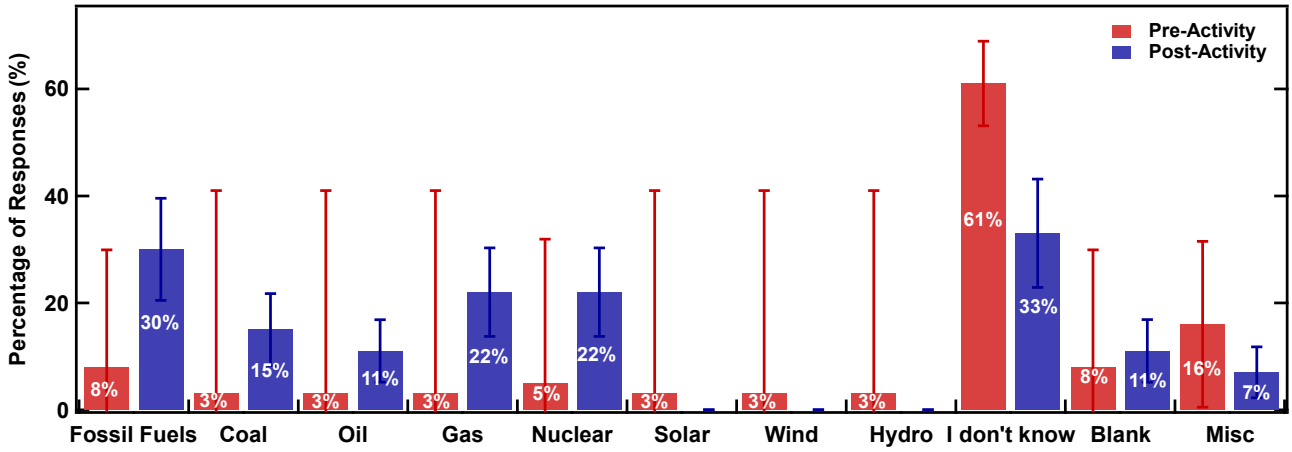

Figure 4.3: Percentage of student responses for non-renewable energy sources from pre-activity survey (red, n=38) and post-activity survey (blue, n=27).

Additionally, we investigate the change in student response for non-renewable energy methods. **Figure 4.3** shows the percentage for each response in the pre/post-activity surveys. We observe trends similar to the responses for renewable energy sources with a decrease in the percentage of "I don't know" and miscellaneous response on the post-activity survey. We also observe an increase in the percentage of fossil fuel, coal, oil, gas, and nuclear power responses. We note that nuclear power appears as a response in both renewable energy sources and non-renewable energy sources. We do not interpret this as a correct or incorrect response for either survey. Table 5 shows the probability for each response and the associate p-value. We report an increase in the mean probability on the post-activity survey for the fossil fuels and gas response based on a 95% confidence interval. The mean probability of an "I don't know" response decreases for the post-activity survey.

Table 5: Probability of Non-Renewable Energy Sources Coded Response In Pre/Post-Activity Surveys and P-value as determined using Welch T-Test

	Probability		P-value
	Pre-Activity Survey	Post-Activity Survey	
Fossil Fuels	0.08	0.30	.036
Coal	0.03	0.15	.111
Oil	0.03	0.11	.214
Gas	0.03	0.22	.029
Nuclear Power	0.05	0.22	.066
Solar Power	0.03	0.00	.324
Wind Power	0.03	0.00	.324
Hydropower	0.03	0.00	.324
I don't know	0.61	0.33	.030
Blank	0.08	0.11	.674
Miscellaneous	0.16	0.07	.292

In addition to the asking about the relationship between energy and the environment, we use multiple choice questions to evaluate whether the students know the relationship between the energy sources and the amount of CO_2 emission produced. Here we use two similarly structured multiple choice questions to ask students to identify the sources of energy that produce the most and least amount of CO_2 emission. Additionally, we ask the students to identify the challenges for using renewable energy sources. The amount of CO_2 emission for different energy sources and information about the challenges in renewable energy sources was presented to the students in the first part of the activity. We use the chi-square goodness of fit test to determine if the student responses to these questions deviated from randomness.

Table 6: Summary of Chi-Square Statistics for Multiple Choice Questions											
		Pre-Activity					Post-Activity				
	Response	Observed N	Expected N	Residual	Chi-Square	P-value	Observed N	Expected N	Residual	Chi-Square	P-value
Most CO_2 Emission	Fossil Fuels	5	8.8	-3.7			11	6.5	4.5		
	Nuclear	7	8.8	-1.7			8	6.5	1.5		
	Solar	10	8.8	1.3			4	6.5	-2.5		
	Wind	13	8.8	4.3	4.200	.241	3	6.5	-3.5	6.308	.098
Least CO_2 Emission	Fossil Fuels	5	8.8	-3.7			4	6.5	-2.5		
	Nuclear	7	8.8	-1.7			4	6.5	-2.5		
	Solar	13	8.8	4.3			12	6.5	5.5		
	Wind	10	8.8	1.3	4.200	.241	6	6.5	-0.5	6.615	.085
Renewable Energy Challenges	Amount of sunlight/wind changes	6	7.0	-1.0			6	5.2	0.8		
	Storage	9	7.0	2.0			3	5.2	-2.2		
	Transportation	5	7.0	-2.0			5	5.2	-0.2		
	All	14	7.0	7.0			11	5.2	5.8		
	None	1	7.0	-6.0	13.429	.009	1	5.2	-4.2	10.923	.027

Table 6 shows a summary of the chi-square goodness of fit test statistics for each multiple-choice question. We report no significant difference between the random responses and the student responses submitted for the questions asking students to identify the source of energy with the most carbon emission and the least amount of carbon emission. However, we find students on both pre/post-activity surveys more frequently selected the correct response of "All of the above" (14 pre, 11 post) over other potential answers for challenges for renewable energy. A chi-square goodness of fit test determined this response to be significantly more frequent than expected for random response as determined using a 95% confidence interval. To determine if there was a difference between the pre/post-activities survey was ran a Welch's t-test as reported in supporting information Table S14, however we find no statistical difference in the mean probability of student responses. We interpret the responses for the multiple-choice questions to indicate that students did not understand the relationship between quantity of CO_2 emission and energy sources. Additionally, we see no change in student understand of the challenges for renewable energy sources between pre/post-activity surveys.

4.4.2 Impact on Student Attitudes Towards STEM/STEM Careers

We evaluate the impacts of the outreach activity on student attitudes towards STEM/STEM careers using the statements shown in Table 7. The post-activity survey included one extra statement aimed at determining the student attitudes towards the outreach activity. **Figure 4.4** shows the comparison in student responses for each statement on both surveys. Overall, the student attitudes remain largely consistent between pre/post-activity surveys. We find the majority of students report positive attitudes towards science and engineering, knowledge of science and/or engineering careers, and confidence and enjoyment of science and engineering activities. Student attitudes towards jobs in science and engineering show the widest range and percent of each response.

Table 7: Comparison of Survey Attitudes Towards STEM/STEM Careers Questions between Student and Teacher Surveys		
	Student Survey	Teacher Survey
Interest in Science and Engineering	I am interested in science and engineering.	My student's interest in science and engineering increased.
Science and Engineering Jobs	I would like a job in science and engineering.	N/A
Knowledge of Jobs in Science and Engineering	I know about jobs in science and engineering.	My students increased awareness of STEM careers and academic pathways to those careers.
Confidence in Science and Engineering	I do well with science and engineering activities.	My students gained confidence in their ability to succeed in science and engineering.
Enjoyment of Activity	I enjoyed this activity.	My students had fun and left with a good impression of the experience.

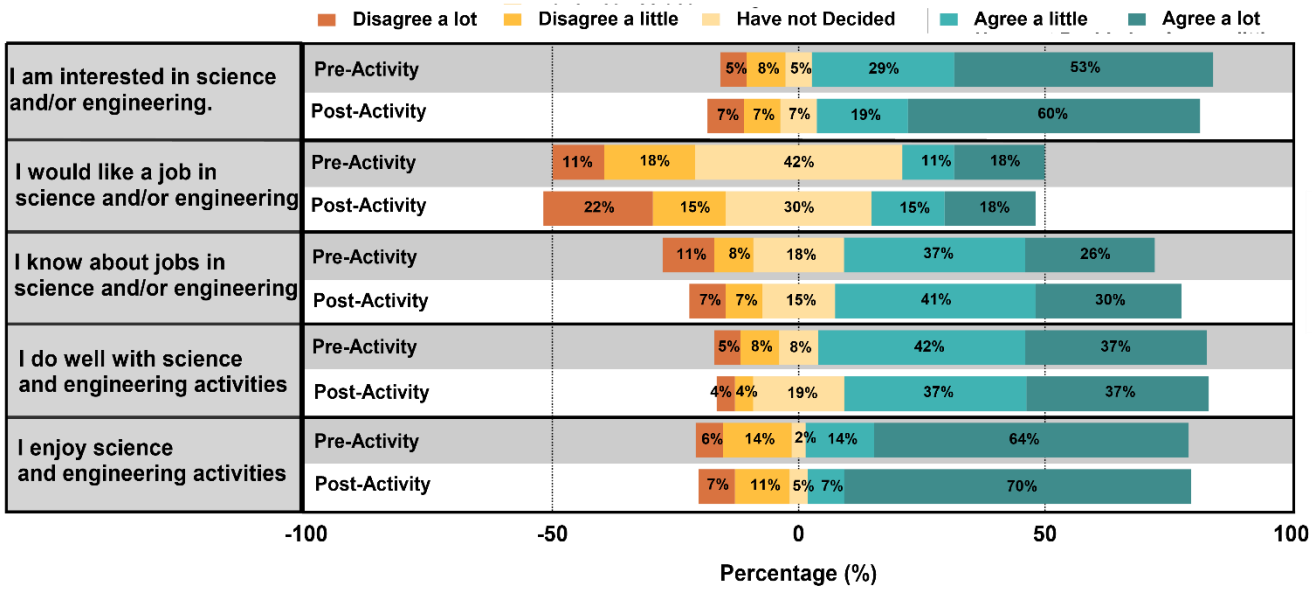

Figure 4.4: Responses to Likert Survey on Student Attitudes towards STEM/STEM Careers

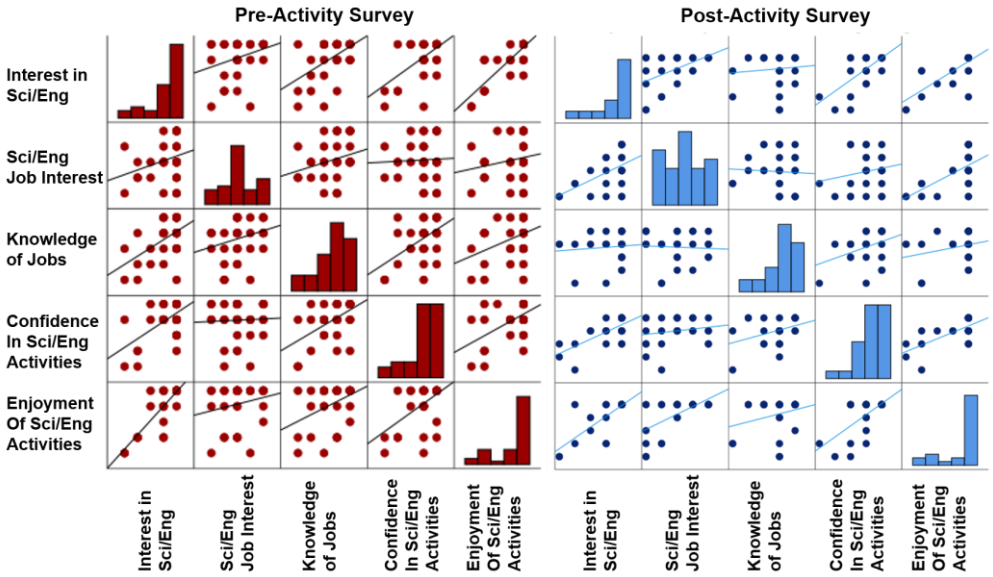

Figure 4.5: Correlation matrix plots for pre-activity (red) and post-activity (blue) survey responses. We see strong positive correlations between interest, confidences, and enjoyment on both pre/post surveys.

We correlate the student responses between these questions on both surveys using Pearson Correlation Test. The graphic representation for these correlations is shown in **Figure 4.5**. Table 8 shows the Pearson Correlation values between pre-activity survey categories with moderate and strong correlations. In the pre-activity surveys we find three strong positive correlations: (1) interest in science and engineering and confidence in ability to do science and engineering activities $r(36)=.575$, $p < .001$ and (2) interest in science and engineering and enjoyment of science and engineering activities $r(36)=.620$, $p<.001$, and (3) confidence in ability to do science and engineering activities and enjoyment of science and engineering activities $r(36)=.526$,$p=.001$.

Table 8: Pre-Activity Survey Response Correlations

Category 1	Category 2	Degree of Correlation	*r*	p-value
Interest	Knowledge of Jobs	Moderate Positive	.498	.001
Interest	Confidence	Strong Positive	.575	< .001
Interest	Enjoyment	Strong Positive	.843	< .001
Knowledge of Jobs	Confidence	Moderate Positive	.486	.002
Knowledge of Jobs	Enjoyment	Moderate Positive	.391	.018
Confidence	Enjoyment	Strong Positive	.526	.001

Table 9 show strong positive correlations between four different pairs of questions in the post activity surveys: (1) interest in science and engineering and confidence in ability to do science and engineering activities $r(25)=.688$, $p < .001$, (2)) interest in science and engineering and enjoyment of science and engineering activities $r(25)=.786$, $p < .001$, (3) interest in science and engineering jobs and enjoyment of science and engineering activities $r(25)=.606$, p .001, and (4) confidence in ability to do science and engineering activities $r(25)=.688$, $p < .001$ and enjoyment of science and engineering activities $r(25)=.650$, $p < .001$. These correlations support that views that student interest, self-efficacy views, and enjoyment impact their desire to pursue jobs in science and engineering.

Table 9: Post-Activity Survey Response Correlations

Category 1	Category 2	Degree of Correlation	*r*	p-value
Interest	Sci/Eng Jobs	Moderate Positive	.533	.004
Interest	Confidence	Strong Positive	.688	< .001
Interest	Enjoyment	Strong Positive	.786	< .001
Sci/Eng Jobs	Enjoyment	Strong Positive	.606	.001
Confidence	Enjoyment	Strong Positive	.650	< .001

We investigate the small difference in the student responses between the pre/post-activity surveys and investigate the significance of three observations from the survey comparison: (1) small decrease in interest in science and/or engineering, (2) small decrease in interest in science and/or engineering jobs, and (3) small increase reported knowledge of science and/or engineering jobs. To determine if these changes reflect changes in student opinions or the shifts represents artifacts due the decrease in survey respondents between pre/post surveys we use the Mann-Whitney U test to determine if we can reject the null hypothesis that the mean ranks of two surveys are equal.

Table 10: Mann Whitney U Scores for Pre/Post-Activity Surveys		
Question	Mann-Whitney U	p-value
I am interested in science and/or engineering.	494.500	.785
I would like a job in science and/or engineering.	482.500	.674
I know about jobs in science and/or engineering.	474.000	.588
I do well with science and engineering activities.	507.000	.932
I enjoy science and engineering activities.	462.500	.696

Table 10 shows the Mann-Whitney U scores for each question along with the calculated p-value. We describe the process for validating and interpretating the results of the Mann-Whitney U test in supporting information. We find that for all questions, the Mann-Whitney U score indicates a large overlap between pre/post-activity survey responses, and we cannot reject the null hypothesis that mean ranks of the pre/post-activity surveys are equal. Therefore, we attribute the differences in survey responses observed in **Figure 4.4** to the decrease in the number of people who took the post-activity survey and conclude that we do not see changes in student perceptions towards STEM/STEM careers with the outreach activity.

However, when we compare the post-activity student responses to "I enjoy science and engineering activities" and "I enjoyed this activity," we see that students respond more favorability towards the latter question. **Figure 4.6** compares the post-activity responses for the questions that showed strong correlations with "I enjoyed this activity" as determined using Pearson's Correlation test, as shown in Table 9. We use the Wilcoxon Signed Rank Test to determine if the mean rank between the questions is equivalent. We chose the Wilcoxon Signed Rank Test over the Mann-Whitney U test because the responses come from the same survey group and we know which responses correspond to individual students. The details of the assigned ranks for Wilcoxon Signed Ranks Test can be found in supporting information Table S25. We report a p-value of .082 between to "I enjoy science and engineering activities" and "I enjoyed this activity," indicating that the difference is weaker than required to satisfy the 95% confidence threshold but passes on 90% confidence interval test. We compare the post survey results between the other questions and "I enjoyed this activity," but we find no statistical difference in student responses. Overall, we interpret this result to mean that students had more favorable opinions towards the outreach activity compared their perception of science and engineering activities.

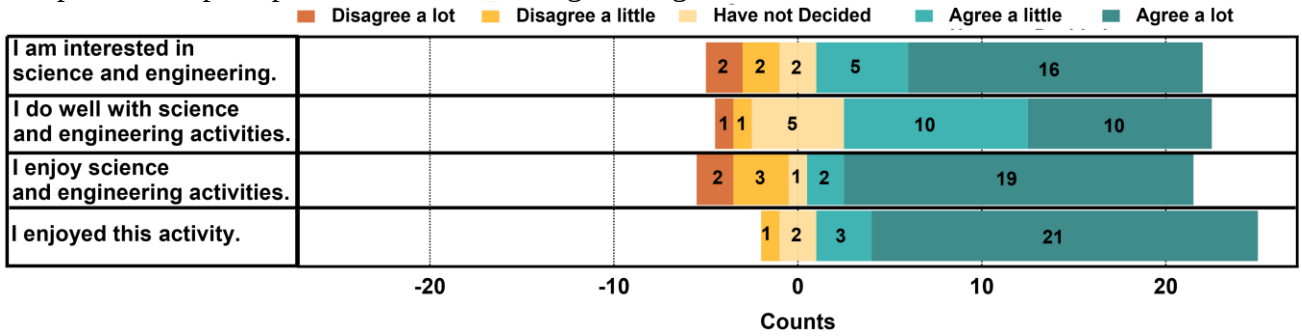

Figure 4.6: Student responses for post-activity attitudes towards STEM/STEM Careers based on a 5 point Likert-scale.

We find the discrepancy in student perspectives interesting because we designed the outreach activity to include an engineering-based activity where students are guided through testing solar car designs to determine what factors influence the speed of the solar car. Possible reasons for the difference in attitudes include, but are not limited to, difference in interpretation of

science/engineering activities, STEM anxiety associated with science and engineering. This survey did not include instruments to look at STEM anxiety or previous experiences with science and engineering activities, however, we think this could be an interest area to explore in future studies.

Teacher Evaluation of Impact on Student Attitudes Towards STEM/STEM Careers

In RQ2, we wanted to determine if teacher evaluations of student attitudes towards STEM/STEM accurately reflected the changes in student attitudes due to participation in the outreach activity. Using teacher surveys to represent student outcomes eliminates the need to collect consent forms for students and can reduce the number of approvals required. However, a direct statistical comparison of these two groups using a Welch's T-test would not produce reliable comparative information in this case due to the large difference between the number of teachers and the number of students. Instead, interpret the teachers survey responses as follows: mean/mode of 1 or 2 would indicate a decline in student attitudes, a mean/mode of 3 indicates no change in student attitudes, and a mean/mode of 4 or 5 indicates an improvement in student attitudes.

Table 7 shows the corresponding questions between the teacher surveys and the student surveys. Both the student survey and teacher survey questions were evaluated using a 5-point Likert scale. Table 11 shows a summary of statistics for all surveys. We interpret the results of the teachers surveys by looking at the mean and mode for each question and comparing those our analysis of the change between the pre-activity and post-activity student surveys. Our previous analysis of the student surveys shows no change in the student attitudes towards STEM as determined by the Mann-Whittney U test for interest in science, knowledge of job in science and engineering, and confidence in science and engineering. We would expect the teacher survey to indicate a neutral response with the mean and mode of 3 for these questions to accurately predict the lack of change in student attitudes. However, as shown in Table 11, the mean/mode for interest in science and engineering, knowledge of science and engineering jobs, and confidence in science and engineering of 3.67/4, 4.00/4, and 3.50/3,4 respectively. We evaluate the enjoyment of the activity and we conclude that the teachers overestimate the change in student attitudes for these categories.

Table 11: Comparison of Student Survey Results and Teacher Survey Results.

		Pre-Activity	Post Activity	Teacher Survey
Interest in Science and Engineering	Mean	4.16	4.15	3.67
	Mode	5	5	4
Knowledge of Jobs in Science and Engineering	Mean	3.61	3.78	4.00
	Mode	4	4	4
Confidence in Science and Engineering	Mean	3.97	4.00	3.5
	Mode	4	4,5	3,4
Enjoyment of Activity	Mean	N/A	4.63	4.33
	Mode	N/A	5	4

We are unable to determining how accurately teachers predicted whether students enjoyed the activity. Table 11 shows the mean response for students was 4.63 and the mean response for teachers was 4.33. While this indicates that teachers predicted that students enjoyed the activity, we do not know what the difference in these averages mean. We not that the mode for the teacher surveys (4) is lower than the mode for the student surveys (5). While this could suggest that the teachers slightly underestimate the impact, we note that our surveys likely contain self-selection bias which could inflate the student response to this question because people who did not enjoy the activity were less likely to complete the survey.

4.5 Conclusion

In conclusion, we determine that student knowledge of the relationship between energy and the environment improves after participating in the virtual outreach activity. While most of the measured improvements in student responses for knowledge fails to show a statistical improvement, we measure quantifiable differences in students' ability to identify certain types of renewable and non-renewable energy sources. Additionally, we determine that student attitudes towards science remains unchanged between the pre/post surveys. However, we find that teacher surveys overestimated the changes in students' attitudes towards science, predicting that student interest, confidence, and knowledge of jobs increased as a result of the activity. Overall, we prove virtual outreach has the potential to help improve student knowledge of the relationship between energy and the environment. In addition, the positive attitudes towards the activity could be helpful for improving positive attitudes towards STEM activities in the future by encouraging students to reflect on the how the activity compared to their previous concept of STEM activities.

Appendix C

Supporting information for Chapter 4 containing statistical analysis methods and detailed statistical results.

Acknowledgements

This study was reviewed for adherence to ethical standards and was determined to qualify for exempt status (Category 1). The study reviewed and approved by Edmonds School District. The researchers would like to thank the participating students and teachers. This work was supported by the Clean Energy Institute at the University of Washington.

References

(1) U. S. Bureau of Labor Statics. *Occupational Outlook Handbook: Fastest Growing Occupations*, **2021**. https://www.bls.gov/ooh/fastest-growing.htm

(2) National Science Board. *The State of U.S. Science and Engineering 2020: Science and Engineering Indicators.* **2020**. https://ncses.nsf.gov/pubs/nsb20201/preface

(3) Chen, X. *STEM Attrition: College Students' Paths Into and Out of STEM Fields (NCES 2014-001).* National Center for Education Statictics, Institute of Education Sciences, U.S. Department of Education, **2013.** https://nces.ed.gov/pubs2014/2014001rev.pdf

(4) Salzman, H.; Lowell, B. L.; *Into the Eye of the Storm: Assessing the Evidence on Science and Engineering Education, Quality, and Workforce Demand. Into the Eye of the Storm: Assessing the Evidence on Science and Engineering Education, Quality, and Workforce Demand.* Urban Institute, **2007**. https://www.urban.org/research/publication/eye-storm

(5) Xue, Y.; Larson, R. C.; STEM crisis or STEM surplus? Yes and yes," *Monthly Labor Review,* U.S. Bureau of Labor Statistics, **2015.** https://doi.org/10.21916/mlr.2015.14

(6) Wang, X. Why Students Choose STEM Majors: Motivation, High School Learning, and Postsecondary Context of Support. *American Education Research Journal* **2015**, *50* (5), 1081–1121.

(7) Bruce, B. C.; Bruce, S. P.; Conrad, R. L.; Huang, H.-J. University Science Students as Curriculum Planners, Teachers, and Role Models in Elementary School Classrooms. *Journal of Research in Science Teaching* **1997**, *34*, 69–88.

(8) Cleaves, A. The Formation of Science Choices in Secondary School. *Int J Sci Educ* **2005**, *27* (4), 471–486. https://doi.org/10.1080/0950069042000323746.

(9) Ainley, M.; Ainley, J. Student Engagement with Science in Early Adolescence: The Contribution of Enjoyment to Students' Continuing Interest in Learning about Science. *Contemp Educ Psychol* **2011**, *36* (1), 4–12. https://doi.org/10.1016/j.cedpsych.2010.08.001.

(10) Hidi, S.; Renninger, K. A. The Four-Phase Model of Interest Development. *Educ Psychol* **2006**, *41* (2), 111–127. https://doi.org/10.1207/s15326985ep4102_4.

(11) Piburn, M. D.; Baker, D. R. If I Were the Teacher. . . Qualitative Study of Attitude Toward Science. *Science Education* **1993**, *77* (4), 393–406.

(12) DeWitt, J.; Osborne, J.; Archer, L.; Dillon, J.; Willis, B.; Wong, B. Young Children's Aspirations in Science: The Unequivocal, the Uncertain and the Unthinkable. *Int J Sci Educ* **2013**, *35* (6), 1037–1063. https://doi.org/10.1080/09500693.2011.608197.

(13) Andre, T.; Whigham, M.; Hendrickson, A.; Chambers, S. Competency Beliefs, Positive Affect, and Gender Stereotypes of Elementary Students and Their Parents about Science versus Other School Subjects. *J. Res. Sci. Teach.* **1999**, 36 (6), 719-747. https://doi.org/10.1002/(SICI)1098-2736(199908)36:6<719::AID-TEA8>3.0.CO;2-R

(14) Simpkins, S. D.; Davis-Kean, P. E.; Eccles, J. S. Math and Science Motivation: A Longitudinal Examination of the Links Between Choices and Beliefs. *Developmental Psychology* **2006**, *42* (1), 70–83. https://doi.org/10.1037/0012-1649.42.1.70.

(15) Tai, R. H.; Liu, C. Q.; Maltese, A. V.; Fan, X. Planning Early for Careers in Science. *Science* **2006**, *312* (5777), 1143–1144. https://doi.org/10.1126/science.1128690.

(16) Osborne, J.; Simon, S.; Collins, S. Attitudes towards Science: A Review of the Literature and Its Implications. *Int J Sci Educ* **2003**, *25* (9), 1049–1079. https://doi.org/10.1080/0950069032000032199.

(17) Laursen, S.; Liston, C.; Thiry, H.; Graf, J.; What Good Is a Scientist in the Classroom? Participant Outcomes and Program Design Features for a Short- Duration Science Outreach Intervention in K-12 Classrooms. *CBE – Life Sciences Education* **2007**, 6, 49-64. DOI: 10.1187/cbe.06 – 05– 0165

(18) Knox, K. L.; Moynihan, J. A.; Markowitz, D. G. Evaluation of Short-Term Impact of a High School Summer Science Program on Students' Perceived Knowledge and Skills'. *J. Sci. Educ. Technol.* **2003**, 12, 471-478. https://doi.org/10.1023/B:JOST.0000006306.97336.c5

(19) Vennix, J.; Brok, P. den; Taconis, R. Do Outreach Activities in Secondary STEM Education Motivate Students and Improve Their Attitudes towards STEM? *Int J Sci Educ* **2018**, *40* (11), 1–21. https://doi.org/10.1080/09500693.2018.1473659.

(20) Bell, R. L.; Blair, L. M.; Crawford, B. A.; Lederman, N. G. Just Do It? Impact of a Science Apprenticeship Program on High School Students' Understandings of the Nature of Science and Scientific Inquiry. *J Res Sci Teach* **2003**, *40* (5), 487–509. https://doi.org/10.1002/tea.10086.

(21) Beiers, R.; McRobbie, C. Learning in Interactive Science Centres. *Res Sci Educ* **1992**, *22* (1), 38–44. https://doi.org/10.1007/bf02356877.

(22) Gibson, H. L.; Chase, C. Longitudinal Impact of an Inquiry-based Science Program on Middle School Students' Attitudes toward Science. *Sci Educ* **2002**, *86* (5), 693–705. https://doi.org/10.1002/sce.10039.

(23) Luehmann, A. L. Students' Perspectives of a Science Enrichment Programme: Out-of-school Inquiry as Access. *Int J Sci Educ* **2009**, *31* (13), 1831–1855. https://doi.org/10.1080/09500690802354195.

(24) Gardner, P. L.; Attitudes to Science: A Review. *Studies in science education* **1975**, 2, 1-41. https://doi.org/10.1080/03057267508559818

(25) Yager, R. E.; Yager, S. O. Changes in Perceptions of Science for Third, Seventh, and Eleventh Grade Students. *J Res Sci Teach* **1985**, *22* (4), 347–358.

(26) George, R. Measuring Change in Students' Attitudes Toward Science Over Time: An Application of Latent Variable Growth Modeling. *J Sci Educ Technol* **2000**, *9* (3), 213–225. https://doi.org/10.1023/a:1009491500456.

(27) Barmby, P.; Kind, P. M.; Jones, K. Examining Changing Attitudes in Secondary School Science. *Int J Sci Educ* **2008**, *30* (8), 1075–1093. https://doi.org/10.1080/09500690701344966.

(28) Tobias, S. What Makes Science Hard? A Karplus Lecture. *J. Sci. Edu. Technol.* **1993**, 2 (1) 297-304**.**

(29) George, R. A Cross-domain Analysis of Change in Students' Attitudes toward Science and Attitudes about the Utility of Science. *Int J Sci Educ* **2007**, *28* (6), 571–589. https://doi.org/10.1080/09500690500338755.

(30) Anderson, D.; Lucas, K. B.; Ginns, I. S.; Dierking, L. D.; Development of Knowledge about Electricity and Magnetism during a Visit to a Science Museum and Related Post-Visit Activities. *Sci. Educ.* **2000**, 84 (5), 658-679. https://doi.org/10.1002/1098-237X(200009)84:5<658::AID-SCE6>3.0.CO;2-A

(31) Hamilton, L. S.; Grant, D.; Kaufman, J. H.; Diliberti, M. K.; Schwartz, H. L.; Hunter, G. P.; Setodji, C. M.; Young, C. J. COVID-19 and the State of K–12 Schools: Results and Technical Documentation from the Spring 2020 American Educator Panels COVID-19 Surveys. *Creative Commons Attribution 4.0 International Public License* **2020**.

(32) Wyse, A. E.; Stickney, E. M.; Butz, D.; Beckler, A.; Close, C. N. The Potential Impact of COVID-19 on Student Learning and How Schools Can Respond. *Educ Meas Issues Pract* **2020**, *39* (3), 60–64. https://doi.org/10.1111/emip.12357.

(33) Middleton, K. V. The Longer-Term Impact of COVID-19 on K–12 Student Learning and Assessment. *Educ Meas Issues Pract* **2020**, *39* (3), 41–44. https://doi.org/10.1111/emip.12368.

(34) Hillman, S. J.; Zeeman, S. I.; Tilburg, C. E.; List, H. E. My Attitudes Toward Science (MATS): The Development of a Multidimensional Instrument Measuring Students' Science Attitudes. *Learn Environ Res* **2016**, *19* (2), 203–219. https://doi.org/10.1007/s10984-016-9205-x.

Appendix A

Experimental Method

PbS quantum dot synthesis:
Both the butylamine (BA) and oleic acid (OA) capped PbS quantum dots were prepared using an adapted version of the Hines and Scholes protocol.[1] In a 100 mL three-neck round bottom flask, 900 mg (4.0 mmol) of PbO, 28 g of 1-octadecene (ODE)(technical grade, 90%) and 2.4 g (8.5 mmol) of oleic acid were combined and stirred at 100 °C under vacuum for a minimum of 1 h to dissolve the lead precursor as well as degas and dry the solution. After heating, the solution changed color from yellow to clear indicating the PbO completely dissolved. The temperature of the reaction flask was lowered to 90 °C and returned to nitrogen flow while the sulfur precursor solution was prepared. In a separate three-neck round bottom flask, 8 g of ODE was degassed under vacuum for at least 30 min prior to the addition of 420 μL of hexamethyldisilathiane (HMDS). The sulfur precursor was then immediately injected into the hot lead precursor solution to form the PbS quantum dots.
Successful creation of the PbS quantum dots was evident by the change from a colorless solution to a black solution following the injection of the sulfur precursor. After the injection the heat was turned off allowing the reaction to slowly cool down to room temperature. The product was divided in half prior to being isolated from unreacted precursors via methods previously reported.[2] Following isolation and cleaning of the products, one half of the products were treated with butylamine using a solution-based ligand exchange. To exchange ligands, PbS QDs were dissolved in ~2 mL of butylamine and underwent 30 min of sonication. This process was performed twice to ensure full replacement of the native oleic acid ligands. Finally, both the BA treated PbS QDs and OA capped PbS QDs were dried under nitrogen flow and transferred into a nitrogen glove box. The QDs were dispersed in ~2 mL of anhydrous 1,2-dichlorobenzene and stored in the glove box until use.

Preparation of PTB1/PbS films:
PTB1 polymer solution (10 mg/mL concentration) was prepared in a nitrogen glove box by adding an appropriate amount of anhydrous 1,2- dichlorobenzene to PTB1 polymer (1-Material) and heating the solution to 70 °C while stirring until fully dissolved. The polymer/QD blend solution was prepared to be a 1:9 (w/w) ratio with both the polymer and the PbS solutions filtered using a 0.45 μm PTFE syringe filter prior to blending. The blend solution was heated to 70 °C and stirred for 1 h before filtering and spin coating onto ITO/PEDOT:PSS substrates.
To prepare the ITO/PEDOT:PSS substrates, ITO substrates were cleaned by sonication for 20 min in the each of following solutions: 2% Micro-90 detergent, DI water, acetone, and isopropanol. Following cleaning, the substrates were dried with nitrogen gas and plasma cleaned for 5 min immediately prior to spin coating the PEDOT:PSS layer. Approximately 100 μL of PEDOT:PSS was deposited onto the substrate before spinning for 1 min at 3000 rpm. Immediately after spin coating, substrates were placed on a hot plate at 120 °C for 30 min to anneal the PEDOT:PSS layer.
The blend solution was then spun onto the substrates at 1000 rpm for 90 s. Ligand exchange was performed as previously described using a 10 mmol 3-mercaptopronic acid (MPA).[2] The MPA

solution was made in acetonitrile to ensure no PEDOT:PSS was dissolved during the ligand exchange.

STEM imaging and reconstruction:
The films were exposed to DI water to dissolve the PEDOT:PSS layer and release it from the substrate, and were then collected from the surface of the water on a TEM grid. All STEM images used for the reconstructions were taken with a JEOL 2100F at 200 kV. The beam convergence semi-angle was 17.1 mrad and the inner detection semiangle was 70 mrad. Tilt series were obtained using dynamic focus via a tomography plugin for DigitalMicrograph (Gatan). Images were taken using a Saxton interval scheme from a minimum range of +65 to −65° and a maximum range of ±70°. The electron dose for each image was ∼7 electrons per square Angstrom. Image stack alignment was performed manually using IMOD,[3] and 3D reconstructions were created using the ASTRA Tomography Toolbox. The voxel size of the reconstructions is 0.35 nm.[4] Final volumes were visualized using IMOD.

AFM imaging:
AFM images were measured using a Veeco Multimode AFM in tapping mode at 1.0 Hz.

GDOES analysis:
GDOES analysis was conducted on samples using a Horiba GDProfiler-2 with a sampling time of 0.050 s at an applied power of 2.50 W and argon pressure of 4 Pa. The area of analysis was 4 mm diameter circle roughly centered on a 1 cm by 1 cm sample.

Graph analysis:
Morphology traits like connectivity to electrodes and distance of voxels to interfaces have been correlated with device performance. We utilized a fast and efficient approach to extracting morphology traits that consisted of converting the reconstructed morphology into an equivalently colored and weighted graph.[4,5] This was done by considering each voxel as a graph vertex (with the color of the vertex determined by the phase of voxel – black vertex for mixed phase and white vertex for QD). The edges of the graph are just constructed by connecting each vertex (or voxel) to its neighbors. The weight of each edge is the geometric distance between the voxel centers. The interface between the pure QD and mixed phase is identified by edges that connect vertices of different color. Vertices having an interface edge are considered as sites for exciton dissociation. The electrodes are represented as meta-vertices in the graph, which are directly connected to the top-/bottom-layer. Connectivity is calculated as the percentage of voxels that are directly connected to the respective electrode (meta-) vertex. Distance to the closest interface is calculated using Djikstra's algorithm.

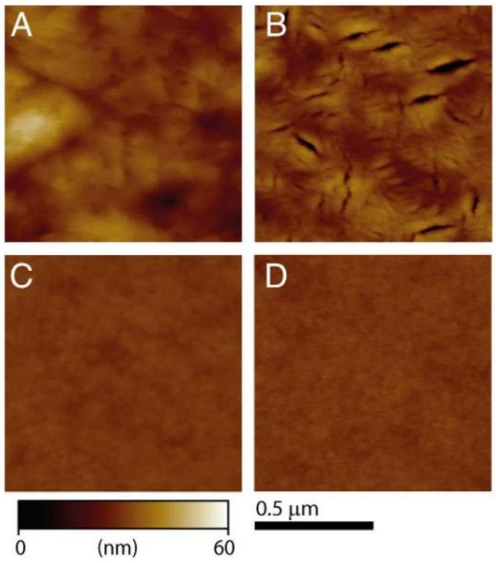

Figure S1: AFM of PbS-PTB1 blend films: (A) oleic acid as cast film, (B) MPA treated oleic acid PbS cast film, (C) butylamine as cast, (D) MPA treated butylamine PbS cast film. Inset scale bars 10 nm. Adapted with permissions from *Organic Electronics* **2018**, 54, 119-125, DOI: 10.1016.j.orgel.2017.12.018 Copyright © 2017 Elsevier B.V.

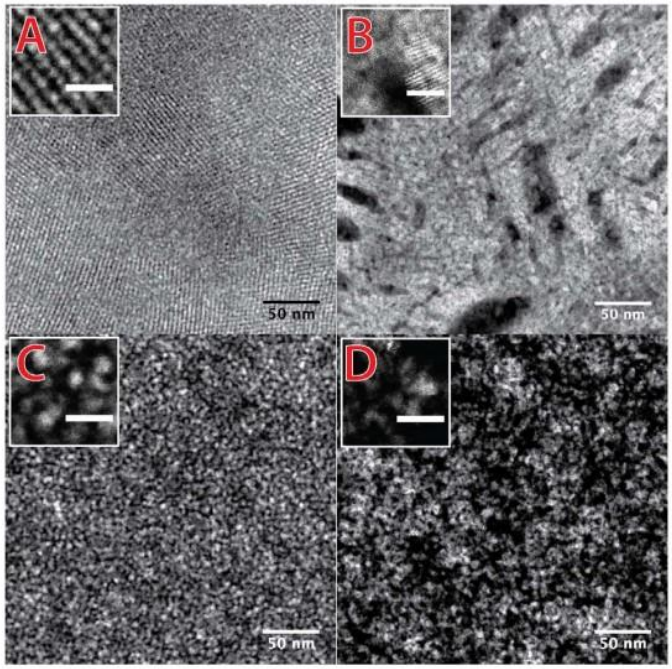

Figure S2: STEM micrographs showing the morphologies of (A) oleic acid as cast film, (B) MPA treated oleic acid PbS cast film, (C) butylamine as cast, (D) MPA treated butylamine PbS cast film. Inset scale bars 10 nm. Adapted with permissions from *Organic Electronics* **2018**, 54, 119-125, DOI: 10.1016.j.orgel.2017.12.018 Copyright © 2017 Elsevier B.V.

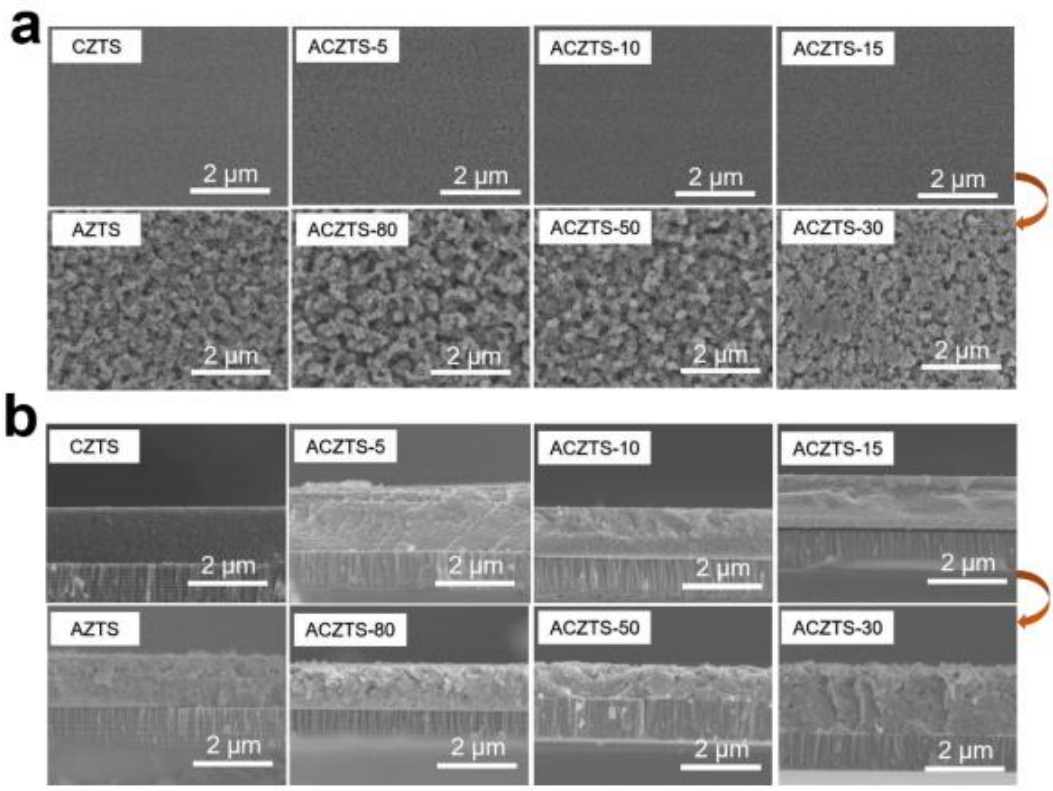

Figure S3: (a) Top and (b) cross-sectional view of SEM images with various amounts of Ag-doping. Adapted with permissions from *Adv. Funct. Mater.* **2021**, 2101927, DOI: 10.1002/adfm.202101927 Copyright © 2021 Wiley-VCH GmbH

References

(1) Hines, M. A.; Scholes, G. D. Colloidal PbS Nanocrystals with Size-Tunable Near-Infrared Emission: Observation of Post-Synthesis Self-Narrowing of the Particle Size Distribution. *Adv Mater* **2003**, *15* (21), 1844–1849. https://doi.org/10.1002/adma.200305395.

(2) Colbert, A. E.; Wu, W.; Janke, E. M.; Ma, F.; Ginger, D. S. Effects of Ligands on Charge Generation and Recombination in Hybrid Polymer/Quantum Dot Solar Cells. *J Phys Chem C* **2015**, *119* (44), 24733–24739. https://doi.org/10.1021/acs.jpcc.5b07828.

(3) Palenstijn, W. J.; Batenburg, K. J.; Sijbers, J. Performance Improvements for Iterative Electron Tomography Reconstruction Using Graphics Processing Units (GPUs). *J Struct Biol* **2011**, *176* (2), 250–253. https://doi.org/10.1016/j.jsb.2011.07.017.

(4) Wodo, O.; Tirthapura, S.; Chaudhary, S.; Ganapathysubramanian, B. A Graph-Based Formulation for Computational Characterization of Bulk Heterojunction Morphology. *Org Electron* **2012**, *13* (6), 1105–1113. https://doi.org/10.1016/j.orgel.2012.03.007.

(5) Wodo, O.; Roehling, J. D.; Moulé, A. J.; Ganapathysubramanian, B. Quantifying Organic Solar Cell Morphology: A Computational Study of Three-Dimensional Maps. *Energ Environ Sci* **2013**, *6* (10), 3060–3070. https://doi.org/10.1039/c3ee41224e.

Appendix B

Experimental Methods:

Chemicals

Methylammonium bromide (MABr, Dyesol), lead dibromide ($PbBr_2$, >98% Sigma), bismuth tribromide ($BiBr_3$, Sigma), *N*,*N*-dimethylformamide (DMF, Sigma), formic acid (≥ 95%, Sigma Aldrich), lead standard for ICP (Sigma, Tracecert, 1000 mg/L), bismuth standard for ICP (Sigma, Tracecert, 1000 mg/L). All chemicals and reagents were used as received with no further purification.

Single Crystal Growth

Solution preparation

A 1 M $MAPbBr_3$ solution is prepared by combining MABr and $PbBr_2$ in DMF and stirring until solids are completely dissolved. $MAPbBr_3$ solution should be clear and colorless once completely dissolved. Separately, we prepared a 1 M $BiBr_3$ solution in DMF which form a transparent yellow solution upon once dissolved.

Undoped crystal synthesis

For undoped crystals, we added 30μL of formic acid to 1 mL of 1 M $MAPbBr_3$. Upon addition of the formic acid to the $MAPbBr_3$ solution, small orange precipitates formed at the surface of the liquid. These precipitates were readily dissolved with gently shaking. This solution was filtered through a 0.2μ PTFE syringe filter into 4 mL vial (rinsed with ultra-pure Milli-Q water and dried for at least 1 hour in a glassware oven) and quickly capped to prevent any dust or debris that might cause nucleation. After filtering, growth solutions were placed in a 50˚C oil bath and allowed to equilibrate to temperature for 30 minutes. The temperature of the oil bath was slowly increased by 2.5˚C approximately every 30 minutes until nucleation occurred. Once bright orange crystals formed, approximately 62-68˚C for 0%, 0.1%, and 1% $BiBr_3$ solutions and 95-100 ˚C for the 10% $BiBr_3$ solution, the solution was left at the same temperature for several hours until crystal reached approximately 2-3 mm in size. The solution was decanted onto kimwipes to collect single crystals and remove extra growth solution. Crystals were store under atmospheric conditions in the dark.

Bismuth-doped crystal synthesis

For bismuth-doped crystals, we combined 0.1, 1, and 10% of 1 M $BiBr_3$ solution with 1 M $MAPbBr_3$ solution for a total volume of 1 mL. Upon addition of 30μL of formic acid, small red precipitates formed at the surface. Precipitates were redissolved through gentle agitation before filtering the solution through a 0.2μ PTFE syringe filter into a clean 4 mL scintillation vial. The solution was capped to prevent dust or other impurities and placed in a 50˚C oil bath for 30 minutes. The oil bath temperature was raised by 5˚C every half hour until nucleation occurred. Once crystals were observed, the oil bath was left at the same temperature to prevent excess nucleation. Crystals were grown to approximately 2-3 mm before they were removed from solution, dried, and stored.

Inductively Coupled Plasma - Optical Emission Spectroscopy (ICP-OES)

To prepare crystals for ICP-OES measurements, we digested samples in concentrated nitric acid and diluted to parts per billion (ppm) concentrations. We prepared a single stock solution of 50 ppm Pb and 5 ppm Bi using 1000 ppm Pb and 1000 ppm Bi ICP standard solutions (Sigma-Aldrich). We used the stock solution to prepare calibration standards ranging from 125 ppb Pb to 50 ppm Pb and 12.5 ppb Bi to 5 ppm Bi. We measured calibration standards and samples in a continuous run using Perkin Elmer 8300 ICP-OES unit with lower detection limits of 1 ppb for Pb and 1 ppb for Bi.

X-ray Diffraction:

To quantify the change in lattice spacing, we primarily fit the XRD peaks to a pseudo-Voight function to find the 2θ peak and extract the d-spacing for each crystal using Bragg's equation (Equation S1). In this equation, d_{hkl} represents the distance between parallel planes in the crystal lattice or d-spacing, n represents an integer, λ represents the wavelength of the x-ray source, and θ represents the incidence angle of the x-rays on the crystal.

$$d_{hkl} = \frac{n\lambda}{2sin\theta} \tag{S1}$$

Equation S2 shows the relationship between the d-spacing and lattice constant, a. The h, k, and l terms in this equation show the orientation of crystal lattice.

$$d_{hkl} = \frac{a}{\sqrt{h^2 + k^2 + l^2}} \tag{S2}$$

Microcalorimetry Measurements:

We measure specific heat capacity using a Dynacool Physical Property Measurement System (PPMS, Quantum Design). Equation S3 describes the heat capacity measured by this system. In this equation C_{total} represents the total heat capacity of the sample and the sample platform, K_w is the thermal conductance of the supporting wires, T_b represents the temperature of the sample holder, and $P(t)$ represents the applied power from the heater as function of time t. (Reference 1)

$$C_{total} * \frac{dT}{dt} = -K_w * (\mathrm{T} - T_b) + P(t) \tag{S3}$$

To determine heat capacities for each crystal, we conduct background measurements prior to loading the crystal. We then cool samples at a rate of approximately 10 K/min and allow the temperature to stabilize until a temperature drift of less than 1% of the temperature rise was achieved. Once stabilized at the measurement temperature, we apply a heat pulse to generate a 0.5% - 2% rise in the sample temperature. We fit the cooling decay to an exponential decay function and extract out a time constant, τ, that equals C_{total}/K. (Reference 1) We repeat measurements twice at each temperature to ensure repeatability.

Conductivity Measurement:

Conductivity measurements were performed by cleaving the crystals to expose a freshly cleaved surface. Gold contacts were sputtered to this surface in a standard four-point matchstick geometry. Current was applied through the crystal by applying a voltage triangle wave to the outer two contacts and measuring the current response. The voltage response of the inner two leads was measured with a high input impedance voltmeter, usually a Keithley 6514 with an input impedance of 200TΩ.

The linearity of the IV curves usually deviated from perfect linearity at low temperature, at which point the measurement was terminated. For higher temperatures, the IV relationship was usually ohmic enough to determine a resistance by a linear fit of the data.

Density Functional Theory:
All calculations were based on Kohn-Sham density-functional theory[2]. The Vienna Ab Initio Simulation Package (VASP)[3,4] was used where projector augmented-wave (PAW)[5,6] pseudo-potentials is implemented. The valence states of H, C, N, Pb, Bi, and Br are treated explicitly by 1 ($1s^1$), 4 ($2s^2 2p^2$), 5 ($2s^2 2p^3$), 14 ($5d^{10} 6s^2 6p^2$), and 15 ($5d^{10} 6s^2 6p^3$), and 7 14 ($4s^2 4p^5$) electrons, respectively. Structure optimization calculations were performed employing the Perdew-Burke-Ernzerhof exchange-correlation functional revised for solids (PBEsol)[7] with the plane-wave kinetic cutoff energy of 700 eV. Convergence criteria of 10^{-6} eV for total energy in unit cell and 10^{-3} eVÅ^{-1} for forces on each atom were set. $2 \times 2 \times 2$ super cell of cubic $MAPbBr_3$ (96 atoms) was employed to model charged point defects. For $1 \times 1 \times 1$ primitive cell Γ-centered *k*-point grid of $8 \times 8 \times 8$ was applied, while Γ-centered *k*-point grid of $4 \times 4 \times 4$ was used for $2 \times 2 \times 2$ supercells.

Supporting Information

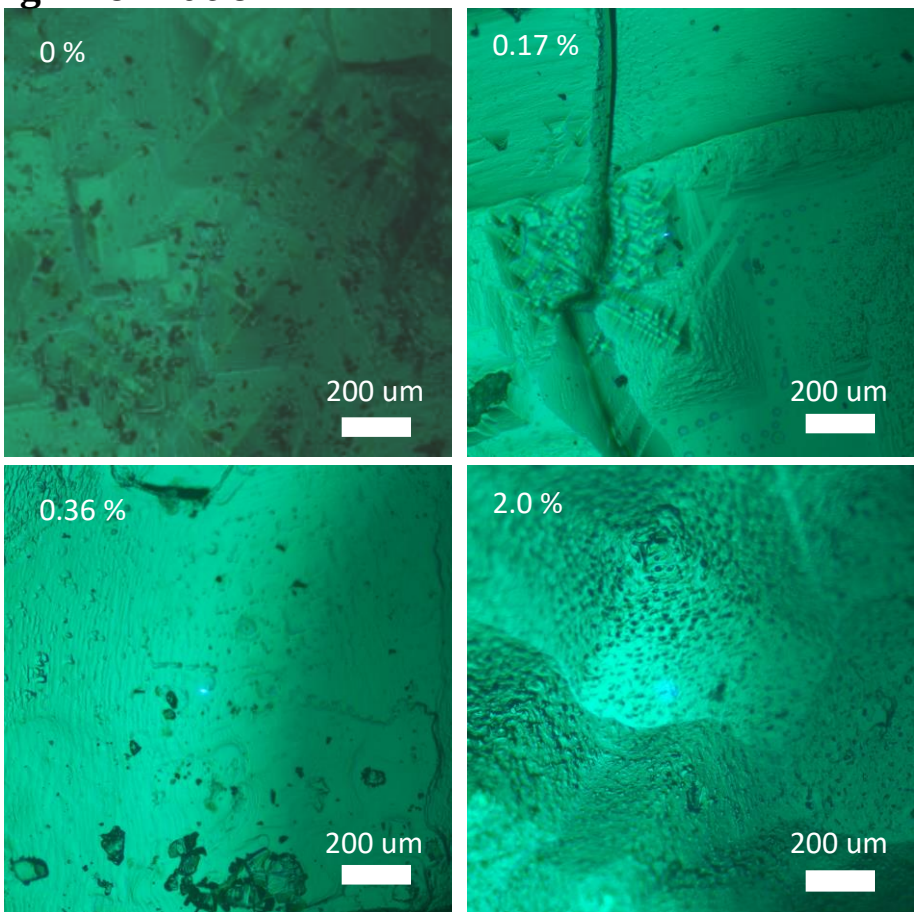

Fig. S1, Optical microscopy images for single crystals with varying levels of bismuth doping.

Table S1, Summary of reported temperature-dependent $MAPbBr_3$ Crystal Structure

Phase	Temperature (K)	Crystal System	Space Group	Lattice (pm)	Reference
α	> 236.9	Cubic	P*m3m*	*a* = 590.1	8
β	155.1 - 236.9	Tetragonal	I4/*mcm*	*a* = 832.2 *c* = 1183.2	8
λ	149.5 – 155.1	Tetragonal	P4/*mmm*	*a* = 589.4 *c* = 586.1	8
δ	> 145	Orthorhombic	*Pnma*	*a* = 794.3 *b* = 1184.9 *c* = 859.2	9

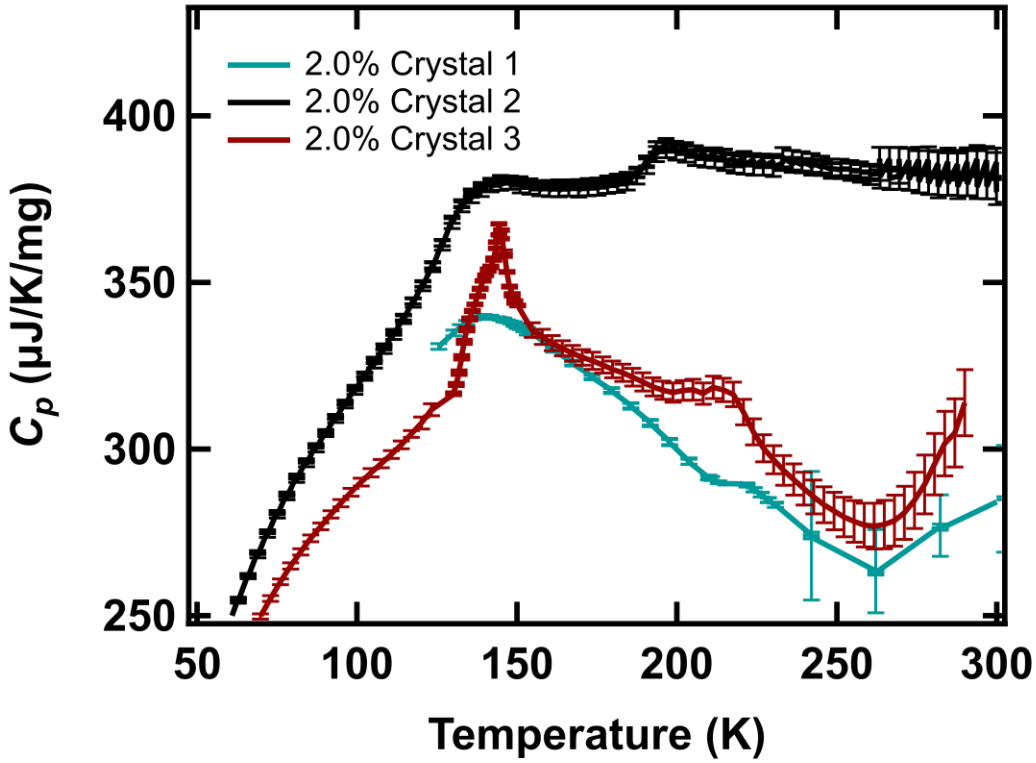

Fig. S2, Temperature-dependent specific heat capacity (C_p) measurements for different 2.0% Bi single crystals.

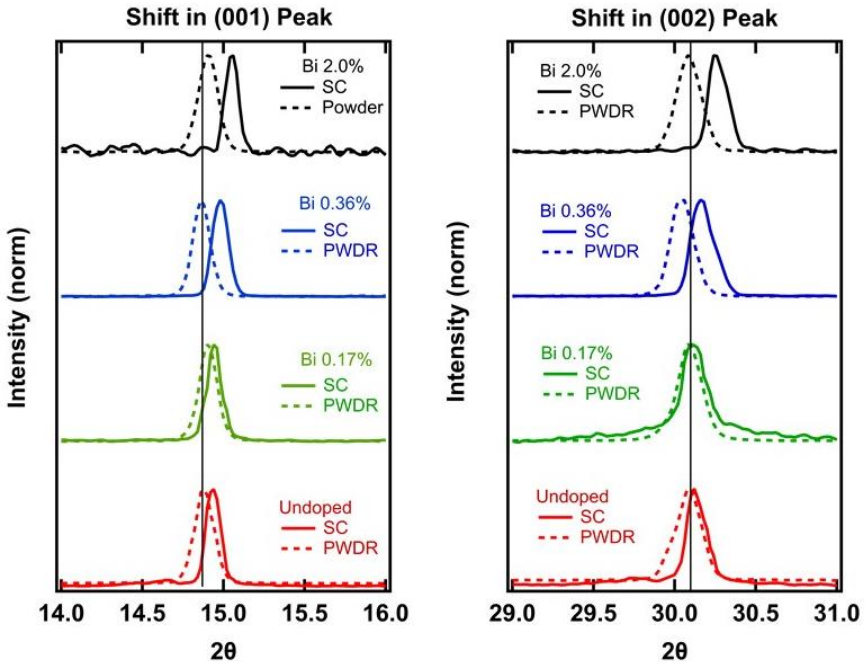

Fig. S3, Comparison XRD spectra between single crystal (solid lines) and crushed powders (dashed lines) for varying Bi-doping level.

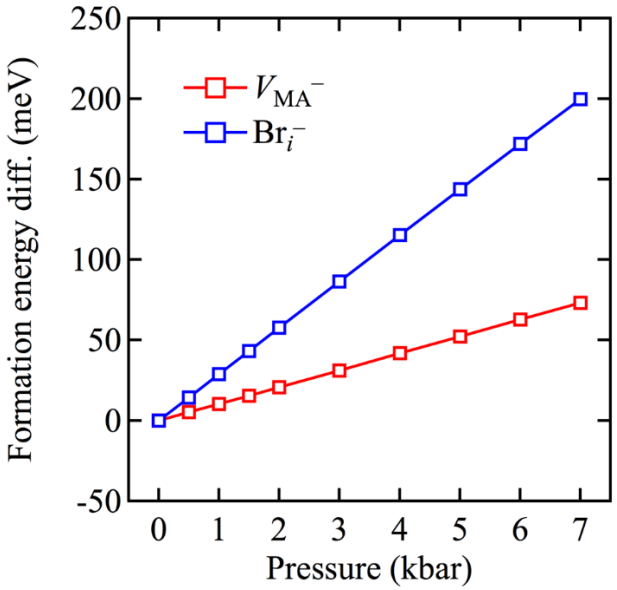

Fig. S4, DFT calculated formation energy vs. lattice pressure for negatively charged defects: MA vacancy and Bromine interstitial.

References

(1) Quantum Design. *Physical property measurement systems: heat capacity option user's manual.* https://www.mrfn.org/files/instrument/DynaCool_Manual_A0.pdf

(2) Kohn, W.; Sham, L. J. Self-Consistent Equations Including Exchange and Correlation Effects. *Phys. Rev.* **1965**, 140, A1133–A1138.

(3) Kresse, G.; Furthmüller, J. Efficient Iterative Schemes forAb InitioTotal-Energy Calculations Using a Plane-Wave Basis Set. *Phys. Rev. B* **1996**, 54, 11169–11186.

(4) Kresse, G.; Furthmüller, J. Efficiency ofAb-InitioTotal Energy Calculations for Metalsand Semiconductors Using a Plane-Wave Basis Set. *Comput. Mater. Sci.* **1996**, 6, 15–50.

(5) Kresse, G.; Joubert, D. From Ultrasoft Pseudopotentials to the Projector Augmented-Wave Method. *Phys. Rev. B* **1999**, 59, 1758–1775.

(6) Blöchl, P. E. Projector Augmented-Wave Method. *Phys. Rev. B* **1994**, 50, 17953–17979.

(7) Perdew, J. P.; Ruzsinszky, A.; Csonka, G. I.; Vydrov, O. A.; Scuseria, G. E.; Constantin, L. A.; Zhou, X.; Burke, K. Restoring the density-gradient expansion for exchange in solids and surfaces. *Phys. Rev. Lett.* **2008**, 100, 136406.

(8) Poglitsch, A.; Weber, D. Dynamic disorder in methylammoniumtrihalogenoplubates (II) observed by millimeter-wave spectroscopy. *J. Chem. Phys.* **1987**, 87 (11), 6373–6378.

(9) Swainson, I. P.; Hammond, R. P.; Soulliere, C.; Knop, O.; Massa, W. Phase transitions in the perovskite methylammonium lead bromide, $CH_3ND_3PbBr_3$. *J. Solid State Chem.,* **2003**, 176, 97–104.

Appendix C

Statistical Analysis Methods:

We note the preferred method for statistical analysis for pre/post survey design to be the paired T-test, however this requires knowledge of which surveys responses are matched. Due to the school districts preference for anonymous surveys and the limitations with issuing online surveys in an expedient manner, we are unable to match responses between surveys. Therefore, we use the mean or ranked mean between the pre-survey group and the post survey group to determine the impact of the intervention. This limitation prevents us from learning if the was a change in individual responses between pre/post survey.

Open-ended Response Questions:
We use the Welch's T-test to determine the difference in mean probability of coded responses between pre-activity and post-activity surveys. Before running Welch's T-test, we test for normality using Shaprio-Wilk test. We use p-values < .05 to reject the null hypothesis that the distributions are normal. We determine the mean probabilities to be different if p < .05 for the t-test.

Multiple Choice Questions:
For multiple choice questions we use the chi-squared goodness of fit test to determine if student responses deviated from the probability of randomly choosing an answer. We define the probability of randomly choosing a response in Eq S1 below:

$$Probabilty\ of\ Random\ Response = \frac{1}{\#\ of\ answers} \quad \text{(S1)}$$

We use a p-value < .05 to reject the null hypothesis that there is no preferential response and that the responses do not deviate significantly from randomness.

For questions that show a preferential response, we use the Welch's T-test to determine the difference in mean probability of the preferred response between pre-activity and post-activity surveys. We determine the mean probabilities to be different if p < .05 for the t-test.

Likert-scale Questions:
Due to the potential for skewed results, we first test for normality using Shaprio-Wilk test. We use p-values < .05 to reject the null hypothesis that the distributions are normal. We use the Mann-Whitney U test instead of Welch' T-test because of the parametric distribution. The Mann-Whitney U test requires that the data be skewed in similar manners. We test for a statistical difference between the variations using a Levene test with a threshold of p-value < .05 to signify a difference in the variances. A large Mann-Whitney U score indicates a larger overlap of the ranked mean between the two groups, a small score indicates a small overlap between groups, and score of 0

indicates no overlap between groups. We use a p-value < .05 to indicate a difference in the ranked means of the two groups.

Comparison Between Post-Survey Responses:
We chose the Wilcoxon Signed Rank Test over the Mann-Whitney U test to analysis how students responded between post-survey questions. The responses within the same survey group are matched and we can compare how student responses change between the questions. We use a p-value < .05 to indicate a difference in the ranked averages between the two groups.

Table S1: Shapiro-Wilk Test for Normality of "What Are Some Environmental Impacts of Energy Production?" Level 1 Coding Categories

Tests of Normality

		Kolmogorov-Smirnov[a]			Shapiro-Wilk		
Identifier		Statistic	df	Sig.	Statistic	df	Sig.
Pre-Activity Suvery	# of General Responses	.472	38	.000	.528	38	.000
	# of Specific Responses	.518	38	.000	.400	38	.000
	# of Uncertain Responses	.338	38	.000	.637	38	.000
	# of Misc Responses	.459	38	.000	.487	38	.000
Post-Activity Survey	# of General Responses	.411	27	.000	.651	27	.000
	# of Specific Responses	.466	27	.000	.539	27	.000
	# of Uncertain Responses	.385	27	.000	.626	27	.000
	# of Misc Responses	.433	27	.000	.450	27	.000

a. Lilliefors Significance Correction

Table S2: Independent Samples T-test Results for "What Are Some Environmental Impacts of Energy Production?" Level 1 Coding Categories

Independent Samples Test

		Levene's Test for Equality of Variances		t-test for Equality of Means						
									95% Confidence Interval of the Difference	
		F	Sig.	t	df	Sig. (2-tailed)	Mean Difference	Std. Error Difference	Lower	Upper
General Repsonse	Equal variances assumed	2.663	.108	-.848	63	.400	-.096	.114	-.324	.131
	Equal variances not assumed			-.833	52.226	.409	-.096	.116	-.329	.136
Specfic Response	Equal variances assumed	3.593	.063	-.952	63	.345	-.091	.095	-.281	.100
	Equal variances not assumed			-.919	48.425	.363	-.091	.099	-.289	.108
Uncertain Reponse	Equal variances assumed	1.308	.257	.730	63	.468	.093	.127	-.161	.346
	Equal variances not assumed			.731	56.560	.468	.093	.127	-.161	.346
Misc Response	Equal variances assumed	.049	.825	-.111	63	.912	-.012	.105	-.222	.198
	Equal variances not assumed			-.111	55.274	.912	-.012	.106	-.223	.200

*Welch's T-test results are equal variances not assumed.

Table S3: Shapiro-Wilk Test for Normality for “List Methods of Energy Production That Use Renewable Resources”

Tests of Normality

		Kolmogorov-Smirnov[a]			Shapiro-Wilk		
Identifier		Statistic	df	Sig.	Statistic	df	Sig.
Pre-Activity Suvery	# of Solar Responses	.496	38	.000	.473	38	.000
	# of Wind Responses	.527	38	.000	.355	38	.000
	# of Hydro Responses	.539	38	.000	.237	38	.000
	# of Nuclear Responses	.	38	.	.	38	.
	# of I don't know Responses	.338	38	.000	.637	38	.000
	# of No Responses	.535	38	.000	.302	38	.000
	# of Misc Responses	.484	38	.000	.502	38	.000
Post-Activity Survey	# of Solar Responses	.423	27	.000	.597	27	.000
	# of Wind Responses	.346	27	.000	.638	27	.000
	# of Hydro Responses	.423	27	.000	.597	27	.000
	# of Nuclear Responses	.525	27	.000	.368	27	.000
	# of I don't know Responses	.442	27	.000	.576	27	.000
	# of No Responses	.511	27	.000	.427	27	.000
	# of Misc Responses	.535	27	.000	.294	27	.000

a. Lilliefors Significance Correction

Table S4: Independent Samples T-test Results for “List Methods of Energy Production That Use Renewable Resources”

Independent Samples Test

		Levene's Test for Equality of Variances		t-test for Equality of Means						
									95% Confidence Interval of the Difference	
		F	Sig.	t	df	Sig. (2-tailed)	Mean Difference	Std. Error Difference	Lower	Upper
# of Solar Responses	Equal variances assumed	6.992	.010	-1.374	63	.174	-.149	.109	-.366	.068
	Equal variances not assumed			-1.328	48.833	.190	-.149	.112	-.375	.077
# of Wind Responses	Equal variances assumed	42.926	.000	-3.693	63	.000	-.376	.102	-.580	-.173
	Equal variances not assumed			-3.413	39.654	.001	-.376	.110	-.599	-.153
# of Hydro Responses	Equal variances assumed	54.120	.000	-3.150	63	.002	-.281	.089	-.459	-.103
	Equal variances not assumed			-2.822	34.247	.008	-.281	.099	-.483	-.079
# of Nuclear Responses	Equal variances assumed	24.053	.000	-2.146	63	.036	-.111	.052	-.215	-.008
	Equal variances not assumed			-1.803	26.000	.083	-.111	.062	-.238	.016
# of I don't know Responses	Equal variances assumed	7.330	.009	1.651	63	.104	.204	.123	-.043	.450
	Equal variances not assumed			1.676	58.892	.099	.204	.122	-.040	.447
# of No Responses	Equal variances assumed	3.120	.082	-.878	63	.383	-.069	.079	-.227	.088
	Equal variances not assumed			-.838	46.016	.406	-.069	.083	-.235	.097
# of Misc Responses	Equal variances assumed	10.953	.002	1.506	63	.137	.136	.091	-.045	.318
	Equal variances not assumed			1.616	62.529	.111	.136	.084	-.032	.305

*Welch's T-test results are equal variances not assumed.

Table S5: Shapiro-Wilk Test for Normality for "List Methods of Energy Production That Use Non-Renewable Resources"

Tests of Normality

Identifier		Kolmogorov-Smirnov[a]			Shapiro-Wilk		
		Statistic	df	Sig.	Statistic	df	Sig.
Pre-Activity Suvery	# of Fossil Fuel Responses	.535	38	.000	.302	38	.000
	# of Coal Responses	.538	38	.000	.152	38	.000
	# of Oil Responses	.538	38	.000	.152	38	.000
	# of Gas Responses	.538	38	.000	.152	38	.000
	# of Nuclear Responses	.539	38	.000	.237	38	.000
	# of Solar Responses	.538	38	.000	.152	38	.000
	# of Wind Responses	.538	38	.000	.152	38	.000
	# of Hydro Responses	.538	38	.000	.152	38	.000
	# of I don't know Responses	.393	38	.000	.621	38	.000
	# of No Responses	.535	38	.000	.302	38	.000
	# of Misc Responses	.508	38	.000	.439	38	.000
Post-Activity Survey	# of Fossil Fuel Responses	.442	27	.000	.576	27	.000
	# of Coal Responses	.511	27	.000	.427	27	.000
	# of Oil Responses	.525	27	.000	.368	27	.000
	# of Gas Responses	.478	27	.000	.516	27	.000
	# of Nuclear Responses	.478	27	.000	.516	27	.000
	# of Solar Responses	.	27	.	.	27	.
	# of Wind Responses	.	27	.	.	27	.
	# of Hydro Responses	.	27	.	.	27	.
	# of I don't know Responses	.423	27	.000	.597	27	.000
	# of No Responses	.525	27	.000	.368	27	.000
	# of Misc Responses	.535	27	.000	.294	27	.000

a. Lilliefors Significance Correction

Table S6: Independent Samples T-test Results for “List Methods of Energy Production That Use Renewable Resources”

Independent Samples Test

		Levene's Test for Equality of Variances		t-test for Equality of Means						
									95% Confidence Interval of the Difference	
		F	Sig.	t	df	Sig. (2-tailed)	Mean Difference	Std. Error Difference	Lower	Upper
# of Fossil Fuel Responses	Equal variances assumed	25.345	.000	-2.366	63	.021	-.217	.092	-.401	-.034
	Equal variances not assumed			-2.175	38.673	.036	-.217	.100	-.420	-.015
# of Coal Responses	Equal variances assumed	15.710	.000	-1.836	63	.071	-.122	.066	-.254	.011
	Equal variances not assumed			-1.636	33.470	.111	-.122	.074	-.273	.030
# of Oil Responses	Equal variances assumed	8.556	.005	-1.401	63	.166	-.085	.061	-.206	.036
	Equal variances not assumed			-1.265	35.515	.214	-.085	.067	-.221	.051
# of Gas Responses	Equal variances assumed	37.251	.000	-2.601	63	.012	-.196	.075	-.346	-.045
	Equal variances not assumed			-2.287	31.459	.029	-.196	.086	-.371	-.021
# of Nuclear Responses	Equal variances assumed	20.343	.000	-2.088	63	.041	-.170	.081	-.332	-.007
	Equal variances not assumed			-1.897	36.554	.066	-.170	.089	-.351	.012
# of Solar Responses	Equal variances assumed	2.988	.089	.841	63	.404	.026	.031	-.036	.089
	Equal variances not assumed			1.000	37.000	.324	.026	.026	-.027	.080
# of Wind Responses	Equal variances assumed	2.988	.089	.841	63	.404	.026	.031	-.036	.089
	Equal variances not assumed			1.000	37.000	.324	.026	.026	-.027	.080
# of Hydro Responses	Equal variances assumed	2.988	.089	.841	63	.404	.026	.031	-.036	.089
	Equal variances not assumed			1.000	37.000	.324	.026	.026	-.027	.080
# of I don't know Responses	Equal variances assumed	1.037	.312	2.208	63	.031	.272	.123	.026	.518
	Equal variances not assumed			2.220	57.189	.030	.272	.122	.027	.517
# of No Responses	Equal variances assumed	.756	.388	-.435	63	.665	-.032	.074	-.180	.116
	Equal variances not assumed			-.424	50.385	.674	-.032	.076	-.185	.120
# of Misc Responses	Equal variances assumed	4.444	.039	1.006	63	.318	.084	.083	-.083	.250
	Equal variances not assumed			1.062	62.971	.292	.084	.079	-.074	.242

Table S7: Chi-Squared Test for Pre-Activity Survey “Which emits the most CO_2 gas per kilowatthour of energy?”

Response

	Observed N	Expected N	Residual
Fossil Fuels	13	8.8	4.3
Nuclear	10	8.8	1.3
Solar	7	8.8	-1.7
Wind	5	8.8	-3.7
Total	35		

Test Statistics

	Response
Chi-Square	4.200[a]
df	3
Asymp. Sig.	.241

a. 0 cells (0.0%) have expected frequencies less than 5. The minimum expected cell frequency is 8.8.

Table S8: Chi-Squared Test for Post-Activity Survey "Which emits the most CO_2 gas per kilowatthour of energy?"

Response

	Observed N	Expected N	Residual
Fossil Fuels	11	6.5	4.5
Nuclear	8	6.5	1.5
Solar	4	6.5	-2.5
Wind	3	6.5	-3.5
Total	26		

Test Statistics

	Response
Chi-Square	6.308[a]
df	3
Asymp. Sig.	.098

a. 0 cells (0.0%) have expected frequencies less than 5. The minimum expected cell frequency is 6.5.

Table S9: Chi-Squared Test for Pre-Activity Survey "Which emits the least CO_2 gas per kilowatthour of energy?"

Response

	Observed N	Expected N	Residual
Fossil Fuels	5	8.8	-3.7
Nuclear	7	8.8	-1.7
Solar	13	8.8	4.3
Wind	10	8.8	1.3
Total	35		

Test Statistics

	Response
Chi-Square	4.200[a]
df	3
Asymp. Sig.	.241

a. 0 cells (0.0%) have expected frequencies less than 5. The minimum expected cell frequency is 8.8.

Table S10: Chi-Squared Test for Post-Activity Survey "Which emits the least CO_2 gas per kilowatthour of energy?"

Response

	Observed N	Expected N	Residual
Fossil Fuels	4	6.5	-2.5
Nuclear	4	6.5	-2.5
Solar	12	6.5	5.5
Wind	6	6.5	-.5
Total	26		

Test Statistics

	Response
Chi-Square	6.615[a]
df	3
Asymp. Sig.	.085

a. 0 cells (0.0%) have expected frequencies less than 5. The minimum expected cell frequency is 6.5.

Table S11: Chi-Squared Test for Pre-Activity Survey “What is a challenge for using more renewable energy sources?”

Q9

	Observed N	Expected N	Residual
Amount of Sunlight/Wind Changes	6	7.0	-1.0
Storing energy	9	7.0	2.0
Transporting energy	5	7.0	-2.0
All	14	7.0	7.0
None	1	7.0	-6.0
Total	35		

Test Statistics

	Q9
Chi-Square	13.429[a]
df	4
Asymp. Sig.	.009

a. 0 cells (0.0%) have expected frequencies less than 5. The minimum expected cell frequency is 7.0.

Table S12: Chi-Squared Test for Post-Activity Survey “What is a challenge for using more renewable energy sources?”

Q9

	Observed N	Expected N	Residual
Amount of Sunlight/Wind Changes	6	5.2	.8
Storing energy	3	5.2	-2.2
Transporting energy	5	5.2	-.2
All	11	5.2	5.8
None	1	5.2	-4.2
Total	26		

Test Statistics

	Q9
Chi-Square	10.923[a]
df	4
Asymp. Sig.	.027

a. 0 cells (0.0%) have expected frequencies less than 5. The minimum expected cell frequency is 5.2.

Table S13: Shapiro-Wilk Test for Normality for “What is a challenge for using more renewable energy sources?”

Tests of Normality

		Kolmogorov-Smirnov[a]			Shapiro-Wilk		
Identifier		Statistic	df	Sig.	Statistic	df	Sig.
Pre-Activity Suvery	A_Achall	.508	38	.000	.439	38	.000
	B_Chall	.472	38	.000	.528	38	.000
	C_Chall	.518	38	.000	.400	38	.000
	D_Chall	.406	38	.000	.612	38	.000
	E_Chall	.538	38	.000	.152	38	.000
Post-Activity Survey	A_Achall	.539	27	.000	.193	27	.000
	B_Chall	.478	27	.000	.516	27	.000
	C_Chall	.525	27	.000	.368	27	.000
	D_Chall	.495	27	.000	.476	27	.000
	E_Chall	.385	27	.000	.626	27	.000

a. Lilliefors Significance Correction

Table S14: Independent Samples T-test Results for “What is a challenge for using more renewable energy sources?”

Independent Samples Test

		Levene's Test for Equality of Variances		t-test for Equality of Means						
									95% Confidence Interval of the Difference	
		F	Sig.	t	df	Sig. (2-tailed)	Mean Difference	Std. Error Difference	Lower	Upper
A_Achall	Equal variances assumed	11.801	.001	1.554	63	.125	.12086	.07778	-.03457	.27628
	Equal variances not assumed			1.715	58.507	.092	.12086	.07047	-.02017	.26188
B_Chall	Equal variances assumed	.074	.786	.136	63	.892	.01462	.10770	-.20061	.22984
	Equal variances not assumed			.136	56.727	.892	.01462	.10739	-.20045	.22969
C_Chall	Equal variances assumed	.241	.625	.244	63	.808	.02047	.08395	-.14730	.18823
	Equal variances not assumed			.247	58.356	.806	.02047	.08299	-.14563	.18656
D_Chall	Equal variances assumed	11.948	.001	1.608	63	.113	.18324	.11397	-.04451	.41098
	Equal variances not assumed			1.666	61.847	.101	.18324	.10997	-.03659	.40306
E_Chall	Equal variances assumed	168.800	.000	-4.390	63	.000	-.38109	.08680	-.55455	-.20764
	Equal variances not assumed			-3.815	29.906	.001	-.38109	.09989	-.58512	-.17706

Table S14: Levene Test for Homogeneity of Variance for “I am interested in science and engineering.”

Test of Homogeneity of Variance

		Levene Statistic	df1	df2	Sig.
I am interested in science and/or engineering.	Based on Mean	.407	1	63	.526
	Based on Median	.001	1	63	.975
	Based on Median and with adjusted df	.001	1	62.435	.975
	Based on trimmed mean	.282	1	63	.597

Table S15: Mann-Whitney U Test for Difference of Ranked means between Pre/Post Surveys for “I am interested in science and engineering.”

Test Statistics[a]

	I am interested in science and/or engineering.
Mann-Whitney U	494.500
Wilcoxon W	1235.500
Z	-.273
Asymp. Sig. (2-tailed)	.785

a. Grouping Variable: Randon ID two specific Pre/Post

Table S16: Levene Test for Homogeneity of Variance for “I would like a job in science and engineering.”

Test of Homogeneity of Variance

		Levene Statistic	df1	df2	Sig.
I would like a job in science and/or engineering.	Based on Mean	1.261	1	63	.266
	Based on Median	1.301	1	63	.258
	Based on Median and with adjusted df	1.301	1	62.999	.258
	Based on trimmed mean	1.256	1	63	.267

Table S17: Mann-Whitney U Test for Difference of Ranked means between Pre/Post Surveys for “I would like a job in science and engineering.”

Test Statistics[a]

	I would like a job in science and/or engineering.
Mann-Whitney U	482.500
Wilcoxon W	860.500
Z	-.420
Asymp. Sig. (2-tailed)	.674

a. Grouping Variable: Randon ID two specific Pre/Post

Table S18: Levene Test for Homogeneity of Variance for “I know about jobs in science and engineering.”

Test of Homogeneity of Variance

		Levene Statistic	df1	df2	Sig.
I know about jobs in science and/or engineering	Based on Mean	.422	1	63	.518
	Based on Median	.212	1	63	.646
	Based on Median and with adjusted df	.212	1	62.722	.646
	Based on trimmed mean	.503	1	63	.481

Table S19: Mann-Whitney U Test for Difference of Ranked means between Pre/Post Surveys for “I know about jobs in science and engineering.”

Test Statistics[a]

	I know about jobs in science and/or engineering
Mann-Whitney U	474.000
Wilcoxon W	1215.000
Z	-.542
Asymp. Sig. (2-tailed)	.588

a. Grouping Variable: Randon ID two specific Pre/Post

Table S20: Levene Test for Homogeneity of Variance for “I do well with science and engineering activities.”

Test of Homogeneity of Variance

		Levene Statistic	df1	df2	Sig.
I do well with science and engineering activities.	Based on Mean	.038	1	63	.846
	Based on Median	.013	1	63	.909
	Based on Median and with adjusted df	.013	1	61.881	.909
	Based on trimmed mean	.010	1	63	.922

Table S21: Mann-Whitney U Test for Difference of Ranked means between Pre/Post Surveys for “I do well with science and engineering activities.”

Test Statistics[a]

	I do well with science and engineering activities.
Mann-Whitney U	507.000
Wilcoxon W	885.000
Z	-.085
Asymp. Sig. (2-tailed)	.932

a. Grouping Variable: Randon ID two specific Pre/Post

Table S22: Levene Test for Homogeneity of Variance for "I enjoy science and engineering activities."

Test of Homogeneity of Variance

		Levene Statistic	df1	df2	Sig.
I enjoy science and engineering activities.	Based on Mean	.023	1	61	.880
	Based on Median	.026	1	61	.871
	Based on Median and with adjusted df	.026	1	60.923	.871
	Based on trimmed mean	.002	1	61	.961

Table S23: Mann-Whitney U Test for Difference of Ranked means between Pre/Post Surveys for "I enjoy science and engineering activities."

Test Statistics[a]

	I enjoy science and engineering activities.
Mann-Whitney U	462.500
Wilcoxon W	1128.500
Z	-.390
Asymp. Sig. (2-tailed)	.696

a. Grouping Variable: Randon ID two specific Pre/Post

Table S24: Pearson's Correlations for Pre-Activity Survey Questions

Correlations

		Pre-Survey: I am interested in science and/or engineering.	Pre-Survey: I would like a job in science and/or engineering.	Pre-Survey: I know about jobs in science and/or engineering	Pre-Survey: I do well with science and engineering activities.	Pre-Survey: I enjoy science and engineering activities.
Pre-Survey: I am interested in science and/or engineering.	Pearson Correlation	1	.294	.498**	.575**	.843**
	Sig. (2-tailed)		.074	.001	.000	.000
	N	38	38	38	38	36
Pre-Survey: I would like a job in science and/or engineering.	Pearson Correlation	.294	1	.285	.041	.198
	Sig. (2-tailed)	.074		.083	.807	.248
	N	38	38	38	38	36
Pre-Survey: I know about jobs in science and/or engineering	Pearson Correlation	.498**	.285	1	.486**	.391*
	Sig. (2-tailed)	.001	.083		.002	.018
	N	38	38	38	38	36
Pre-Survey: I do well with science and engineering activities.	Pearson Correlation	.575**	.041	.486**	1	.526**
	Sig. (2-tailed)	.000	.807	.002		.001
	N	38	38	38	38	36
Pre-Survey: I enjoy science and engineering activities.	Pearson Correlation	.843**	.198	.391*	.526**	1
	Sig. (2-tailed)	.000	.248	.018	.001	
	N	36	36	36	36	36

**. Correlation is significant at the 0.01 level (2-tailed).

*. Correlation is significant at the 0.05 level (2-tailed).

Table S24: Pearson's Correlations for Post-Activity Survey Questions

Correlations

		Post-Survey: I am interested in science and/or engineering.	Post-Survey: I would like a job in science and/or engineering.	Post-Survey: I know about jobs in science and/or engineering	Post-Survey: I do well with science and engineering activities.	Post-Survey: I enjoy science and engineering activities.	Post-Survey: I enjoyed this activity.
Post-Survey: I am interested in science and/or engineering.	Pearson Correlation	1	.533**	.097	.688**	.786**	.582**
	Sig. (2-tailed)		.004	.629	.000	.000	.001
	N	27	27	27	27	27	27
Post-Survey: I would like a job in science and/or engineering.	Pearson Correlation	.533**	1	-.056	.184	.606**	.319
	Sig. (2-tailed)	.004		.781	.359	.001	.105
	N	27	27	27	27	27	27
Post-Survey: I know about jobs in science and/or engineering	Pearson Correlation	.097	-.056	1	.375	.268	.318
	Sig. (2-tailed)	.629	.781		.054	.176	.106
	N	27	27	27	27	27	27
Post-Survey: I do well with science and engineering activities.	Pearson Correlation	.688**	.184	.375	1	.650**	.562**
	Sig. (2-tailed)	.000	.359	.054		.000	.002
	N	27	27	27	27	27	27
Post-Survey: I enjoy science and engineering activities.	Pearson Correlation	.786**	.606**	.268	.650**	1	.541**
	Sig. (2-tailed)	.000	.001	.176	.000		.004
	N	27	27	27	27	27	27
Post-Survey: I enjoyed this activity.	Pearson Correlation	.582**	.319	.318	.562**	.541**	1
	Sig. (2-tailed)	.001	.105	.106	.002	.004	
	N	27	27	27	27	27	27

**. Correlation is significant at the 0.01 level (2-tailed).

Table S25: Wilcoxon Signed Ranks Test for "I enjoy science and engineering activities" and "I enjoyed this activity."

Ranks

		N	Mean Rank	Sum of Ranks
Post-Survey: I enjoyed this activity. - Post-Survey: I enjoy science and engineering activities.	Negative Ranks	2[a]	4.00	8.00
	Positive Ranks	7[b]	5.29	37.00
	Ties	18[c]		
	Total	27		

a. Post-Survey: I enjoyed this activity. < Post-Survey: I enjoy science and engineering activities.

b. Post-Survey: I enjoyed this activity. > Post-Survey: I enjoy science and engineering activities.

c. Post-Survey: I enjoyed this activity. = Post-Survey: I enjoy science and engineering activities.

Test Statistics[a]

	Post-Survey: I enjoyed this activity. - Post-Survey: I enjoy science and engineering activities.
Z	-1.741[b]
Asymp. Sig. (2-tailed)	.082

a. Wilcoxon Signed Ranks Test

b. Based on negative ranks.